NTNU – Trondheim
Norwegian University of
Science and Technology

Alternating Current Corrosion of Steel in Seawater

Are Bergin

Materials Technology
Submission date: June 2015
Supervisor: Kemal Nisancioglu, IMTE
Co-supervisor: Magnus Hurlen Larsen, Nexans Norway AS

Norwegian University of Science and Technology
Department of Materials Science and Engineering

Declaration

I hereby declare that all work performed in connection with this master's thesis, has been performed independently and in accordance with the rules and examination regulations of Norwegian University of Science and Technology (NTNU).

Are Bergin

Trondheim, 05.06.2015

Preface

This master's thesis was written during the spring of 2015, at the Department of Materials Science and Engineering (IMT) at the Norwegian University of Science and Technology (NTNU), in Trondheim, Norway. Initiator was Nexans Norway AS, and the thesis is a continuation of the work performed in the course TMT4500, Materials technology specialization project during the autumn of 2014.

The author would like to thank supervisor Kemal Nisancioglu (professor, NTNU) for guidance and help when it was needed.

Gratitude is also directed towards NTNU's technical laboratory of materials and the staff at Department of Materials Science and Engineering, for always being very helpful.

Are Bergin

Abstract

A challenge regarding the transportation of oil and gas in pipelines subsea is to keep the temperature high enough to avoid formation of wax and hydrates, which eventually will stop the flow. In 2000, Nexans introduced a Direct Electrical Heating-system (DEH) that heats up the pipe by applying an alternating current (AC). The problem with applying AC is an increased risk of corrosion. The mechanism of AC corrosion has yet to be fully understood, and there exists limited data on its severity.

The purpose of this thesis is to examine the effect of AC, determine the mechanism of AC corrosion and provide data describing its severity on steel. To achieve this, the following types of steel were investigated through cathodic polarization: X65 carbon steel (CS), AISI 316 stainless steel (SS) and 25Cr super duplex stainless steel (SDSS). A total of 28 samples were tested under cathodic protection-potential (CP) of either -800 mV or -1050 mV, and an applied AC in the range of 0-1000 A/m^2. Testing was performed in 3.5 % NaCl-solution and artificial seawater and lasted for 48 hours. To examine the effect of AC properly, weight loss measurements and surface characterization by Scanning Electron Microscope (SEM) and X-Ray Diffraction (XRD) was performed.

Cathodic currents were observed for all tested samples, where an increase in AC and a negative increase in CP-potential caused increasingly cathodic currents. Increase in AC caused the AC cell potential (V_{AC}) to increase as well. Both cathodic currents and V_{AC} was in the following order, from high to low: 25Cr>316>X65.

Some correlation between the corrosion rates (CR) and the DC current response were found, where an increase in AC increased the CR and the current response. There was not found any correlation between CR and applied CP-potential. The following CRs were calculated for the various types of steel: 0-0.260 mm/year (316), 0-0.522 mm/year (25Cr) and 0.191-0.297 mm/year (X65). When tested at CP-potentials of -800 mV and -1050 mV under 500 A/m^2 applied AC, the CRs were in the following order from high to low: X65>25Cr>316.

Surface topography was seen to have no effect on AC corrosion, while artificial seawater showed a slight decrease in CR compared to 3.5 % NaCl-solution. The latter is likely due calcareous deposits that formed on all samples tested in artificial seawater, usually as $CaCO_3$ and $Mg(OH)_2$. In 3.5 % NaCl-solution, the formed corrosion products were characterized as Fe_3O_4, while Fe_2O_3 and γ-FeOOH was seen to form in artificial seawater.

Sammendrag

En av flere utfordringer når det gjelder transport av olje og gass gjennom rør subsea, er å holde temperaturen tilstrekkelig høy slik at man unngår at voks og hydrater tetter rørene. I år 2000, introduserte Nexans et såkalt Direct Electrical Heating-system (DEH) som varmer opp rørene ved hjelp av vekselstrøm (AC). Den negative siden ved dette er at det er identifisert en økt risiko for korrosjon når AC påføres. Mekanismen for såkalt AC-korrosjon er ikke helt forstått, og det finnes få studier som har undersøkt alvorlighetsgraden.

Formålet med denne masteroppgaven er å undersøke effekten av AC, fastslå mekanismen bak AC-korrosjon og produsere data som sammen med tidligere studier kan si noe om AC-korrosjons alvorlighetsgrad når det kommer til stål. For å oppnå dette så har forskjellige typer stål blitt undersøkt gjennom katodisk polarisasjon: X65 karbonstål, AISI 316 rustfritt stål og 25Cr super duplex rustfritt stål. 28 prøver ble testet under en katodisk beskyttelse (CP) på enten -800 mV eller -1050 mV, og med en påført AC i området 0-1000 A/m^2. Eksperimentene ble utført i 3.5 % NaCl-løsning og kunstig sjøvann, og varte i 48 timer. For å nå oppgavens mål ble vekttapsmålinger utført, samt undersøkelser gjennom Scanning Electron Microscope (SEM) og X-Ray Diffraction (XRD).

Katodiske strømtettheter ble målt for alle prøvene, hvor en økning i AC og en mindre negativ CP førte til at den katodiske strømtettheten økte. En økning i AC førte også til at cellepotensialet for AC (V_{AC}) økte. Videre så var både katodisk strømtetthet og V_{AC} i følgende rekkefølge, fra høy til lav: 25Cr>316>X65.

Det ble observert en viss korrelasjon mellom korrosjonshastigheter (CR) og målte strømtettheter, blant annet at en økning i AC gjør at både CR og strømtettheten øker. Det ble ikke funnet noen korrelasjon mellom CR og de to påførte CP-potensialene. Følgende CR ble funnet for de forskjellige ståltypene: 0-0.260 mm/år (316), 0-0.522 mm/år (25Cr) og 0.191-0.297 mm/år (X65). Ved samme betingelser, henholdsvis påført CP på enten -800 mV eller -1050 mV og påført AC på 500 A/m^2, så var CR i følgende rekkefølge fra høy til lav: X65>25Cr>316.

Det ble videre konkludert med at overflatetopografi ikke har noen innvirkning på AC-korrosjon, mens CR ble funnet til å være noe lavere for kunstig sjøvann sammenlignet med 3.5 % NaCl-løsning. Sistnevnte er sannsynligvis som en følge av at kalkprodukter av $CaCO_3$ og $Mg(OH)_2$, dannet seg på prøveoverflaten til alle prøver som ble testet i kunstig sjøvann. Gjennom XRD-analyse ble det funnet forskjellige korrosjonsprodukter i de forskjellige løsningene: Fe_3O_4 ble funnet på prøver testet i 3.5 % NaCl-løsning, mens Fe_2O_3 og γ-FeOOH ble funnet i kunstig sjøvann.

Contents

Declaration i

Preface iii

Abstract v

Sammendrag vii

Contents ix

List of Figures xiii

List of Tables xix

Nomenclature xxi

1 Introduction 1

- 1.1 Background 1
- 1.2 Purpose of thesis 1
- 1.3 Thesis outline 2

2 Theory 3

- 2.1 History 3
- 2.2 Direct Electrical Heating (DEH) 4
- 2.3 Corrosion behavior in absence of AC 6
  - 2.3.1 General corrosion behavior 6
  - 2.3.2 Localized corrosion behavior 8
  - 2.3.3 Cathodic Protection 9
  - 2.3.4 Immersion testing in 3.5 % NaCl-solution and seawater 11
- 2.4 AC-induced corrosion 12
  - 2.4.1 AC corrosion mechanism 12
  - 2.4.2 Influences on AC corrosion 14
  - 2.4.3 Potential behavior in an open circuit 16
  - 2.4.4 Corrosion kinetics 16
  - 2.4.5 Current behavior under cathodic protection 18

- 2.4.6 Weight loss and corrosion rates 20
- 2.4.7 Surface characterization 22
- 2.4.8 Changes in pH due to AC 23
- 2.5 Summary 23
- 3 Experimental 25
  - 3.1 Test sample 25
    - 3.1.1 Material specification 25
    - 3.1.2 Sample preparation and geometry 26
  - 3.2 Experimental set up 28
    - 3.2.1 Preparation of electrolytes 28
    - 3.2.2 Equipment 29
    - 3.2.3 Apparatus set up 29
    - 3.2.4 Experimental procedure 31
    - 3.2.5 Experimental method 32
  - 3.3 Weight loss measurements 33
  - 3.4 Surface characterization 34
- 4 Results 35
  - 4.1 Polarization behavior 36
    - 4.1.1 Polarization behavior in absence of AC 36
    - 4.1.2 Polarization behavior of various surface roughness 36
    - 4.1.3 Polarization behavior of AISI 316 SS 40
    - 4.1.4 Polarization behavior of 25Cr SDSS 42
  - 4.2 Weight loss measurements 43
    - 4.2.1 Weight loss measurements in absence of AC 43
    - 4.2.2 Weight loss measurements of various surface roughness 44
    - 4.2.3 Weight loss measurements of AISI 316 SS 44
    - 4.2.4 Weight loss measurements of 25Cr SDSS 45

4.2.5 Weight loss measurements of the stored sample 45

4.3 Macroscopic surface characterization 46

4.3.1 Surface characterization in absence of AC 46

4.3.2 Surface characterization of various surface roughness 46

4.3.3 Surface characterization of AISI 316 SS 48

4.3.4 Surface characterization of 25Cr SDSS 49

4.3.5 Surface characterization of samples for GIXRD analysis 50

4.4 Microscopic surface characterization 51

4.4.1 XRD analysis 51

4.4.2 GIXRD analysis 52

4.4.3 SEM analysis 54

4.4.4 EDS analysis 58

4.5 Observations during experimental testing 58

4.5.1 Initial color on sample surface 58

4.5.2 Chlorine evolution 58

4.5.3 AC counter electrode 59

4.5.4 pH measurements 59

4.6 Summary of results 60

5 Discussion 63

5.1 Polarization behavior 63

5.1.1 Current behavior 63

5.1.2 AC cell potential 65

5.2 Weight loss and corrosion rates 66

5.3 Surface characterization 69

5.4 The mechanism for AC corrosion 72

5.5 Evaluation of experimental work 73

5.6 Suggestions for further work 74

6 Conclusions 77

7 References 79

Appendix A: Equations I

  A.1 Required AC voltage I

  A.2 Corrosion rate (CR) I

Appendix B: Weight loss-graph for X65 II

Appendix C: Reproducibility III

Appendix D: Parallel testing of 25Cr IV

Appendix E: Additional XRD data VI

Appendix F: Additional EDS data VIII

List of Figures

Figure 2-1: Cross-sections of two plugged pipelines [6]. 3

Figure 2-2: Illustration of Nexans' DEH-system with the different cable types [1]. 4

Figure 2-3: Schematic view of the DEH-system with current directions included [6]. 5

Figure 2-4: The equivalent electrical circuit that acts as a model for the interface between the metal surface and the surrounding electrolyte. Figure is adapted from literature [11]. 6

Figure 2-5: Two types of pitting described by N. Sato.; etch pitting at low potential in active state and polish pitting at high potentials with transpassive dissolution at pit surface [17]....... 9

Figure 2-6: The Pourbaix diagram for iron/carbon steel in water. The active corrosion, immune and passive regions are indicated, as well as the critical pitting potential [21]. 10

Figure 2-7: Schematic view of the AC corrosion mechanism when samples are under CP (i_{DC} > 1A/m^2), with graph and illustrations [33]. 12

Figure 2-8: Corrosion rate as a function of applied AV. Experiments at room temperature, O_2 removed and at a frequency of 60 Hz [31]. 15

Figure 2-9: Recorded DC potential as a function of time with various AC applied. Recorded at a steel sample with a circular coating defect with a diameter of 5 mm [5]. 16

Figure 2-10: Schematic effect of AC on cathodic overpotential. Left illustration indicates effect on oxygen reduction, the right one indicates effect on hydrogen evolution [40]........... 17

Figure 2-11: Schematic effect of AC on anodic overpotential. Where the cathodic reaction at a) and b) is oxygen reduction and hydrogen evolution, respectively [40]. 17

Figure 2-12: Recorded DC current density as a function of time with various AC applied. The steel sample is polarized potentiostatically at -0.85 V vs SCE [30].. 18

Figure 2-13: Recorded DC current density as a function of time with various AC applied. The steel sample is polarized potentiostatically at -1 V vs SCE [30]... 19

Figure 2-14: Recorded DC current density as a function of time, for X65 in -800 mV DC vs SCE for different AC current densities. First five hours of a total 48 hour long experiment [26]. 20

Figure 2-15: Corrosion rate as a function of applied i_{AC} under different CP-potentials. Determined by weight loss measurements of steel immersed in simulated soil solution [30]. 21

Figure 2-16: Corrosion rate as a function of applied i_{AC} under E_{OC} and different CP-potentials. Based on weight loss measurements of X65 immersed in 3.5 % NaCl-solution. Plot adapted from results by Stamnes [42]. 22

Figure 3-1: The first photo shows two 25Cr-samples, were the left on is prior to cleaning and the right one has been cleaned. The second photo shows the surface difference between some cleaned samples. The samples that was shiny, as the one to the far right was used for XRD and not weight loss measurements 26
Figure 3-2: The left picture is of the standard analytical weight and the right picture is of the lacquer used to coat the samples. 27
Figure 3-3: The left picture shows some samples before they were coated, and the difference in exposed area is visible. The picture in the middle shows how the sample top was covered to avoid unwanted corrosion. The right picture shows drying and storing of the samples after coating. 28
Figure 3-4: Schematic circuit diagram of the used circuit, where the AC-part is on the right and the DC-part is on the left. C is a capacitor, L is an inductor, VM is voltmeters, R is a resistance and the VariAC is the source of the AC signal. The black component is the SCE, the green tube connecting the baths is the salt bridge, the two blue elements are counter electrodes and the red component is the working electrode/steel sample. The circuit diagram is an edited version of the original made by C. B. Esser [27]. 30
Figure 3-5: Picture of the experimental set-up. The numbered components are: 1) PC-based Gamry Potentiostat 2) transformer 3)VariAC 4) capacitor and resistance 5) inductor 6) multimeter displaying AC potential from VariAC 7) multimeter logging AC cell potential 8) multimeter displaying DC polarization from potentiostat 9) stirrer 10) temperature-controlled water bath 11) AC counter electrode 12) working electrode 13) SCE 14) salt bridge 15) DC counter electrode 16) grounding wire. 31
Figure 4-1: The recorded DC current density response as a function of time, with no AC applied. Samples are polarized at -800 and -1050 mV DC, in 3.5 % NaCl-solution and artificial seawater. 36
Figure 4-2: The recorded DC current density response as a function of time, with 500 A/m^2 AC applied. Samples are either milled or grinded at 1000 grit, and polarized at -800 mV DC in 3.5 % NaCl-solution. 37
Figure 4-3: The recorded DC current density response as a function of time, with 500 A/m^2 AC applied. Samples are either milled or grinded at 1000 grit, and polarized at -1050 mV DC in 3.5 % NaCl-solution. 37
Figure 4-4: The recorded DC current density response as a function of time, with 500 A/m^2 AC applied. Samples are either milled or grinded at 1000 grit, and polarized at -800 mV DC in artificial seawater. 38

Figure 4-5: The recorded DC current density response as a function of time, with 500 A/m^2 AC applied. Samples are either milled or grinded at 1000 grit, and polarized at -1050 mV DC in artificial seawater. 38

Figure 4-6: The recorded AC cell potential as a function of time, with 500 A/m^2 AC applied. Samples are either milled or grinded at 1000 grit, and polarized at -800 or -1050 mV DC in 3.5 % NaCl-solution. 39

Figure 4-7: The recorded AC cell potential as a function of time, with 500 A/m^2 AC applied. Samples are either milled or grinded at 1000 grit, and polarized at -800 or -1050 mV DC in artificial seawater. 39

Figure 4-8: The recorded DC current density response as a function of time, with different AC applied at 316-samples. The samples are milled and polarized at different potentials in artificial seawater. 40

Figure 4-9: The recorded AC cell potential as a function of time, with various AC applied at 316-samples. The samples are milled and polarized at different potentials in artificial seawater. 41

Figure 4-10: The recorded DC current density response as a function of time, with different AC applied at 25Cr-samples. The samples are milled and polarized at different potentials in artificial seawater. 42

Figure 4-11: The recorded AC cell potential as a function of time, with various AC applied at 25Cr-samples. The samples are milled and polarized at different potentials in artificial seawater. 43

Figure 4-12: Pictures of the samples tested with applied DC and absence of AC. The top pictures are prior to cleaning and the bottom one is post cleaning. Of the top pictures: the two to the left are tested in 3.5 % NaCl-solution and the right ones in artificial seawater. From left to right they have been tested at -800, -1050, -800 and -1050 mV DC. The bottom picture corresponds to the first at the top. 46

Figure 4-13: Pictures of samples with different surface roughness tested in 3.5 % NaCl-solution at 500 A/m^2 AC. The top pictures are prior to cleaning and the bottom one is post cleaning. The left cluster was tested at -800 mV DC, and the other at -1050 mV DC. Within each cluster, the 1000 grit samples are to the left. 47

Figure 4-14: Pictures of samples with different surface roughness tested in artificial seawater at 500 A/m^2 AC. The top pictures are prior to cleaning and the bottom one is post cleaning. The left cluster was tested at -800 mV DC, and the other at -1050 mV DC. Within each cluster, the 1000 grit samples are to the left. 47

Figure 4-15: Pictures of 316-samples tested in artificial seawater at 500 A/m^2 AC. The top pictures are right after testing, the middle ones are after deposits have been stripped off prior to cleaning and the bottom one is post cleaning. The left row was tested at -800 mV DC, and the right at -1050 mV DC. 48

Figure 4-16: Pictures of 316-samples tested in artificial seawater at 1000 A/m^2 AC. The top pictures are prior to cleaning and the bottom ones are post cleaning. The left row was tested at -800 mV DC, the middle at -1050 mV DC and the right is the re-test of the middle one. 48

Figure 4-17: Pictures of 25Cr-samples tested in artificial seawater. The top pictures are prior to cleaning and the bottom one is post cleaning. The left cluster was tested at 100 A/m^2 AC, and the right cluster at 500 A/m^2 AC. Within each cluster, the left samples are at -800 mV DC and the right at -1050 mV DC. 49

Figure 4-18: Pictures of 25Cr-samples tested in artificial seawater at 1000 A/m^2 AC. The top pictures are prior to cleaning and the bottom one is post cleaning. The pictures to the left are samples tested at -800 mV DC and the right at -1050 mV DC. 49

Figure 4-19: Picture of an X65-sample before GIXRD analysis. It was tested in 3.5 % NaCl-solution at -800 mV DC and 700 A/m^2 AC. The sample was cut without any cooling medium. 50

Figure 4-20: Picture of an X65-sample before GIXRD analysis. It was tested in artificial seawater at -800 mV DC and 500 A/m^2 AC. The left picture is before the sample was cut, while the right is after it was cut with water as cooling medium. This sample corresponds to the left cluster in Figure 4-14. 50

Figure 4-21: Picture of a 25Cr-sample before GIXRD analysis. It was tested in artificial seawater at -800 mV DC and 1000 A/m^2 AC. The left picture is just after the sample was removed from solution, the middle picture is before cutting and the right picture is after it was cut with water as cooling medium. This sample corresponds to the left pictures in Figure 4-18. 50

Figure 4-22: X-ray diffractogram of crushed calcareous deposit formed on 25Cr tested in artificial seawater at -800 mV DC and 1000 A/m^2 AC. This corresponds to the pictures on the left row in Figure 4-18 and the sample in Figure 4-21. 51

Figure 4-23: X-ray diffractogram of a surface film on a X65-sample tested in 3.5 % NaCl-solution at -800 mV DC and 700 A/m^2 AC. This corresponds to the picture in Figure 4-19. . 52

Figure 4-24: X-ray diffractogram of a surface film on an X65-sample tested in artificial seawater at -800 mV DC and 500 A/m^2 AC. This corresponds to the picture in Figure 4-20 (which is tested at same parameters as the left cluster in Figure 4-14). 53

Figure 4-25: X-ray diffractogram of a surface film on a 25Cr-sample tested in artificial seawater at -800 mV DC and 1000 A/m^2 AC. This analysis corresponds to the picture in Figure 4-21 (and tested at the same parameters as the left part of Figure 4-18). 53

Figure 4-26: SEM images taken of X65-samples with different surface roughness, tested in 3.5 % NaCl-solution at -800 mV DC and 500 A/m^2 AC. The left sample is milled and the right is grinded to 1000 grit. Images are taken with a magnification of 500 X. 54

Figure 4-27: SEM images taken of X65-samples with different surface roughness, tested in artificial seawater at -800 mV DC and 500 A/m^2 AC. The left sample is milled and the right is grinded to 1000 grit. Images are taken with a magnification of 500 X. 54

Figure 4-28: SEM images taken of X65-samples with different surface roughness, tested in artificial seawater at -1050 mV DC and 500 A/m^2 AC. The left sample is milled and the right is grinded to 1000 grit. Images are taken with a magnification of 500 X. 55

Figure 4-29: SEM images taken of 316-samples tested in artificial seawater at 500 A/m^2 AC. The top sample was polarized at -800 mV DC, the bottom at -1050 mV DC. Images are taken with a magnification of 500 X. The magnified square at the bottom image is at 2000 X. 56

Figure 4-30: SEM images taken of 25Cr-samples tested in artificial seawater at 100 A/m^2 AC. The left sample tested at -800 mV DC and the right at -1050 mV DC. Images are taken with a magnification of 500 X. 57

Figure 4-31: SEM images taken of 25Cr-samples tested in artificial seawater at 500 A/m^2 AC. The left sample tested at -800 mV DC and the right at -1050 mV DC. Images are taken with a magnification of 500 X. 57

Figure 4-32: SEM images taken of 25Cr-samples tested in artificial seawater at 1000 A/m^2 AC. The left sample tested at -800 mV DC and the right at -1050 mV DC. Images are taken with a magnification of 500 X. 58

Figure 4-33: A photograph of the AC counter electrode that has started to dissolve. 59

Figure 4-34: Calculated corrosion rate for all different-samples tested (at different ACs under -800 and -1050 mV DC) in artificial seawater. The CR-values are averaged for the experiments tested twice, but deviations are not included. 61

Figure 5-1: Pourbaix diagram for iron species in the ternary system of Fe-Cr-Ni at 25 °C. The question mark at FeO_4^{2-} indicates uncertainty on its stoichiometry and stability [50]............ 68

Figure 5-2: Pourbaix diagram for the platinum-water system at 25 °C. The question marks behind the ions on the left and right hand side indicate uncertainty due to lack of thermodynamic data [51]. 69

Figure B-1: Example of measured weight loss as a function of number of cycles, according to ASTM G-1. The corresponding experiment was performed at a grinded X65-sample tested in 3.5 % NaCl-solution at -1050 mV DC and 500 A/m^2 AC. The weight loss was determined to be 0.0055 g. II
Figure C-1: Corrosion rate as a function of applied DC-potential. The plot compares results from this thesis with results from C. H. M. Hagen's thesis. The results were acquired from experiments performed at -800 mV and -1050 mV DC, in 3.5 % NaCl-solution at 500 A/m^2 AC. III
Figure D-1: The recorded DC current density response as a function of time. Both experiments have been tested at 25Cr under a DC of -800 mV at 1000 A/m^2 AC in artificial seawater. IV
Figure D-2: The recorded AC cell potential as a function of time. Both experiments have been tested at 25Cr under a DC of -800 mV at 1000 A/m^2 AC in artificial seawater. IV
Figure E-1: X-ray diffractogram of crushed calcareous deposits formed on 316 tested in artificial seawater at -800 mV DC and 1000 A/m^2 AC. VI
Figure E-2: X-ray diffractogram of crushed cell sediments formed during an experiment on X65 in artificial seawater at -800 mV DC and 500 A/m^2 AC. VII
Figure F-1: SEM image from the darkest area seen on the 25Cr-sample tested in artificial seawater at -800 mV DC and 500 A/m^2 AC. VIII

List of Tables

Table 3-1: The chemical composition of the X65 carbon steel used in this thesis. Values are given in wt%. 25
Table 3-2: The chemical composition of the AISI 316 Stainless Steel. Values are given in wt%. 25
Table 3-3: The chemical composition of the 25Cr Super Duplex Stainless Steel. Values are given in wt%. 26
Table 3-4: The ideal dimensions of the samples. 27
Table 3-5: The composition of artificial seawater [46]. 28
Table 3-6: The various solutions and procedures for chemical cleaning of the tested samples. 33
Table 4-1: Calculated corrosion rate for X65-samples tested at 500 A/m^{2}AC under -800 and -1050 mV DC, in 3.5 % NaCl-solution and artificial seawater. The samples have been either milled or grinded to 1000 grit. 44
Table 4-2: Calculated corrosion rate for 316-samples tested at different ACs under -800 and -1050 mV DC, in artificial seawater. One sample was re-tested. 44
Table 4-3 Calculated corrosion rate for 25Cr-samples tested at different ACs under -800 and -1050 mV DC in artificial seawater. 45
Table 4-4: Calculated corrosion rate for a milled X65-sample tested at 500 A/m^{2}AC and -800 mV DC Testing was done in 3.5 % NaCl-solution and the sample was stored three months in a desiccator between testing and cleaning. 45
Table 4-5: Key results from the DC current response and AC cell potential during polarization, for all DC-potentials and and types of metal. All samples were under applied AC of 500 A/m^2, except for X65(DC), which was tested in absence of AC. V_{AC_avg} is averaged over the whole experiment, i_{net_start} is collected 2.5 hours into the experiment and i_{net_end} is collected at the end. The collected values for X65 are also averaged over the two surface topographies. 60
Table D-1: Calculated corrosion rate for 25Cr-samples. Both samples have been tested under a DC of -800 mV at 1000 A/m^2 AC in artificial seawater. V
Table F-1: The measured composition of EDS Spot 1 visible in Figure F-1. VIII
Table F-2: The measured composition of EDS Spot 4 visible in Figure F-1. VIII
Table F-3: The measured composition of Full Area 1 (which is the whole image) visible in Figure F-1. VIII

Nomenclature

AC	Alternating Current
AV	Alternating Voltage
CP	Cathodic Protection
CR	Corrosion Rate
CS	Carbon Steel
DC	Direct Current
DEH	Direct Electrical Heating
EDS	Energy-Dispersive X-ray Spectroscopy
E_{corr}	Corrosion potential
HSE	Health, Safety and Environment
GIXRD	Grazing Incidence X-ray Diffraction
i_{corr}	Corrosion Current Density
i_{DC}	Current Density of DC
i_{net}	Net Current Density
Pt	Platinum
RMS	Root Mean Square
Rpm	Revolutions per minute
SEM	Scanning Electron Microscope
SCE	Standard Calomel Electrode (reference electrode)
SDSS	Super Duplex Stainless Steel
SG	Specific Gravity (related to wt%)
SHE	Standard Hydrogen Electrode (reference electrode)
SMSS	Super Martensitic Stainless Steel
SS	Stainless Steel
XRD	X-Ray Diffraction

316 An Austenitic Stainless Steel (AISI 316L)

316 An Austenitic Stainless Steel (AISI 316L)

1 Introduction

1.1 Background

Oil and gas are often collected from the bottom of the sea through long pipelines. A likely and potential devastating problem is that during shutdown, the multiphase flow will experience heat loss, which again will cause formation of wax and hydrates that may clog the pipelines. In order to avoid such clogging, heating of the pipelines with a system called Direct Electrical Heating (DEH) is used. This system heats up the pipeline by applying an alternating current (AC), which flows through the walls of the pipe and heats it up due to its own electrical resistance [1].

However, a problem has been seen to rise upon application of AC: the AC-signal has been seen to affect the conventional corrosion theory. It has been widely acknowledged that steel pipelines suffer from AC corrosion despite satisfying cathodic protection (CP) criteria, and several failures from all over the world has been reported [2]. In later years there has been an increased amount of research regarding this topic, and it has been determined that steel will not suffer from AC corrosion if CP is applied through aluminum sacrificial anodes [3]. However, if CP is applied by a current rectifier and there are defects in the coating, the steel will suffer from AC corrosion [4, 5]. There is a lack of understanding how the superimposition of AC on a DC-signal effects the corrosion behavior of steel. In order to develop a system that can ensure that structures are fully protected from AC, even in cases where sacrificial anodes are inapplicable, it is necessary to determine and understand the mechanism of AC corrosion. In addition, it is advantageous to be aware of AC corrosions severity on different steels.

1.2 Purpose of thesis

This thesis is a continuation of TMT4500 Specialization project in materials technology, and a part of ongoing research studying the electrochemistry of corrosion under the influence of AC. The main scope of the thesis is to examine the effect of applied AC, determine the mechanism of AC corrosion and provide data describing the severity of AC corrosion on steel. A secondary scope is to check a few assumptions regarding the high corrosion rates (CR) presented during the specialization project.

The chosen methodology to reach these goals will be through cathodic polarization of X65 carbon steel, AISI 316 stainless steel and 25Cr super duplex stainless steel under appliance of AC. The experimental set up consists of two parts; one is a regular three-electrode potentiostat that polarizes the steel cathodically, while the other is an AC-circuit that superimposes an alternating voltage (AV) on the steel. The methodology can be divided into five parts, whereas the three first will be performed on X65: examine the effect of storing corroded samples, effect of surface roughness, difference between 3.5 % NaCl-solution and artificial seawater, effect of AC on 316 and effect of AC on 25Cr.

Polarization behavior, weight loss measurements and surface characterization through Scanning Electron Microsope (SEM), Energy-Dispersive X-ray Spectroscopy (EDS), X-Ray Diffraction (XRD) and Grazing Incidence X-ray Diffraction (GIXRD) will be performed to examine the effect of applied AC properly.

1.3 Thesis outline

The thesis is divided into six chapters. Appendices and references will be presented after the six chapters.

Chapter 1 – Presents the motivation and scope of the thesis.

Chapter 2 – Presents a literature review on the corrosion of steel, focused mainly on corrosion in the presence of AC.

Chapter 3 – Presents the material specifications, sample size and experimental set up, procedure and method.

Chapter 4 – Presents the acquired results.

Chapter 5 – Presents a detailed discussion of results and experimental work together with suggestions for further work.

Chapter 6 – Presents the conclusions of the thesis.

2 Theory

The theory chapter is divided into three main parts. The first part consists of two chapters and presents the Direct Electrical Heating-system (DEH) and its history and purpose. This is followed by a general review of DC corrosion and its mechanism in absence of AC. The last part is a thorough and up-to-date literature review of AC corrosion, containing its mechanism and the most relevant of former work. All this is summarized in the last chapter.

2.1 History

The offshore industry is moving towards an increased number of subsea structures. The structures can be wells and whole processing-systems, and they are connected to offshore or land-based installations with long pipes reaching out to each structure or clusters of several structures. When the oil and gas exits the well or manifold and are pumped towards the installation, it is under high pressure and temperature. In order to avoid too much heat loss so that the product can flow without problems, the several kilometer long pipes are insulated. However, during a production shutdown the insulation will not be able to keep the temperature high enough, and formation of wax and hydrates is likely to cause plugging as seen in Figure 2-1 [1]. As the industry is heading towards production at deeper waters and in the arctic environment, it is possible that the insulation that is in use today will prove insufficient, and plugging may occur during regular production.

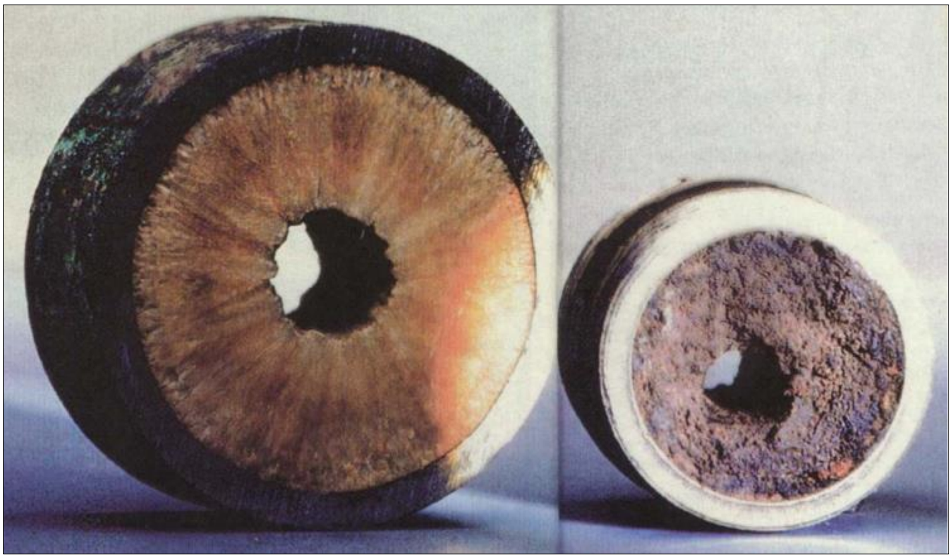

Figure 2-1: Cross-sections of two plugged pipelines [6].

For both environmental- and economic reasons such plugging is unwanted, and an often-used method to avoid it have been to add different chemicals, for instance methanol, to the transported medium [7]. This has worked well enough, however it is expensive and it has been necessary to separate the chemicals from the medium upon arrival at the platform. This is yet another processing step and more potential hazardous waste [8]. In 2000, Nexans installed an alternative to the use of chemicals; the world's first Direct Electrical Heating-system (DEH). This was done for Statoil at the Åsgård-field at the Haltenbank west of Norway. In the aftermath, more DEH-systems have been installed at new fields like Skarv, Tyrihans and Ormen Lange to name a few [1].

2.2 Direct Electrical Heating (DEH)

The DEH-system is a set of electrical conducting cables that sends an electrical signal from a power source on the platform to the pipelines at the sea bottom. The mechanism that avoids the plugging of the pipelines is that this signal, which is sent as an alternating current (AC), flows through the pipe-walls and heats them up due to their own electrical resistance. There exists several systems similar to Nexans' DEH-system, but the latter is based on pipelines in open seawater and consists of three different types of cables as seen in the red rings in Figure 2-2, from left to right: riser cable, armoured feeder cable and piggyback cable [1].

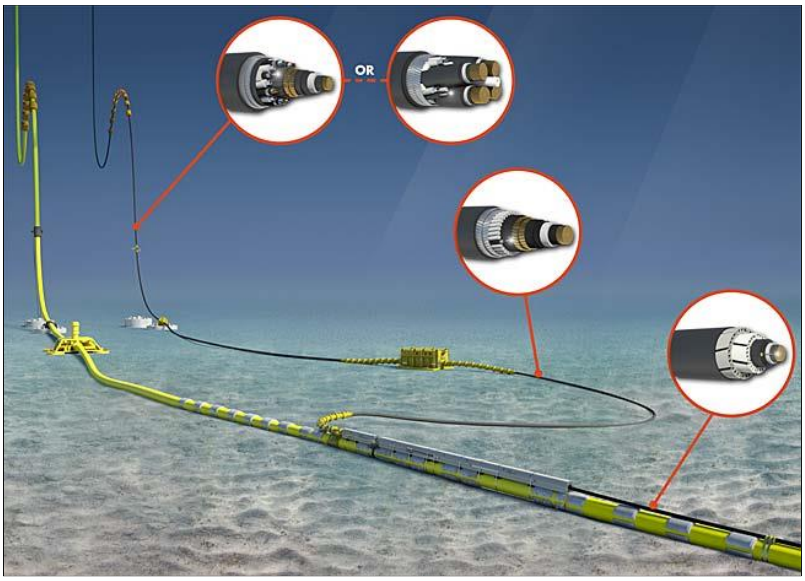

Figure 2-2: Illustration of Nexans' DEH-system with the different cable types [1].

The riser cable supplies power from the platform to the seabed and can be used for several piping-systems at the same time. It may also include hydraulic tubes and signal cables. The armoured feeder cable acts as a connector and connects the riser cable and the piggyback cable at the seabed. The piggyback cable is strapped tightly to the pipeline and conducts the current along it until the connection-point at its far end. The piggyback cable also contains a fiber-optic system for monitoring and is surrounded by an IPS (Integrated Protection System), which protects it from external loads and abrasion. To summarize, the current go from the power supply through the riser cable, armoured feeder cable, piggyback cable and into the pipeline at its far end. Then the current go through the pipeline (and eventually feeder- and riser cable) on its way back to the platform or installation [1].

The pipeline that is heated is an active conductor in a single-phase electric circuit, where the piggyback cable is the forward conductor. The DEH-system is necessarily an open system, which means that it is in contact with the surrounding seawater as can be seen in Figure 2-3. The contact is through an increased amount of anodes at the points where the current enters and leaves the pipeline. The consequence of an open system is that the seawater acts as a conductor, which causes the pipeline and seawater to share the current (although it does not lie parallel and close to the pipe as in Figure 2-3, but stretches out through the whole volume of the sea). This means that a part of the current (typically around 40 %) is transferred into the seawater, either as products from the oxidation of anodes or through charging and discharging of the double layer capacitance [4, 6, 7, 9].

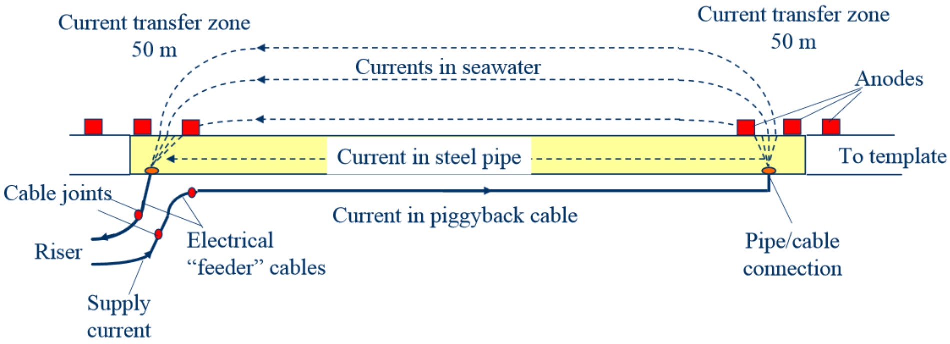
Current transfer zone
50 m
Current transfer zone
50 m
Currents in seawater
Anodes
Current in steel pipe
To template
Cable joints
Current in piggyback cable
Riser
Electrical
"feeder" cables
Pipe/cable
connection
Supply
current

Figure 2-3: Schematic view of the DEH-system with current directions included [6].

Earlier studies on AC-corrosion has shown that there is no significant corrosion of carbon steel as long as it is protected by anodes, and the applied current density is below 240 A/m^2. It is especially important to have enough anodes in the current transfer zone and in areas where cracks in coating and insulation can occur, to keep the transfer current density below critical values (in the study by Nysveen et al., the critical value of the transfer current density is set to 40 A/m^2) [7].

2.3 Corrosion behavior in absence of AC

2.3.1 General corrosion behavior

2.3.1.1 The equivalent circuit

An electrochemical cell can be described as an equivalent electrical circuit consisting of resistances, capacitances and impedances. This equivalent circuit acts as a model for the interface between the metal surface and the surrounding electrolyte and can be seen in Figure 2-4, which is a model based on the Randles circuit. In the figure, R_e represents the ohmic resistance or potential drop of the electrolyte, C_{dl} refers to the capacitance associated with the double-layer, R_f is the charge transfer resistance and Z_d represents the impedance for mass transport [10].

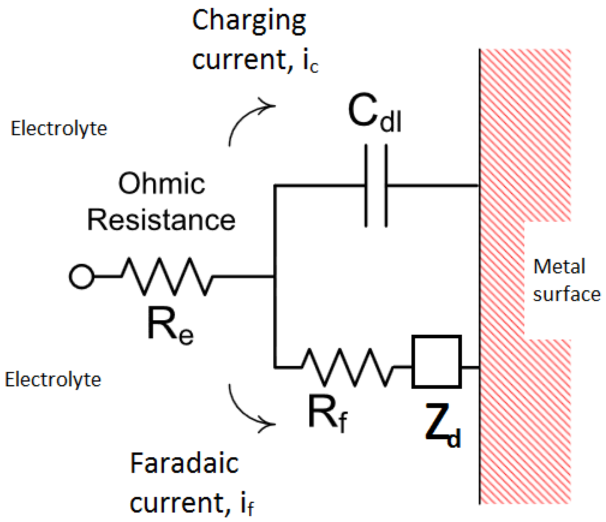

Figure 2-4: The equivalent electrical circuit that acts as a model for the interface between the metal surface and the surrounding electrolyte. Figure is adapted from literature [11].

The capacitance at the double layer (C_{dl}) arises due to charge redistribution at the interface, or from a dielectric oxide-film on the metal surface. It may act as a capacitor, and parts of any current that flow between electrolyte and the metal surface will cause charging or discharging (both will be i_c) of the double layer. R_f and Z_d on the other hand, are combined to an impedance called the polarization resistance. This resistance correlates to overpotential that is created by the concentration gradients of reactants and products, which are formed due to the flow of the Faradaic current, i_f. This current, dependent on its direction, causes oxidation of the metal surface and formation of other products due to oxidation [10, 12].

The model in Figure 2-4 implies that the total current that flows between the metal surface and the electrolyte, is a combination of the Faradaic- and charging current where both contributions are equal:

$$i = i_c + i_f \tag{2.1}$$

2.3.1.2 Uniform corrosion

Two reactions on the metal surface are necessary for the metal to corrode, the cathodic- and the anodic reaction. It is the sum ΔG for both reactions that determine which way the total reaction will be favored, or in other words if corrosion will occur or not. The potential at which corrosion will occur is called the corrosion potential (E_{corr}). This potential can be analyzed in a Pourbaix diagram as shown in Figure 2-6, which is a pH-potential plot that shows where different corrosion products of a metal are thermodynamically stable. This means that by studying the Pourbaix diagram, it is possible to determine if a corrosion-reaction will occur or not. However, that is the case if the only anodic reactions that occur on the surface, is directly causing the corrosion. In reality, there are several different reactions going on simultaneously, and all of them are not necessarily causing corrosion [13].

In the case for uniform corrosion, the anodic- and cathodic reaction occurs all over the surface, which gives an even reduction in thickness. A lot of research has been done on uniform corrosion of steel in aqueous solution, and numerous mechanisms have been proposed. However, if it is assumed that OH^- is the active adsorption anion in the anodic reaction (due to lack of other active adsorption anions), it is generally agreed that the initial stages of oxidation proceeds through the following equations [14, 15]:

$$Fe + H_2O = FeOH_{ADS} + H^+ + e^- \tag{2.2}$$

$$FeOH_{ADS} = FeOH^+ + \ e^- \tag{2.3}$$

Which are followed by the following stages [15]:

$$FeOH^+ = Fe^{2+} + OH^- \tag{2.4}$$

$$FeOH_{ADS} + OH^- = Fe(OH)_2 + e^- \tag{2.5}$$

However if Cl^- ions are present, there will be a competition between them and OH^- at the surface adsorption sites. Which precipitates that are formed, are determined by the relative concentration between OH^- and Cl^- ions, and in solutions dominated by the latter it is more likely that $FeCl_{ADS}$ and Fe(OH)Cl will form instead of the above mentioned. At high concentrations of Cl^-, the Fe^{2+} ion can exist in several ferrous-chloride complexes like $FeCl^+$, $FeCl_2$, $FeCl_3^-$, etc. [14].

If the solution is alkaline, $Fe(OH)_2$ may oxidize and form the more stable magnetite, according to the Schikorr reaction (2.6) as seen below [14].

$$3Fe(OH)_2 = Fe_3O_4 + H_2 + 2H_2O \tag{2.6}$$

Other possible reactions like (2.7) and (2.8) may also occur if the solution is aerated and Cl^- ions are present.

$$2OH^- = \frac{1}{2}O_2 + H_2O + 2e^- \tag{2.7}$$

$$2Cl^- = Cl_2(g) + 2e^- \tag{2.8}$$

The corresponding reduction reactions that commonly occur are shown in equation (2.9)-(2.11) below, where (2.10) will occur in an alkaline solution and (2.11) is for an acidic solution [16].

$$\frac{1}{2}O_2 + H_2O + 2e^- = 2OH^- \tag{2.9}$$

$$2H_2O + 2e^- = 2OH^- + H_2\,(g) \tag{2.10}$$

$$2H^+ + 2e^- = H_2\,(g) \tag{2.11}$$

2.3.2 Localized corrosion behavior

Pitting is a form of localized corrosion that occurs on surfaces that have some degree of passivation, through alloying elements or supplied current. Further, the surfaces need to be exposed to a medium with aggressive ions, like chlorides, and the potential of the surface must be above a certain critical value. Pitting is characterized by holes or caves that can become very deep even though their surface-diameter is small.

The initiation of pitting is caused by a local breakdown of the passive film, which occurs at sites where the film is weaker than the surrounding area. There are several explanations to why these weak sites occur, where chemical composition and mechanical influence are two possible explanations. After initiation, the main propagation-mechanism is that the pits get minimum mixing with the bulk electrolyte and thus the pits create their own environment.

The pitting propagation proceeds through several processes that occur continuously. Firstly, the formed pit corrodes uniformly with anodic dissolution and the reduction of oxygen as the cathodic reaction (eq. 2.9). Gradually, oxygen will be removed as it is reduced faster than it diffuses into the tight pit. This concentration-difference of oxygen will transform the metal surface to a cathode and the pit to an anode, which will maintain the metal dissolution within the pit. As the concentration of metal-ions increases, there will be a charge unbalance, with many positive ions within the pit. To have balance, aggressive ions (particularly chlorides) migrate into the pits and form metal-chlorides, which again produce H^+ ions through hydrolysis. This causes the environment to become increasingly acidic, which increase the dissolution even further within the pit.

N. Sato distinguishes between two different types of pitting corrosion as can be seen in Figure 2-5; etch and polish. The etch pitting occurs at low potentials when the pit surface is in the active state, while polish pitting takes place at high potentials when the pit surface is under transpassive dissolution and usually covered with a salt layer [17].

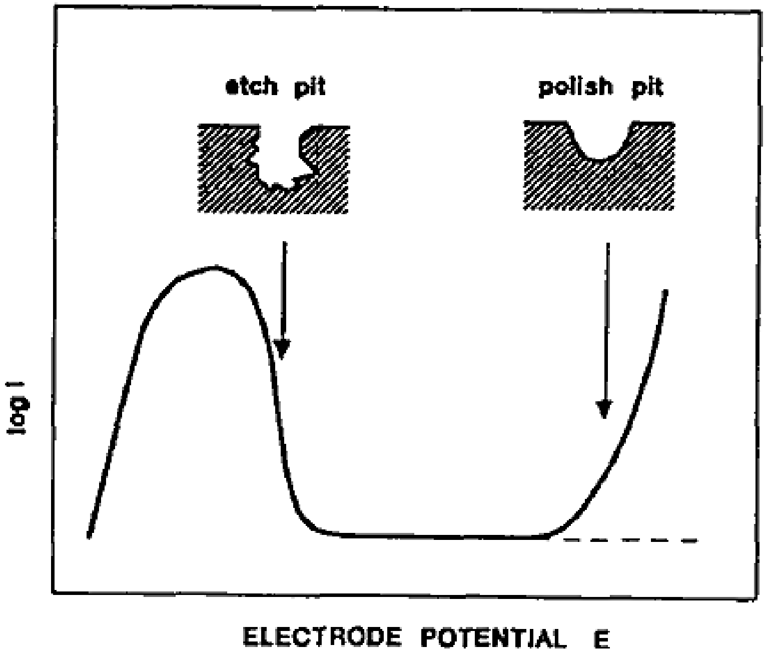

Figure 2-5: Two types of pitting described by N. Sato.; etch pitting at low potential in active state and polish pitting at high potentials with transpassive dissolution at pit surface [17].

2.3.3 Cathodic Protection

The main principle of cathodic protection is to supply a current on the material that is to be protected. The current reduces the potential of the material into the immune area, as shown in Figure 2-6, and more or less removes the danger of corrosion completely. It is worth noting that the pourbaix-diagram in Figure 2-6 is in water and not in a chloride-rich environment, but a similar diagram for the latter should not be too different. The reduction of potential into the immune area is called cathodic polarization, and can be done with sacrificial anodes or by applying current from an outer current rectifier. The latter is more relevant for this thesis, as a potentiostat is being used.

According to NORSOKs standard, an installation should be polarized to a potential between -800 mV and -1050 mV vs the Ag/AgCl reference electrode throughout the whole design life to be protected [18]. Det Norske Veritas’ (DNV) Recommended Practice states that a potential of -800 mV vs the Ag/AgCl reference electrode is accepted for carbon and low-alloy steel, although this should be increased to -900 mV in anaerobic environments [19]. The difference between Ag/AgCl reference and Standard Calomel Electrode (SCE) is -0,042 V (-42 mV), which means that -800 mV Ag/AgCl is approximately -760 mV SCE [20].

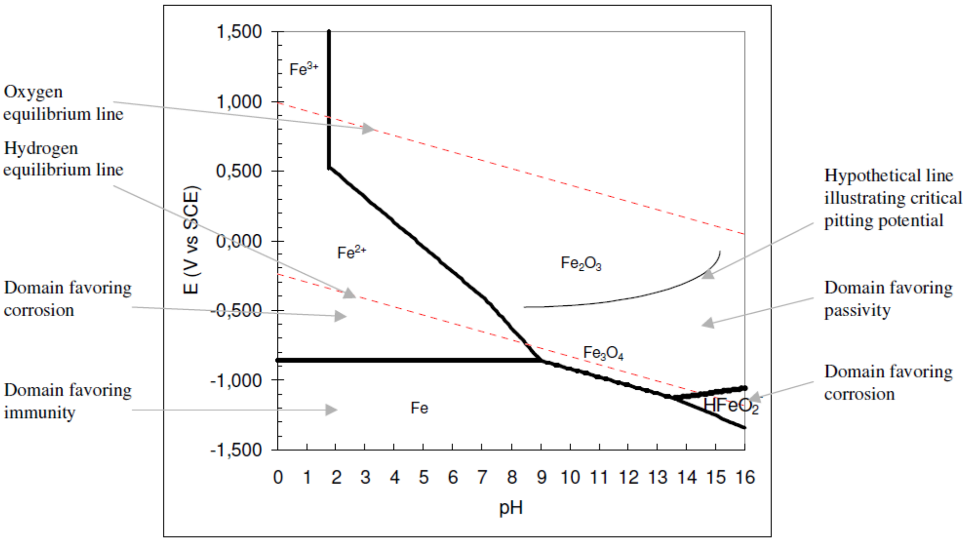

Figure 2-6: The Pourbaix diagram for iron/carbon steel in water. The active corrosion, immune and passive regions are indicated, as well as the critical pitting potential [21].

2.3.3.1 Calcareous deposits

When steel structures are immersed in seawater and under CP, it is known that calcareous deposits will form at the steel surface. They form due to a cathodic current that increases the local pH by producing OH^- ions. Deposits may form through a reaction between these ions and cations in the seawater, precipitating the product at the steel surface, or through other reactions and precipitations. It is recognized that these deposits serve as parameter that reduces corrosion in marine environments, with or without CP, partly due to reduced diffusion of oxygen from bulk to steel surface. The deposits that are most likely to occur are $Mg(OH)_2$, equation (2.12), and $CaCO_3$ seen in equation (2.13)-(2.16) [22].

$$Mg^{2+} + 2OH^- = Mg(OH)_2 \tag{2.12}$$

The reason why only magnesium deposit as a hydroxide is that $Mg(OH)_2$ has lower solubility than $Ca(OH)_2$, and there are more Mg^{2+} ions in seawater than Ca^{2+} ions. Furthermore, $MgCO_3$ have higher solubility than $CaCO_3$ and thus the latter precipitates easier. The formation of $CaCO_3$ is seen below and is initiated by a reaction between atmospheric CO_2 and water. All the reactions are dependent on a local increase in pH [22].

$$CO_2 + H_2O = H_2CO_3 \tag{2.13}$$

$$H_2CO_3 = H^+ + HCO_3^- \tag{2.14}$$

$$HCO_3^- = H^+ + CO_3^{2-} \tag{2.15}$$

$$CaSO_4 + CO_3^{2-} = CaCO_3 + SO_4^{2-} \tag{2.16}$$

It has further been shown that the precipitation rate of deposits is very high at the beginning of CP, and is reduced and keeps on reducing as time passes. The growth rate reaches its peek at approximately 8 hours of CP, although this does not mean that the steel surface is completely covered after 8 hours. Further, $Mg(OH)_2$ is formed with faster kinetics than $CaCO_3$ and thus is the major component at the early stages of CP. However, as polarization time prolongs, the amount of the $CaCO_3$ increases and becomes the major component [23].

2.3.4 Immersion testing in 3.5 % NaCl-solution and seawater

Natural seawater is a very complex chemical system that is affected by other factors than the major components, like dissolved oxygen, pH and biological activity to name a few. It has even been experienced that it changes in corrosivity from the bulk seawater upon storage. In other words, it is difficult to simulate seawater in a laboratory. 3.5 % NaCl-solution have often been used, but has been known to be more aggressive toward carbon steel than natural seawater. The reason for this has been suggested to be the presence ions in seawater, which form the mentioned calcareous deposits. A cross between the 3.5 % NaCl-solution and natural seawater, is synthetic seawater produced from the standard ASTM D1141 or MBL [24].

Another factor that causes 3.5% NaCl-solution to be more aggressive than seawater is the seawater’s buffer capacity. A NaCl-solution has low buffer capacity and easily gets local variations in pH, which increases both corrosion rate and danger of pitting. Seawater on the other hand has high buffer capacity due to equilibrium between different ions (like carbonates and CO_2), and are thus able to keep a stable pH to a larger degree [4].

Through experiments with simple immersion testing and potentiodynamic measurements, Moller et al. found that the corrosion rate of low carbon steel in 3.5 % NaCl-solution is about four times higher than for natural seawater, and that the corrosion rates in natural- and synthetic seawater is similar. They also found different corrosion products between the seawaters and the 3.5 % NaCl-solution. In the latter the corrosion-layer consisted mainly Fe_3O_4 (magnetite) and γ-FeOOH (lepidocrocite), while for the seawaters it was mainly found γ-FeOOH. This was explained with the higher corrosion rates in 3.5 % NaCl-solution that gives a higher concentration of Fe^{2+} at the steel surface, which again can react according to equation (2.17) below [24].

$$Fe^{2+} + 2FeOOH = Fe_3O_4 + 2H^+ \tag{2.17}$$

Further, it was also found small amounts of α-FeOOH (Goethite) and $Fe_6(OH)_{12}CO_3$ (Iron carbonate hydroxide). Additionally, $CaCO_3$ were formed on both seawaters although with finer morphology for the natural seawater, which is the probable cause for a slightly lower corrosion rate. Magnesium-containing deposits were difficult to detect. [24].

According to DNV’s standard for pipelines, 25Cr duplex is generally corrosion resistant in seawater at ambient temperatures, but requires good control of microstructure. 316 on the other hand is not corrosion resistant in seawater with the same parameters, with exception if the seawater is near to anaerobic conditions [25].

2.4 AC-induced corrosion

It has been acknowledged that corrosion of bare steel accelerates in the presence of AC. However, if the steel is under CP by anodes or protected by an intact coating, AC corrosion is not considered a problem. The problem occurs if CP is applied by a rectifier, there are micro- or macroscopic defects in the coating, or if unprotected structures suffer from stray ACs [3-5]. Most of the research that exist on AC-induced corrosion, have investigated how CS and other low-alloyed steel are affected [26-32]. There is little research done on different types of SSs [26, 27].

2.4.1 AC corrosion mechanism

The AC-signal that is sent varies between negative and positive values periodically, at a certain frequency. This periodic function is often sinusoidal. When the AC-signal is superimposed on a DC-signal, the AC-signal will alternate between what is defined as anodic and cathodic currents on each side of a time-axis, as seen in Figure 2-7. The DC-signal determines the position of the time-axis and thus the area of both the anodic and the cathodic cycle. If the AC is applied on a high DC, the time-axis move up and reduces the area of the anodic cycle, and vice versa for low DC.

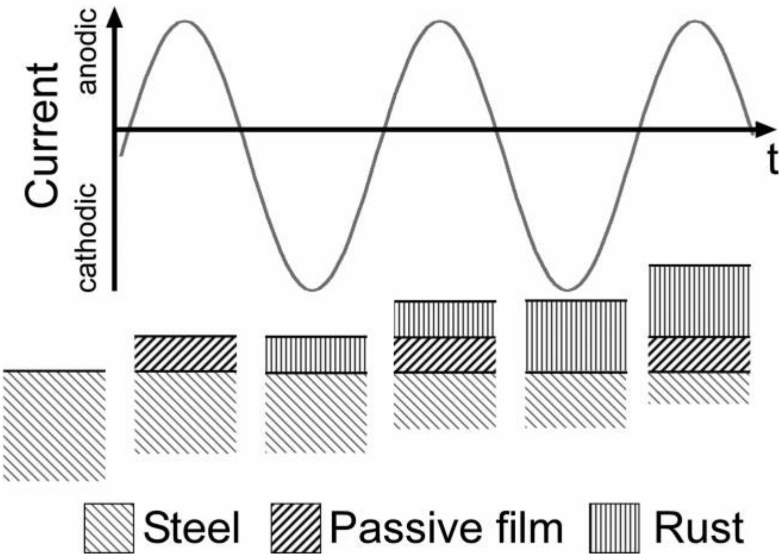

Figure 2-7: Schematic view of the AC corrosion mechanism when samples are under CP ($i_{DC} > 1A/m^2$), with graph and illustrations [33].

The anodic and cathodic cycle affects the steel in different ways, and the amplitude of the AC voltage is an important parameter in determining what happens. Possible scenarios during the anodic half-cycle: a current may "exit" (in the form of oxidized products) the steel surface and the charge can lead to capacitive discharging of the double layer, the oxidation of hydrogen, the oxidation of corrosion products and oxidation of iron. The latter often leads to formation of a passive film due to high pH at the steel surface. Conversely, the charge in the cathodic cycle is consumed by recharging of the double layer capacitance, the reduction of oxygen, the formation of hydrogen and the reduction of oxidized corrosion products. It can also polarize the anodic formed passive film into the immune area, thus dissolving it electrochemically [34].

More specifically, for a case with a certain CP ($i_{DC} > 1\ A/m^2$) as in Figure 2-7, the anodic cycle causes the steel surface to be oxidized by the current "leaving" the steel surface, leading to the formation of a protective passive film according to reaction (2.18) [33, 34].

$$3Fe + 4H_2O \rightarrow Fe_3O_4 + 8H^+ + 8e^- \tag{2.18}$$

$$Fe^{2+} \rightarrow Fe^{3+} + e^- \tag{2.19}$$

In the next cycles, it is assumed that the current may be divided, thus it is possible that several reactions occur in each cycle (including dis- and recharging of double layer). During the first cathodic cycle, a part of the current causes the steel surface to polarize into the immune area, reducing the passive film electrochemically and converting it to a porous layer of rust, as Fe^{2+}. Other parts of the current may drive typical cathodic reactions, like evolution of H_2 and reduction of oxygen as seen in equation (2.9)-(2.11). During the following anodic cycle, a new passive film is formed below the porous rust layer and Fe^{2+} in the rust layer will be oxidized according to reaction (2.19). Additionally, parts of the current may drive the formation of O_2 and Cl_2, as in equation (2.7) and (2.8), where the latter has been observed in earlier studies [27, 35]. During the subsequent cathodic cycle, passive film will be converted again, and reaction (2.19) will be reversed in the rust layer, forming more rust as Fe^{2+}. This is a continuous process. Each time a new passive film is formed a small amount of steel is oxidized. Thus, corrosion is a result of repeatedly formations of passive films, and not anodic metal dissolution [33, 34, 36].

In addition, due to high AC-voltage it is possible that a solid-state reaction occurs, according to equation (2.20). If it occurs, it may do so in both the anodic- and cathodic cycle. The reaction can move in both directions depending on the cycle, which correlates to the current moving back and forth in the faradaic part of the equivalent circuit. In the anodic cycle the reaction will be favored to the right, while it will be favored to the left in the cathodic cycle [13, 36].

$$2Fe_3O_4 + H_2O = 3Fe_2O_3 + 2H^+ + 2e^- \qquad (2.20)$$

A partly similar mechanism as in the paragraphs above is described by D.-K. Kim et al. They suggest that the combination of applied AC and an elevated pH, leads to corrosion either by a destabilization of the passive layer or by a very high increase in pH. For the latter case, the steel enters the active corrosion area of $HFeO_2^-$ as can be seen in the Pourbaix diagram in Figure 2-6. The first case is explained by the irreversibility of the chemical reactions that occur on the metal-solution interface, which leads to a change in the double layer composition and metal surface [29].

It is worth noting that S. Muralidharan et al. performed experiments by applying a certain current density (as DC, AC or both) on mild steel in chloride rich environments. They reported that the influence of AC current density superimposed in the same current density in DC, were far more severe than either AC or DC alone. The corrosion rate of AC+DC in NaCl-solution was 1.5 times higher than only DC and 18 times higher than AC alone [32].

2.4.2 Influences on AC corrosion

2.4.2.1 Frequency

Immersion testing with mild carbon steel in synthetic seawater with purged oxygen performed by M. A. Pagano et al., found that the frequency of applied AV affected the AC corrosion rate. They tested frequencies in the area 5-500 Hz and stated that increases in frequency leads to a drop in corrosion rate. It is also worth noting that at high frequencies, corrosion rates for high AVs are similar. They explained these results with a significant decrease in the impedance of the double layer. Due to this decrease, only small fractions of the current flows through the polarization resistance, and this lead to a lower corrosion rate. Another thing is that at lower frequencies, Fe^{2+}-ions diffuse into the solution faster than the polarity of the working electrode changes, which means that there are less Fe^{2+} available for redeposition [31].

Through a study of electrochemical dissolution of platinum by potentiostatic and galvanostatic techniques with applied AC, G. Benke and W. Gnot determined that the highest rates of platinum dissolution occurs at frequencies close to 50 Hz [37]. Another study by Y. Hosokawa et al. that monitored ACs on a pipe steel, determined that a frequency of 50 Hz had the worst effect on AC corrosion [2].

2.4.2.2 Potential

M. A. Pagano et al. found that the amplitude of the applied AV affected the corrosion rate. As seen in Figure 2-8, the corrosion rate increases rapidly with increasing AV, although with a slight fall in corrosion rate at potential between 100 and 600 mV (corrosion rates between these voltages are still higher than with no applied voltage). It was stated that this fall in corrosion rate was due to passivation of the carbon steel. As the voltage was increased, hydrogen evolution caused the pH in the diffusion layer to increase, which formed a protective oxide layer. At voltage higher than 600 mV, the oxide layer was broken down and corrosion rates increased rapidly again [31].

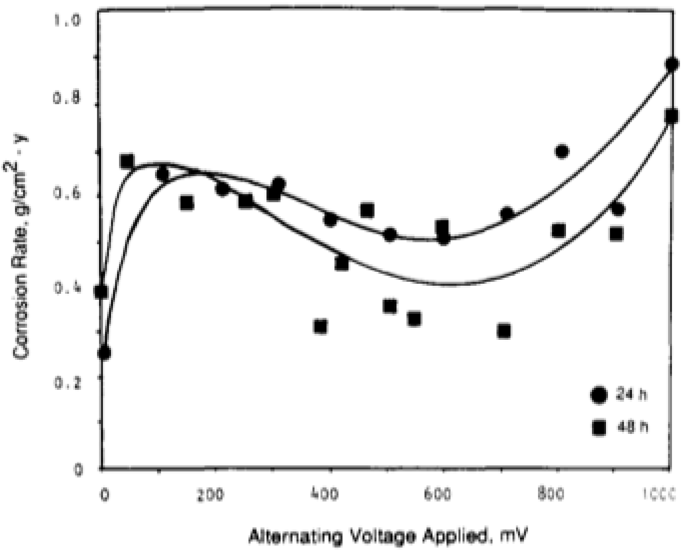

Figure 2-8: Corrosion rate as a function of applied AV. Experiments at room temperature, O_2 removed and at a frequency of 60 Hz [31].

C. H. M. Hagen measured V_{AC} (AC cell potential) between working electrode and AC counter electrode, and found that it was higher for SS compared to CS and where 25Cr were higher than 316 [26].

2.4.3 Potential behavior in an open circuit

D. Kuang and Y. F. Cheng performed experiments to determine the effect of different coating defects on AC corrosion. The experiments were performed without applied DC on X65 carbon steel, immersed in deoxygenated bicarbonate solution with near-neutral pH. A part of their results can be seen in Figure 2-9 [5].

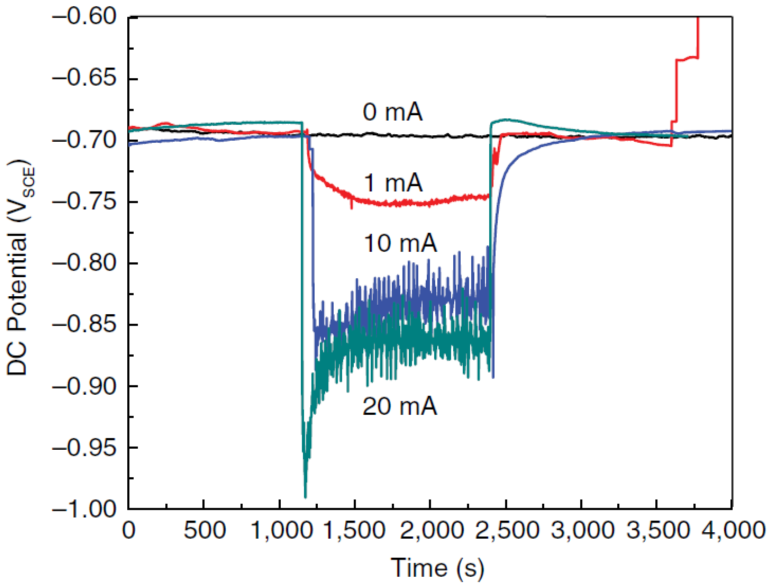

Figure 2-9: Recorded DC potential as a function of time with various AC applied. Recorded at a steel sample with a circular coating defect with a diameter of 5 mm [5].

The figure shows a steel sample that is immersed in the solution with different levels of applied AC. As no DC is applied, the recorded values are the corrosion potential (E_{corr}) of the sample, and can be divided into three regions: before applied AC, with applied AC and after applied AC. As the DC is measured at a coating defect with 5 mm in diameter, the applied AC current density from highest to lowest will be approximately: 1000, 500 and 50 A/m^2. One can see that the applied AC increases the E_{corr} in negative direction, and that the values pre- and post-AC is more or less the same. The DC values of -0.8 V vs SCE that occur for 10 and 20 mA applied AC, resembles a regular CP-system. However, the steel samples were not protected at this potential, as they were reported to suffer from corrosion. It is thus likely that a regular CP-system is unable to protect a structure that is in contact with AC. A probable cause for this is the oscillating nature of the AC. This could also mean that a sample that is under CP of approximately -0.8 V vs SCE would possibly suffer from more severe corrosion, due to being in the active corrosion area together with an oscillating AC [5].

2.4.4 Corrosion kinetics

Several studies have reported that the corrosion kinetics is affected when AC is applied [38-40]. However, it has been debated whether it is the cathodic- or anodic overpotential that suffers a change when AC is applied. S. Goidanich et al. suggested that the reduction in overpotential were higher for the cathodic reaction, and explained it with a change in the double layer chemical composition [39]. L. Lazzari et al. on the other hand concluded through studies in different simulated soil solutions, that both the cathodic- and anodic reaction are affected, as can be seen in Figure 2-10 and Figure 2-11 [40].

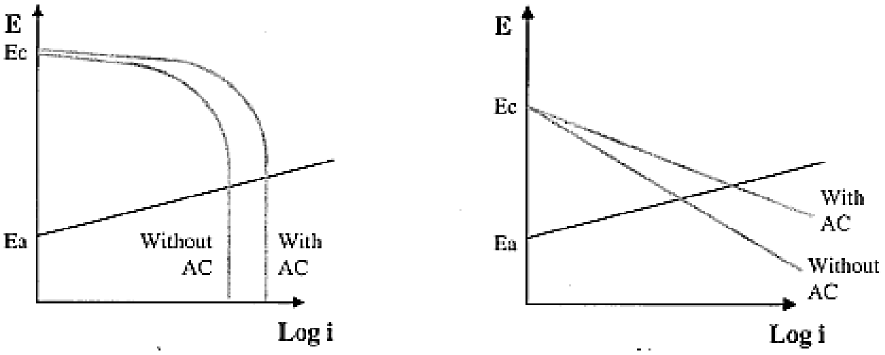

Figure 2-10: Schematic effect of AC on cathodic overpotential. Left illustration indicates effect on oxygen reduction, the right one indicates effect on hydrogen evolution [40].

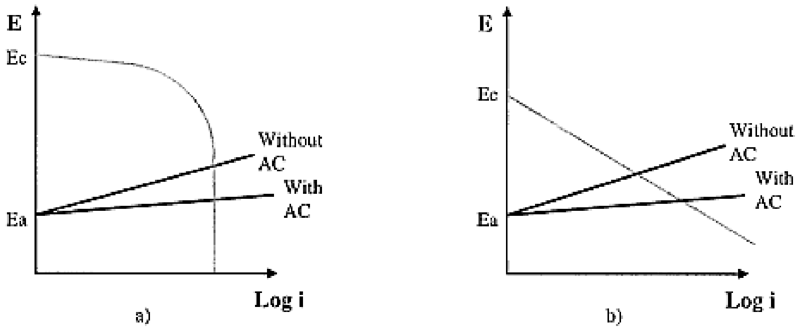

Figure 2-11: Schematic effect of AC on anodic overpotential. Where the cathodic reaction at a) and b) is oxygen reduction and hydrogen evolution, respectively [40].

At high current densities, several studies have reported an enhanced hydrogen reaction at high AC current densities [41, 42]. L. Lilleby et al. performed experiments at SMSS in 3.5 % NaCl-solution and reported that the oxygen reduction reaction disappeared from the polarization curves at high AC, leaving the evolution of hydrogen as the cathodic reaction [43]. This was acknowledged by C.H.M. Hagen’s studies in 3.5 wt% NaCl-solution, were it was concluded that hydrogen evolution is the controlling cathodic reaction for different SSs (316 and 25Cr SDSS) at $i_{AC} > 100$ A/m^2 [26, 44].

2.4.5 Current behavior under cathodic protection

Through immersion testing of a sheet of 16Mn steel pipe in a test solution simulating soil solution with a pH of 8.95 and connected to a potentiostat, L.Y. Xu et al. found that applied AC affected the CP of the steel as can be seen in Figure 2-12 and Figure 2-13. The DC-potential is maintained and the regions have the same meaning in both figures: CP-I and CP-II/CP-2 are when only DC is applied. CP+AC mean that various AC current densities are superimposed on the DC. By other words, DC is maintained at a constant voltage and AC is applied at the CP+AC-region [30].

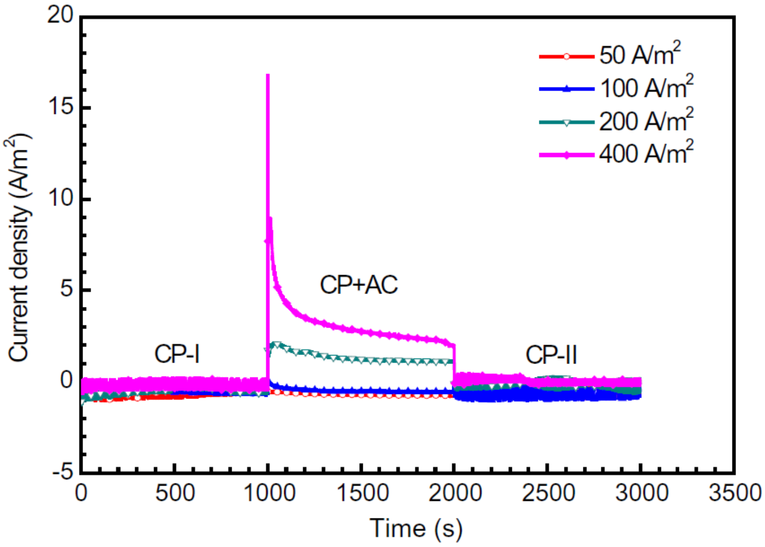

Figure 2-12: Recorded DC current density as a function of time with various AC applied. The steel sample is polarized potentiostatically at -0.85 V vs SCE [30].

As Figure 2-12 shows, the DC current density is close to zero and equal both before and after AC is applied. When AC is applied in the CP+AC-region, a positive shift is seen in the current density. This positive shift means that the current density becomes anodic, which is attributed to oxidizing of the steel anodically and thus enhanced corrosion. For applied AC less than 100 A/m^2 there is a slight change in anodic direction. For higher AC however, there is a bigger difference. Moreover, as the applied AC increases, the more anodic the DC current density becomes [30].

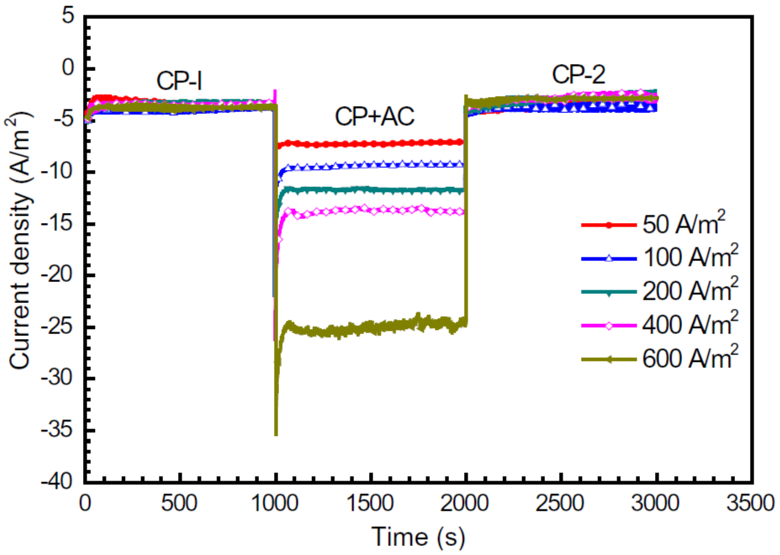

Figure 2-13: Recorded DC current density as a function of time with various AC applied. The steel sample is polarized potentiostatically at -1 V vs SCE [30].

Figure 2-13 also shows equal DC current density before and after AC has been applied, although at approximately -4 A/m^2 which means full CP-protection. When AC is applied, the DC current density drops instantly and stabilizes at a current density that is much lower than originally. Further, as applied AC increases, the more negative the DC current density becomes. This drop in current density indicates that it becomes cathodic, which means that the DC-potential increases and the cathodic reaction and electron consumption is enhanced. With these results and weight loss measurements performed, L. Y. Xu et al. concludes that applied AC reduces the effectiveness of CP. Although, corrosion is at an acceptable level at sufficient negative CP (-1 V vs SCE) and reasonably low AC (i_{AC} < 400 A/m^2). Additionally, they point out that the AC affects the CP potential readings. For instance when CP is applied by constant current or voltage, the readings will be shifted either negatively or positively, not necessarily representing the CP-system [30].

Other studies have reported results that only coincide partly to these findings. C. H. M. Hagen performed similar study on 316 and X65 in 3.5 % NaCl-solution. The deviation from the findings by L. Y. Xu et al. is that it was reported that the DC current density for X65 in -800 mV DC vs SCE, shifted to positive values for a short period only, before turning to negative and cathodic values. This is visualized in Figure 2-14. For -1050 mV vs SCE however, results were in accordance with L. Y. Xu et al. This was acknowledged by C. B. Esser, who tested in artificial seawater, and A. Bergin, who tested in both solutions [26, 27, 35].

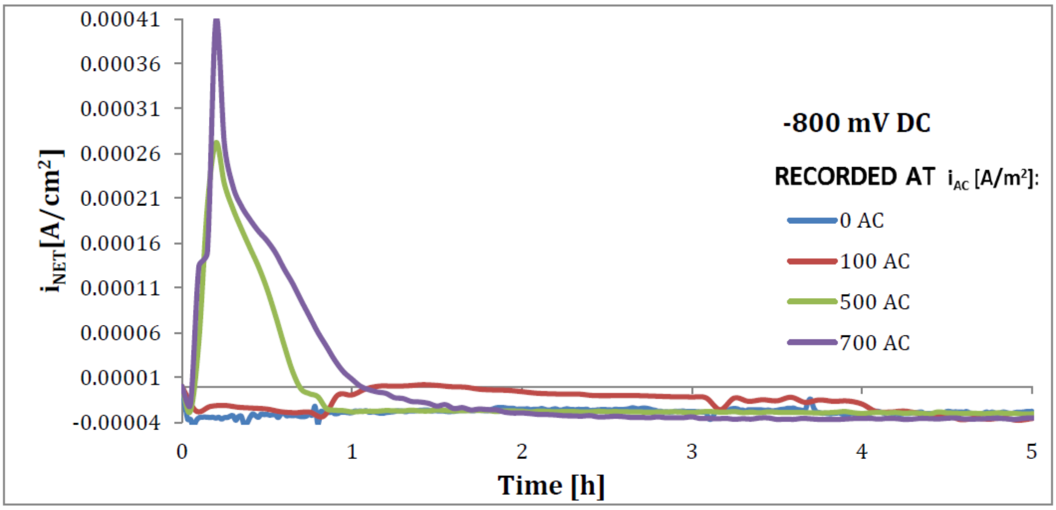

Figure 2-14: Recorded DC current density as a function of time, for X65 in -800 mV DC vs SCE for different AC current densities. First five hours of a total 48 hour long experiment [26].

C. H. M. Hagen integrated the short period of positive values over a time integral, and the charge corresponding to this period was calculated. Then it was discovered that the final weight loss was much higher than the weight loss from this charge. Thus, dissolution of the steel happens during the whole experiment (despite negative DC current response) and is not related to the positive values at the beginning [26].

For 316, C. H. M. Hagen reported a negative current response for both -800 mV and -1050 mV vs SCE, where the values stabilized at less negative values than the values initially. This was confirmed by C. B. Esser [26, 27].

2.4.6 Weight loss and corrosion rates

2.4.6.1Carbon steel

D.-K. Kim et al. performed AC-corrosion experiments with mild steel, at a frequency of 60 Hz and under CP in 3.5 % NaCl-solution and natural seawater. They discovered for both solutions, that there were no corrosion in the absence of AC, but as AC was applied an increase in AC current density lead to an increase in corrosion rate. This was the case for both CP-potentials. They explain this by destabilization of the passive layer that occurs because of the electrochemical reactions. For a AC current density of 100 A/m^2, the corrosion rate was in the area of 0.98-0.99 mm/y for a CP-potential of -780 mV vs. SCE and 0.15-0.17 for a CP-potential of -1100 mV vs. SCE. In addition, the corrosion rate was higher for the 3.5 % NaCl-solution compared to natural seawater [29]. The latter is in contrast with A. Bergin’s study, which concluded that there was little or no difference between 3.5 % NaCl-solution and artificial seawater [35].

L. Y. Xu et al.’s experiments in simulated soil solution, as seen in Figure 2-15, reported complete protection from corrosion (defined as CR < 0.1 mm/y) at a CP-potential of -1 V vs

SCE. If applied AC was below 100 A/m^2, complete protection was the case for a CP-potential of -0.85 V vs SCE as well [30].

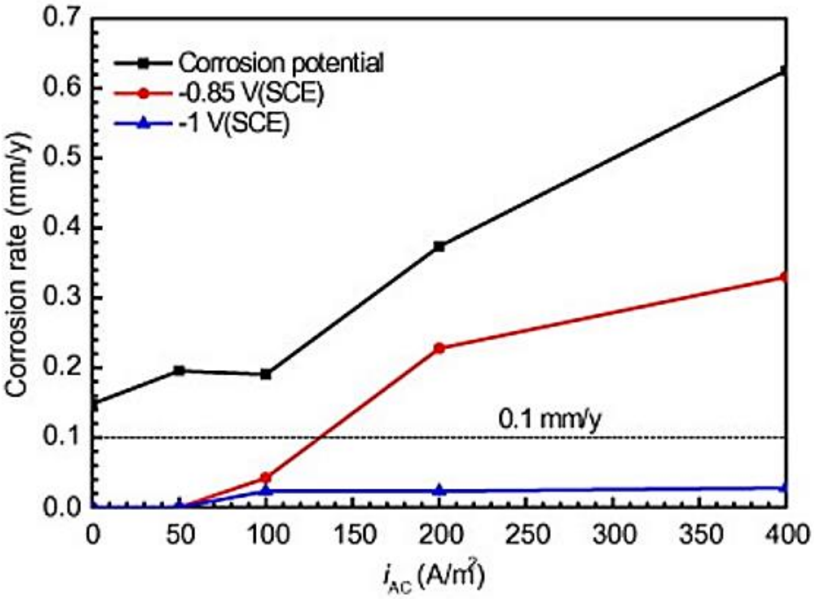

Figure 2-15: Corrosion rate as a function of applied i_{AC} under different CP-potentials. Determined by weight loss measurements of steel immersed in simulated soil solution [30].

C. H. M. Hagen reported corrosion rates in the area 0.115-0.205 mm/year depending on AC current density at a CP-potential of -800 mV vs SCE in 3.5 % NaCl-solution. With the peak CR at 500 A/m^2 AC. Similar for a CP-potential of -1050 mV [26]. C. B. Esser found somewhat higher CR in artificial seawater; in the area 0.57-1.16 mm/year [27]. Significantly higher was the CR reported by A. Bergin, with the peak at 27.4 mm/year. It was proposed that a rougher surface roughness, storage of the samples prior to cleaning and an unfavorable testing procedure was the reason to these very high CRs [35].

In general, an increase in corrosion rate with increasing AC current densities are supported by several studies, and visualized in Figure 2-16 [28, 30, 32, 35, 42].

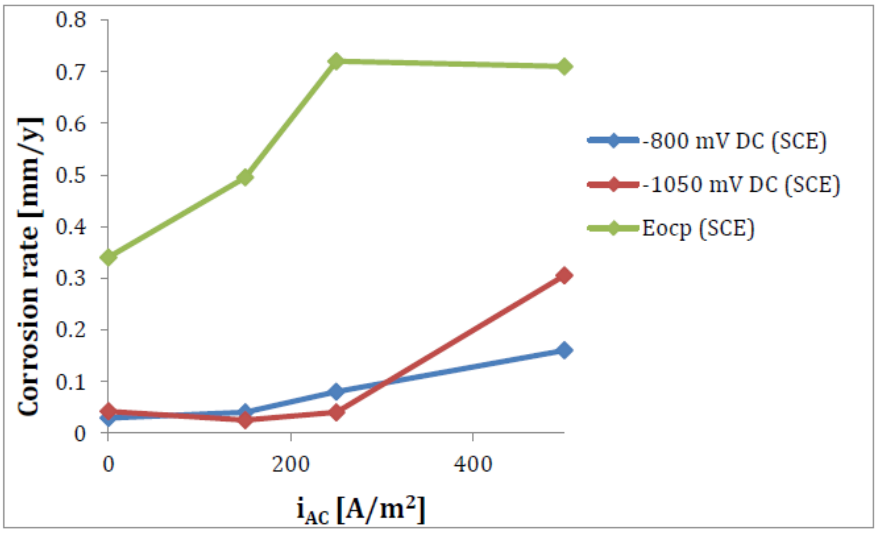

Figure 2-16: Corrosion rate as a function of applied i_{AC} under E_{OC} and different CP-potentials. Based on weight loss measurements of X65 immersed in 3.5 % NaCl-solution. Plot adapted from results by Stamnes [42].

2.4.6.2 Stainless steels

Much data exists on how carbon steel is affected by AC, but there is little on SSs. Experiments on 316 in 3.5% NaCl-solution by C. H. M. Hagen found CR in the area of 0.008-0.113 mm/year for a CP-potential of -800 mV vs SCE, and 0.007-0.024 for -1050 mV. Experiments on 25Cr SDSS were performed by first finding its passive regions through polarization curves in 3.5 % NaCl-solution. Then the steel was polarized anodically with applied AC. Testing was done with i_{AC} of 0 and 100 A/m^2, as the passive regions only was present at AC current densities below 100 A/m^2. CRs were found in the area of 0.003-0.005 mm/year for 0 AC and 0.010-0.022 mm/year for 100 A/m^2 AC [26].

C. B. Esser’s study on 316 in artificial seawater reported CR in the area of 0.0002-0.090 mm/year for a CP-potential of -800 mV vs SCE, and 0.023-0.034 for -1050 mV [27].

2.4.7 Surface characterization

Visual inspection performed by D.-K. Kim et al. found no corrosion-products at mild steel under CP in the absence of AC. For applied AC they found red rust products (two different iron products, not defined), increasingly amounts for higher AC-densities. The red rust was not formed at one place, but rather spread around on the surface. For the highest AC current densities, the red rust was covering approximately 90 % of the surface [29].

Immersion testing of X65-steel in concentrated carbonate/bicarbonate-solution performed by A.Q. Fu and Y.F. Cheng, also discovered that absence of AC lead to full protection. At low AC current densities (50 A/m^2 and below) they found that the steel corroded uniformly, but for higher AC current densities (100 A/m^2 and up) pitting occurred. Further, increased AC current density lead to more pits, and at 500 A/m^2 the steel suffered extensively from pitting [28].

In the study performed by C. H. M. Hagen, the samples were viewed post cleaning in Scanning Electron Microscope (SEM) and Energy-Dispersive X-ray Spectroscopy (EDS). It was reported that for both X65 and 316, the density and depth of pits increased with an increase in applied AC. Additionally, pits on 316 was seen to change configuration with AC; low AC current density caused etched pitting while higher current densities caused polished pits. Further, grain boundary corrosion was observed at 316 under -1050 mV vs SCE DC and 1000 A/m^2 AC, and non-soluble films formed on 316 were identified as layers of Platinum (Pt) [26].

K. Forthun performed microscopic analysis with XRD of steel samples that had been immersed in artificial seawater together with aluminum anodes. The steel samples did not suffer from corrosion, except for a few cases of non-significant corrosion at very high effective AC current density (due to area-ratio between anode and steel). The XRD-analysis was taken of the calcareous deposits that formed on the steel. From the results, it was reported that the deposits consisted mainly of $Mg(OH)_2$ and $CaCO_3$ (aragonite). The amount of the latter was seen to decrease as applied AC increased. It was also discovered minor amounts of NaCl, corrosion products (undefined) and a polymorph of $CaCO_3$ (calcite) [3].

2.4.8 Changes in pH due to AC

D.-K. Kim et al. found, by measuring bulk pH at the end of each experiment, that there was a small increase in pH during exposure time with the increase of AC current density. For a current density of 100 A/m^2 AC, the pH increased with approximately 0.8 for an exposure time of 24 hours. This means that the degree of alkalization is increased. Alkalization means that water is electrochemically reduced into OH^- (can happen with or without oxygen), and an increase of these ions close to the metal surface is believed to affect the corrosion process greatly. The elevated pH together with the AC-affected DC, may induce corrosion either by destabilization of passive layer or by moving the steel into to active corrosion-area (for very high pH), as seen in the Pourbaix-diagram in Figure 2-6 [29].

2.5 Summary

Several studies and experimental work, both in absence of and with applied AC, has been presented in the last chapters. The most important information is reviewed in the following paragraphs.

- The complete mechanism of AC corrosion has yet to be fully understood, and it is unknown which corrosion products that are formed. Studies on AC suggest that

$HFeO_2^-$ [29], Fe_3O_4 [33, 34] and Fe_2O_3 [36] may form. Studies in absence of AC also suggest the formation of Fe_3O_4 [14, 24]. Other suggestions are $FeCl_x$ and Fe(OH)Cl [14], $Fe(OH)_2$ [15] and FeOOH [24].

- It is expected that calcareous deposits will form on samples tested in artificial seawater. $Mg(OH)_2$ and $CaCO_3$ are the most probable deposits, where increased immersion time [23] and increasing AC [3] favors the latter.
- AC-cell potential is expected to be in the following order, from high to low: 25Cr>316>X65 [26]. An increase in applied AV has been seen to increase CR [31].
- The corrosion potential is seen to increase in negative direction upon applied AC [5].
- The kinetics of the anodic- and cathodic reaction has been seen to change when AC is applied [39, 40]. The cathodic reaction suffers from the most change; it has been reported that the reduction of O_2 disappears completely at high AC, leaving the formation of H_2 as the cathodic reaction [26, 43, 44].
- Recorded DC current behavior for a CP-system by different studies is contradictory. Studies agree on a cathodic and negative shift for samples polarized at -1050 mV. Several studies report a cathodic shift for -800 mV as well [26, 27, 35], while other report an anodic shift [30]. It is further expected that steel dissolution will occur despite cathodic current response of a CP-system [26].
- Corrosion is expected to occur on all steels despite CP, and an increase in applied AC has been seen to increase CR [26-28, 30, 32, 35, 42]. It has also been reported that an increase in negative direction for CP potential decreases CR for X65 [29, 30] and 316 [26, 27]. However, studies have also showed that there is no correlation between CP potential and CR for X65 [26, 35]. It is further expected that CR for samples under CP and AC will be in the following order, from high to low: X65>316>25Cr [26, 27].
- Studies comparing 3.5 % NaCl-solution and seawater are contradictory. Some studies suggest a pronounced higher CR for the NaCl-solution, tested with [29] and without [24] applied AC respectively. Other studies with applied AC have reported little difference between the two mediums [27, 35].
- Pitting is expected to occur at samples of X65 and 316, under CP and high AC current densities. An increase in current density increases pitting severity [26, 28].
- pH is expected to increase due to alkalization of the surface, for samples under CP and AC in marine environments [29].

3 Experimental

This section contains test equipment, test set up and all procedures used for this immersion corrosion testing of CS and SSs, with applied AC and under CP. All methods described are inspired by earlier projects performed by C.H.M. Hagen and C.B. Esser, and certain standards [26, 27, 45, 46]. Further, it is a continuation of the work done during the author's specialization project [35].

3.1 Test sample

3.1.1 Material specification

Three different materials have been tested in this study: X65 CS, AISI 316 SS and 25Cr SDSS. The X65-samples were manufactured from a part of a pipe at NTNU's technical laboratory of materials. Information about its chemical composition can be seen in Table 3-1.

Table 3-1: The chemical composition of the X65 carbon steel used in this thesis. Values are given in wt%.

X65 CS	**Chemical composition**								
		C	Si	Mn	P	S	V	Nb	Ti
	Wt%	0.16	0.45	1.65	0.020	0.010	0.09	0.05	0.06

The samples of 316 were manufactured from a plate delivered from NTNU's technical laboratory of materials. It was also used earlier studies by C. H. M. Hagen and C. B. Esser. Its chemical composition is shown in Table 3-2 below.

Table 3-2: The chemical composition of the AISI 316 Stainless Steel. Values are given in wt%.

AISI 316 SS	**Chemical composition**								
		C	Cr	Ni	Mo	Mn	Si	P	S
	Wt%	<0.03	16-18.5	10-14	2-3	<2	<1	0.045	<0.03

The 25Cr was delivered as a plate from "Smith Stål Nord Trondheim" and cut into samples by NTNU's technical laboratory of materials. It was also used in an earlier thesis by C. H. M. Hagen, and its chemical composition can be found in Table 3-3. The chemical composition is collected from a material certificate that accompanied the delivered plate [26].

Table 3-3: The chemical composition of the 25Cr Super Duplex Stainless Steel. Values are given in wt%.

25Cr SDSS	**Chemical composition**					
		C	Cr	Ni	Mo	Mn
	Wt%	<0.017	25.75	6.88	3.77	0.58
		Si	P	S	Cu	N
		0.29	0.021	0.0004	0.17	0.278

3.1.2 Sample preparation and geometry

The used samples were pretreated in different ways. The samples from X65 was freshly machined and either milled at NTNU’s technical laboratory of materials and then grinded manually afterwards, or just milled. Grinding was done by using successively finer grade of SiC-papers (220-500-1000 grit size) at a standard grinding table with running water. It was necessary to clean the grinded samples according to ASTM-G1 after grinding, as they started to corrode in the presence water [45]. The samples of 316 and 25Cr were old samples from C. H. M Hagen and C. B. Esser’s studies, which presumably had been polished by water to a grade finer than 1000 grit size. They had reacted during their storing at the workbench, and thus was cleaned according to ASTM-G1 as well [45]. Figure 3-1 shows two photos of samples from 25Cr; differences in surface pre- and post-cleaning and between cleaned samples.

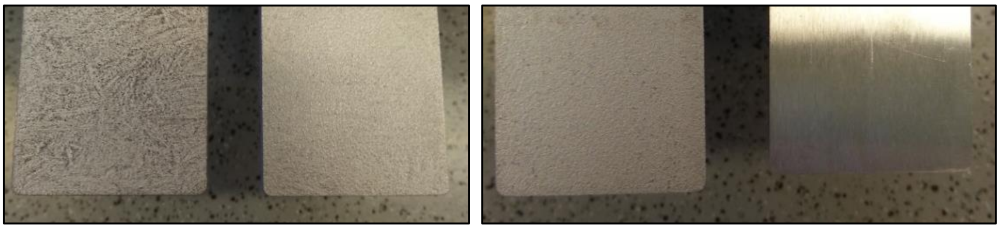

Figure 3-1: The first photo shows two 25Cr-samples, were the left on is prior to cleaning and the right one has been cleaned. The second photo shows the surface difference between some cleaned samples. The samples that was shiny, as the one to the far right was used for XRD and not weight loss measurements

Prior to testing, they were washed, dried, weighed and coated. Washing was done in the following order: distilled water, acetone and ethanol (96 %). The samples were dried using hot air from an electrical heat gun, weighed by a standard analytical weight (with an error of ± 1 mg) and coated with Miccro Super XP 2000 Stop-Off Lacquer. The weight and the lacquer can be seen in Figure 3-2. The lacquer used was chosen due to its good protection against corrosion and easy removal.

Figure 3-2: The left picture is of the standard analytical weight and the right picture is of the lacquer used to coat the samples.

The samples were delivered in sizes of approximately 80*20*2 mm (except for the 25Cr-samples, which had a thickness of 1.5 mm), but each sample was measured individually due to small dimension irregularities. The samples were coated to be able to control the applied AC current densities. The limited power output from the AC-supply made it necessary to decrease the dimensions of exposed area for high current densities. The ideally exposed area of the different samples are shown in Table 3-4 and Figure 3-3, which would give about the same “tune-in” value at the VariAC for 500 and 1000 A/m^2. However, as the coating was applied by hand with a q-tip, there were differences in actual area. This was adjusted by an increase or decrease in applied AC-voltage.

Table 3-4: The ideal dimensions of the samples.

Ideal sample dimensions				
	Exposed area [cm^2]	Height [cm]	Width [cm]	Thickness [cm]
$i_{AC} \leq 500$ A/m^2	5.68	1.2	2	0.2
$i_{AC} > 500$ A/m^2	2.6	0.5	2	0.2

All the samples were coated twice, with approximately one day between each cycle and at least one day before immersion. As many samples often were coated at the same time, the samples were stored for days in the same manner as can be seen in Figure 3-3. To avoid corrosion around the clamp on the top of the samples during experiments, coating was applied tight around the clamp and the whole top was covered with laboratory-film as seen in Figure 3-3.

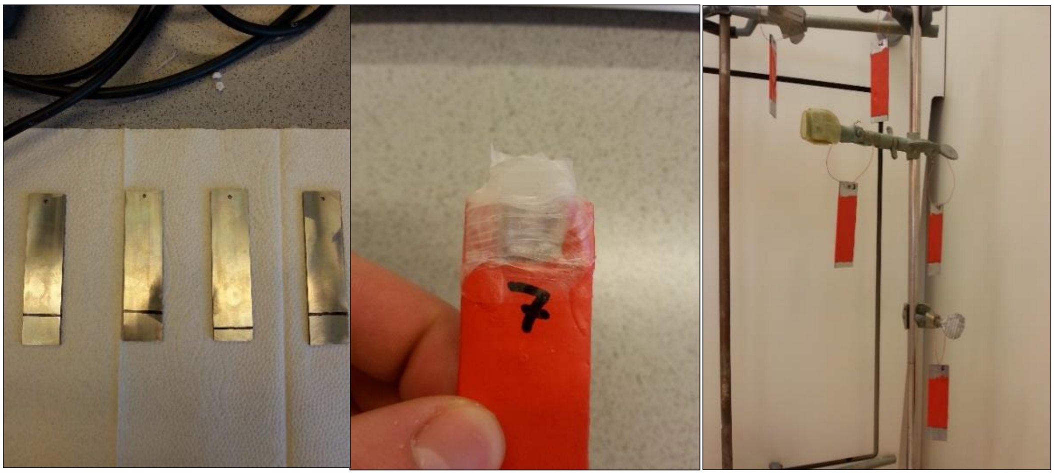

Figure 3-3: The left picture shows some samples before they were coated, and the difference in exposed area is visible. The picture in the middle shows how the sample top was covered to avoid unwanted corrosion. The right picture shows drying and storing of the samples after coating.

3.2 Experimental set up

3.2.1 Preparation of electrolytes

Two different electrolytes were used, the 3.5% NaCl-solution and artificial seawater. The artificial seawater was prepared partly in accordance with ASTM's standard [46]. One thing that was done differently from what the standards suggests is that bromides (KBr) were excluded due to HSE-reasons. Another suggestion from the standard that was not followed was that the various parts of the solutions should be made and stored in separate containers, and then be mixed immediately prior to use. Instead, based on results from the author's specialization project [35] and communication with the main supervisor [47], all the ingredients were mixed simultaneously and stored in the same container. Immediately prior to use, the pH of the solution was adjusted to 8.2 with 1.25 M NaOH, partly according to standard (standard suggests 0.1 M NaOH). pH was measured with PHM210 Standard pH Meter from Radiometer Copenhagen. The composition of the artificial sweater is found in Table 3-5.

Table 3-5: The composition of artificial seawater [46].

Compound	**Concentration [g/L]**	**Compound**	**Concentration [g/L]**
NaCl	24.53	$MgCl_2$	5.20
Na_2O_4	4.09	$CaCl_2$	1.16
KCl	0.695	$NaHCO_3$	0.201
H_3BO_4	0.027	$SrCl_2$	0.025
NaF	0.003		

3.2.2 Equipment

Lidded glass beakers were used as cells and they were immersed in a water-bath holding 25 °C, under constant stirring for equal distribution of temperature. At first, the solution within the cells was constantly stirred with an electrical driven glass rod at 100 rpm to keep the oxygen-level constant. However, since the glass rod barely was immersed in the solution and had a low rpm, it was regarded as redundant and was discarded after about half of the samples had been tested.

Platinum was used as counter electrodes and SCE in saturated KCl was used as reference electrode for all tests. The SCE displays approximately + 0.244 V vs. SHE (Standard Hydrogen Electrode) at 25 °C, which means that $E_{SHE} = E_{measured} + 0.244$ V. All DC-potentials in this project are reported versus the SCE-reference.

In order to have ionic contact between reference electrode and the submerged samples, salt bridges were made approximately every two weeks. They were made in U-shaped glass tubes constructed specially for this application by the technical laboratory at NTNU, and prepared by heating saturated KCl to 90 °C, adding agar and sucking the mixture up on one side of the glass tubes.

3.2.3 Apparatus set up

The set-up of the circuit is the same as has been used for several years of AC-studies at NTNU, and used in projects written the last couple of years [26, 27, 35]. The principle of the design is to monitor and control the DC- and AC-voltages independently of each other. The circuit is shown in Figure 3-4 and Figure 3-5.

All equipment that needed electrical supply was grounded and isolated by the use of a transformer. To keep any noise at a minimum, all the equipment was put in close proximity to each other and the wires that were used were as short as possible. Pre start-up, all clamps and wires were inspected and resistance-tested to be sure they were conductive. A VariAC supplied AC in the form of voltage, and a PC-based Gamry Potentiostat^{TM} were used to apply the DC and log data with the Gamry Framework^{TM}. The VariAC sent sinusoidal waves at a frequency of 50 Hz.

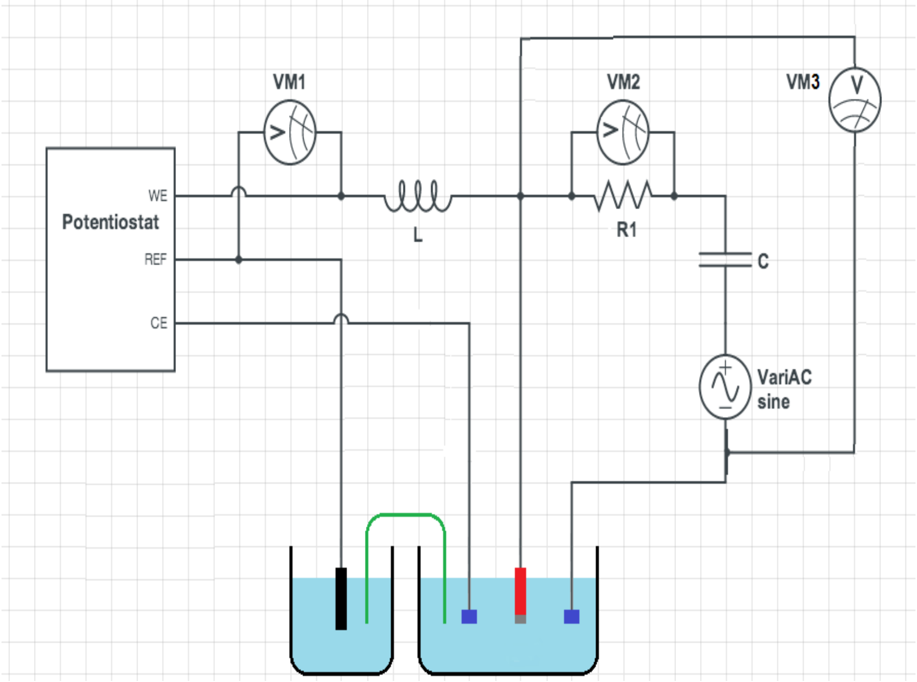

Figure 3-4: Schematic circuit diagram of the used circuit, where the AC-part is on the right and the DC-part is on the left. C is a capacitor, L is an inductor, VM is voltmeters, R is a resistance and the VariAC is the source of the AC signal. The black component is the SCE, the green tube connecting the baths is the salt bridge, the two blue elements are counter electrodes and the red component is the working electrode/steel sample. The circuit diagram is an edited version of the original made by C. B. Esser [27].

Fluke TrueRMS multimeters were used as voltmeters, where VM1 displayed the DC-potential applied by the potentiostat, making it possible to check if it was correct. VM2 displayed the AC-voltage that was manually applied by the VariAC, over a fixed resistance, R1. A Fluke 289 True RMS logging multimeter saved the values from VM3, which displayed the AC cell potential, V_{AC}. The capacitor (C) of 500 µF filtered out DC from the AC-part and the inductor (L) of 10 L filtered out AC from the DC-part. In Figure 3-5, a picture of the circuit and all its components can be seen.

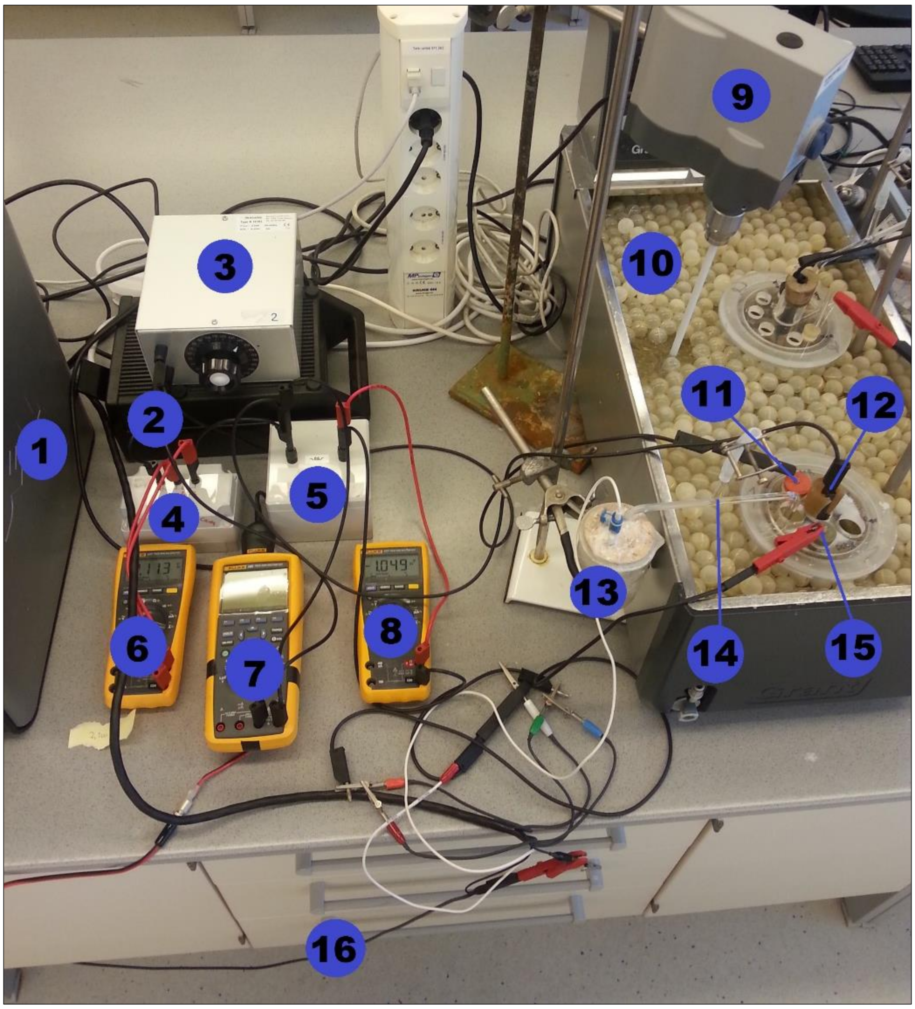

Figure 3-5: Picture of the experimental set-up. The numbered components are: 1) PC-based Gamry Potentiostat 2) transformer 3)VariAC 4) capacitor and resistance 5) inductor 6) multimeter displaying AC potential from VariAC 7) multimeter logging AC cell potential 8) multimeter displaying DC polarization from potentiostat 9) stirrer 10) temperature-controlled water bath 11) AC counter electrode 12) working electrode 13) SCE 14) salt bridge 15) DC counter electrode 16) grounding wire.

3.2.4 Experimental procedure

The test cell was filled with approximately 850 mL of electrolyte and counter electrodes and the salt bridge was installed. Then the sample was introduced, immediately before DC polarization was initiated to avoid any corrosion before recording. Lastly, the VariAC was tuned into the right voltage (if the stirring rod was used, it was introduced afterwards). Right AC-voltage was calculated with equation found in Appendix A. The VariAC needed to be fine-tuned regularly to be sure it remained at the correct value due to its oscillating nature. After 48 hours, the AC was turned off right after polarization ended. Then the sample was taken out, rinsed in distilled water and ethanol and dried with heat gun. Lastly, the coating was peeled of manually and the samples were cleaned for corrosion products (except for one sample that was stored in a desiccator for approximately 3 months).

For the majority of the experiments, the pH was measured. This was done either with regular pH-strips or by a standard pH-meter. For the strips, the pH was measured in the solution right before the end or at the corroded sample right after it had been removed from the solution. For the pH-meter, the pH was measured in the solution after the sample had been removed.

3.2.5 Experimental method

Due to time constraints and unforeseen events, limited parallel- and re-testing was performed. A total of 28 samples were tested: 15 of X65, 5 of 316 and 8 of 25Cr. The common testing-method for all samples was to polarize them potentiostatically at -800 or -1050 mV vs SCE, and then applying a constant AC current density through the whole experiment of 48 hours. The parameters that were measured were the DC current response of the potentiostat and the AC cell potential (data from three experiments were lost due to technical failures). The following polarizing-tests were performed:

- One sample of X65 was tested in 3.5 % NaCl-solution under -800 mV DC and with applied AC of 500 A/m^2. The sample was stored for 3 months in a desiccator. The purpose was to examine if corrosion continued upon storage, which was assumed to be the cause for the high CR in the author's specialization project [35].
- Four samples of X65 were tested with applied DC and no AC, to examine if the samples were fully protected by the DC. Experiments were performed in 3.5 % NaCl-solution and artificial seawater, at -800 and -1050 mV DC.
- Eight samples (four in 3.5 % NaCl-solution and four in artificial seawater) of X65 were tested to determine the effect of surface roughness. Testing was done at 500 A/m^2 AC with two different topographies, in -800 and -1050 mV DC. These performed experiments in NaCl-solution also served as reproducibility-data when compared to a former thesis by C. H. M. Hagen [26].
- Four samples of 316 were tested in artificial seawater at 500 and 1000 A/m^2 AC, in -800 and -1050 mV DC.
- Six samples of 25 Cr were tested in artificial seawater at 100, 500 and 1000 A/m^2 AC, in -800 and -1050 mV DC.
- Powder from three experiments was inspected through XRD analysis. The different powders originated from calcareous deposits on 316 and 25Cr tested in artificial seawater at -800 mV DC and 1000 A/m^2 AC, and cell sediments from experiment performed at X65 in artificial seawater at -800 mV DC and 500 A/m^2 AC.
- Three experiments were performed in order to examine the samples in Grazing Incidence X-ray Diffraction (GIXRD) analysis. This was performed at: X65 tested in 3.5 % NaCl-solution at -800 mV DC and 700 A/m^2 AC, X65 tested in artificial seawater at -800 mV DC and 500 A/m^2 AC, 25Cr tested in artificial seawater at -800 mV DC and 1000 A/m^2 AC.

- 15 samples were examined and photographed in SEM: seven samples of X65 that was tested in different solutions, different surface roughness and various DC-potentials. Two from 316 that was tested at 500 A/m^2 AC and six samples from 25Cr.
- One sample was examined in EDS: 25 Cr tested in artificial seawater at -800 mV DC and 500 A/m^2 AC. It was examined after cleaning.

3.3 Weight loss measurements

After electrochemical testing, the samples were cleaned and analyzed in accordance with ASTM G1 [45]. The chosen cleaning method was chemical removal, where different solutions and procedures were used for different types of steels, which are summarized in Table 3-6. During cleaning, the whole sample was immersed in the solution.

Table 3-6: The various solutions and procedures for chemical cleaning of the tested samples.

Steel	Solution	Cycle time	Temperature
X65	- 500 mL HCl (SG 1.16) - 3.5 g hexamethylene tetramine - Reagent water to make 1000 mL	30 sec	20 - 25 °C
AISI 316 SS **25Cr SDSS**	- 100 mL HNO_3 (SG 1.40) - Reagent water to make 1000 mL	20 min	60 °C

Non-corroded samples were tested in order to determine if the cleaning solutions caused any metal loss. As X65 suffered small amounts of loss while the SSs suffered none, the detailed cleaning procedure differed slightly between the types of steel.

X65 was usually cleaned in six cycles, where the samples were rinsed as normal (with distilled water, acetone, ethanol and then dried with a heat gun) between each cycle. The weight loss measurements from each cycle was corrected for metal loss and used to construct a plot where the weight loss from corrosion products was found. An example of such a plot and some explanation can be found in Appendix B. As the SSs were immune to the cleaning solution, no correction or plot was necessary, and only one cleaning cycle was performed.

The weight loss measurements were used to calculate corrosion rate (CR) with the equation found in Appendix A.

3.4 Surface characterization

On a macroscopic level, the samples were inspected visually both after electrochemical testing and after cleaning. Photographs were also taken pre and post cleaning.

On a microscopic level, the samples were tested in SEM, EDS, XRD and GIXRD. All the samples viewed in SEM and EDS were viewed post cleaning. The SEM that was used was a LV FE-SEM Zeiss Supra 55 VP. A secondary electron detector was used to achieve topographical contrast, and the chosen parameters were an accelerating voltage of 15 kV and a working distance of approximately 10 mm. For regular SEM, low current-mode and an aperture size of 30 µm was used. For EDS, high current mode was used and the aperture size was set to 120 µm.

Three tests were performed with XRD and three with GIXRD, where a Bruker AXS D8 DaVinci Advance machine was used to perform the testing and Bruker AXC Diffrac.EVA software was used to evaluate the results. For XRD, the deposits and products on the samples were scratched off, crushed in a mortar and distributed on sample holders with single-crystalline silicon as background. These tests were set for 30 minutes each, with a fixed divergence slit of 0.2° and a 2θ-range of 10-75°. In GIXRD, the sample surface was characterized, and thus any calcareous deposits were removed before the samples were cut in applicable size by NTNU’s technical laboratory of materials. One sample was cut without any cooling medium and the two others were cut with water-cooling and rinsed in ethanol afterwards. These tests were set for 2 hours each with a fixed divergence slit, 2.5° incidence slit and a 2θ-range of 15-70°.

4 Results

This chapter will present the results from the 28 tested samples: 15 of X65, 5 of 316 and 8 of 25Cr. All samples were tested for 48 hours. The results from X65 in 3.5 % NaCl-solution that was used to test reproducibility of data compared to C. H. M. Hagen's thesis, will be presented in Appendix C. Any results due to parallel testing or from some other reason are unnecessary to include in this chapter, will be presented in Appendix D-F.

The results will be presented in the following order: polarization behavior, weight loss, surface characterization (first macroscopic, then microscopic) and general observations. Lastly, all the results will be summarized in a separate subsection. All recorded potentials are measured against the SCE, which shows + 0.244 V against the SHE at room temperature. The AC-potentials are consistently reported as root mean square (RMS) values as measured by multimeters, and the DCs in polarization-figures are reported at cathodic for negative values and anodic for positive values. Further, 3.5 % NaCl-solution will be referred to as NaCl and artificial seawater will be referred to as seawater in this chapter.

4.1 Polarization behavior

During experimental testing, the applied DC current density to maintain the DC-potential at a constant level was measured. In addition, the AC cell potential was logged throughout each experiment.

4.1.1 Polarization behavior in absence of AC

The DC current response for potentiostatic polarization of X65-samples in absence of AC can be seen in Figure 4-1. Samples have been immersed in both NaCl and seawater, and polarized at -800 and -1050 mV DC.

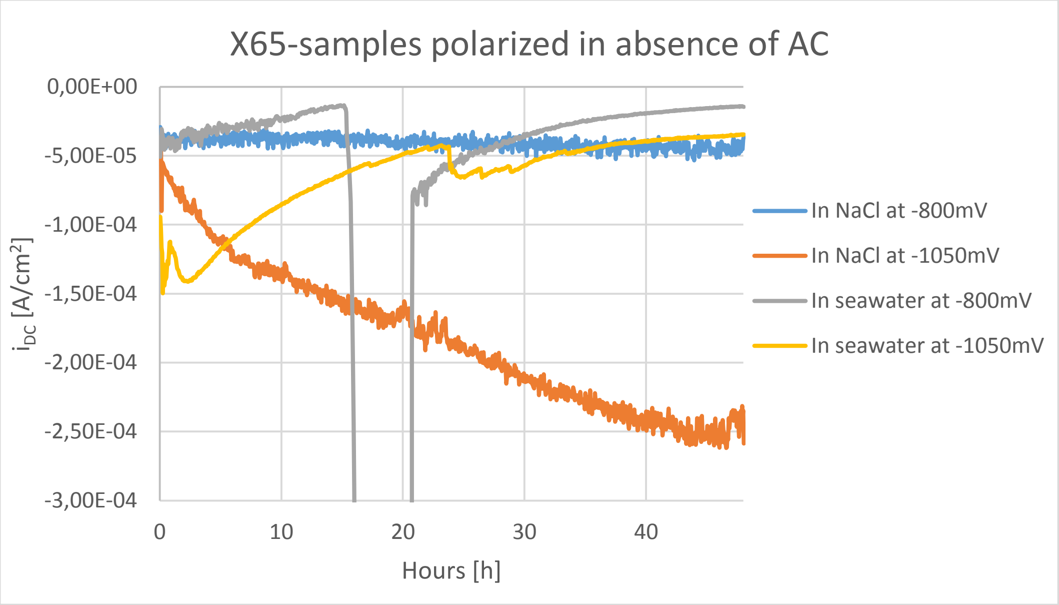

Figure 4-1: The recorded DC current density response as a function of time, with no AC applied. Samples are polarized at -800 and -1050 mV DC, in 3.5 % NaCl-solution and artificial seawater.

One can see here that the DC current response is at a stable cathodic current for samples polarized at -800 mV DC in NaCl. At -1050 mV DC in the same medium, the current increases in cathodic direction through the whole experiment. For the sample in seawater at -800 mV DC, a big drop in the current response can be seen. This is due to a situation where the salt bridge lost contact and can therefore be ignored. Then, it is visible that the DC current response shows decreasingly cathodic values for both potentials in seawater.

4.1.2 Polarization behavior of various surface roughness

The DC current response for potentiostatic polarization of X65-samples in order to determine the effect of surface roughness, can be seen in from Figure 4-2 to 4-5. Samples polarized in NaCl can be seen in Figure 4-2 and 4-3, which have been polarized at -800 and -1050 mV DC, respectively. Figure 4-4 and 4-5 shows the samples that were immersed in artificial seawater, polarized at -800 and -1050 mV DC.

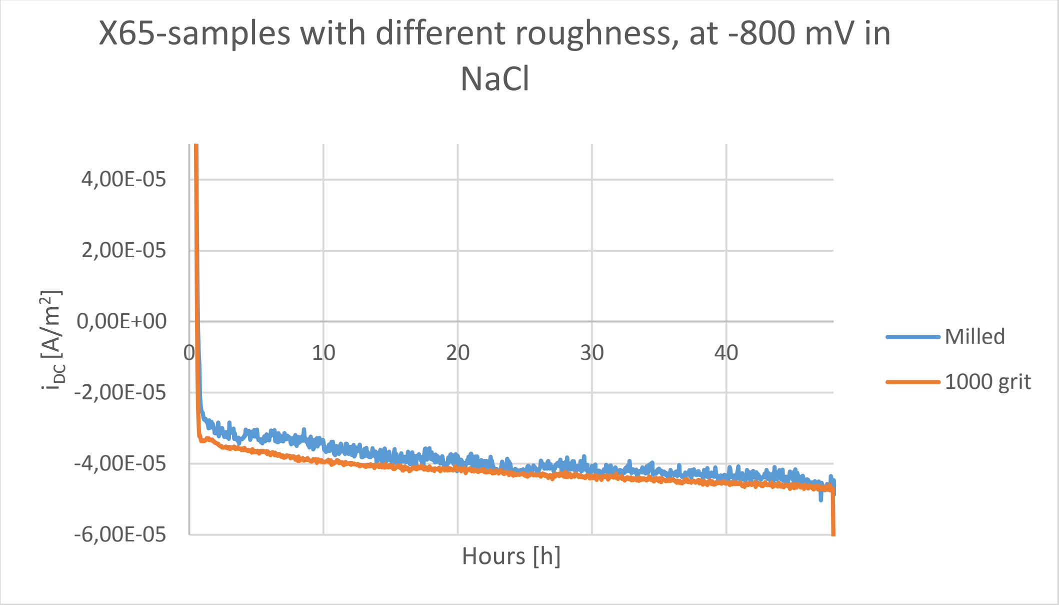

Figure 4-2: The recorded DC current density response as a function of time, with 500 A/m^2 AC applied. Samples are either milled or grinded at 1000 grit, and polarized at -800 mV DC in 3.5 % NaCl-solution.

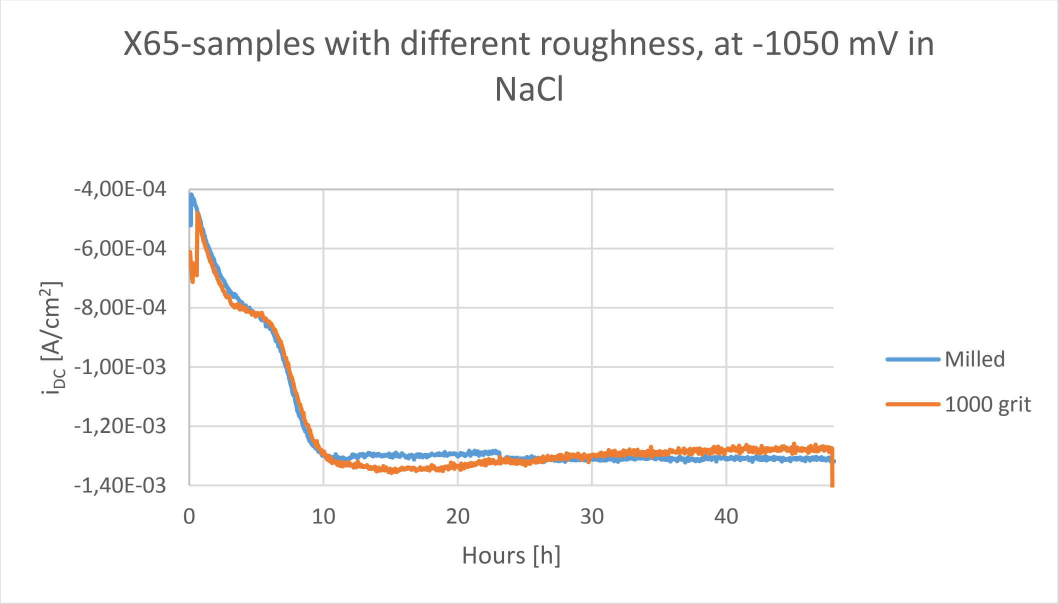

Figure 4-3: The recorded DC current density response as a function of time, with 500 A/m^2 AC applied. Samples are either milled or grinded at 1000 grit, and polarized at -1050 mV DC in 3.5 % NaCl-solution.

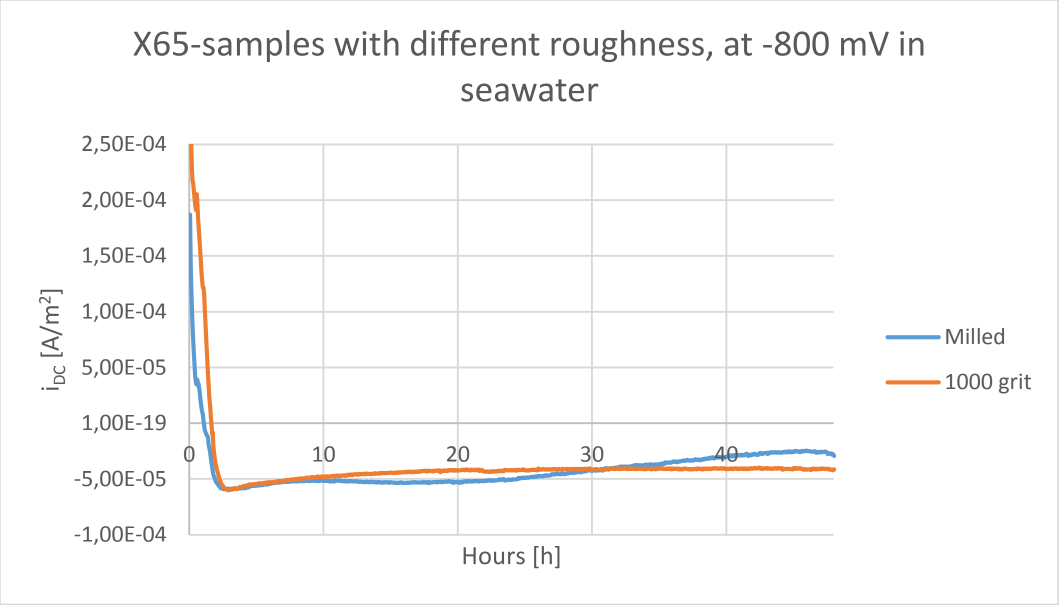

Figure 4-4: The recorded DC current density response as a function of time, with 500 A/m^2 AC applied. Samples are either milled or grinded at 1000 grit, and polarized at -800 mV DC in artificial seawater.

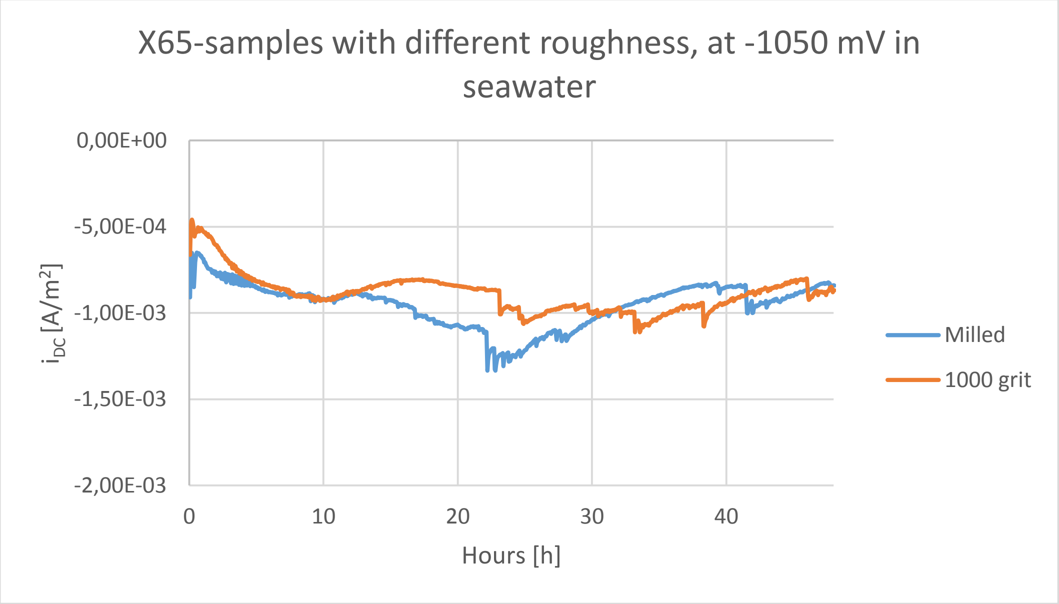

Figure 4-5: The recorded DC current density response as a function of time, with 500 A/m^2 AC applied. Samples are either milled or grinded at 1000 grit, and polarized at -1050 mV DC in artificial seawater.

From Figure 4-2 to 4-5, one can see that the DC current response more or less stabilizes at cathodic currents for all experiments, with an increase in cathodic direction for -1050 mV compared to -800 mV DC. More important, it is visible that the difference between milled samples and samples that are grinded to 1000 grit is very small. The differences seen for seawater at -1050 mV in Figure 4-5, are so small they can be neglected.

Figure 4-6 and 4-7 displays the AC cell potential that was recorded from the experiments viewed in Figure 4-2 to 4-5 above.

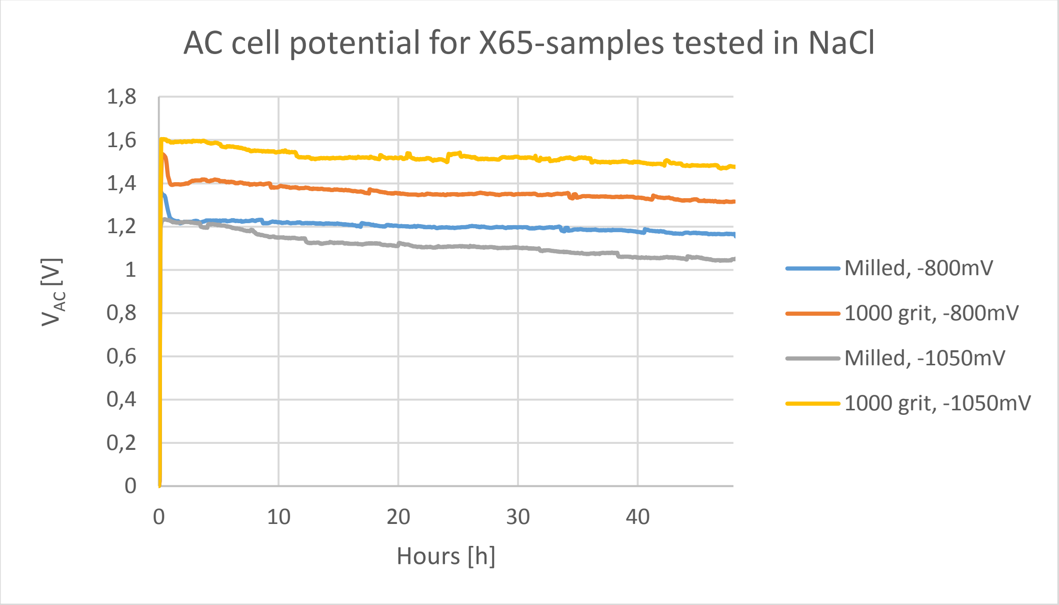

Figure 4-6: The recorded AC cell potential as a function of time, with 500 A/m² AC applied. Samples are either milled or grinded at 1000 grit, and polarized at -800 or -1050 mV DC in 3.5 % NaCl-solution.

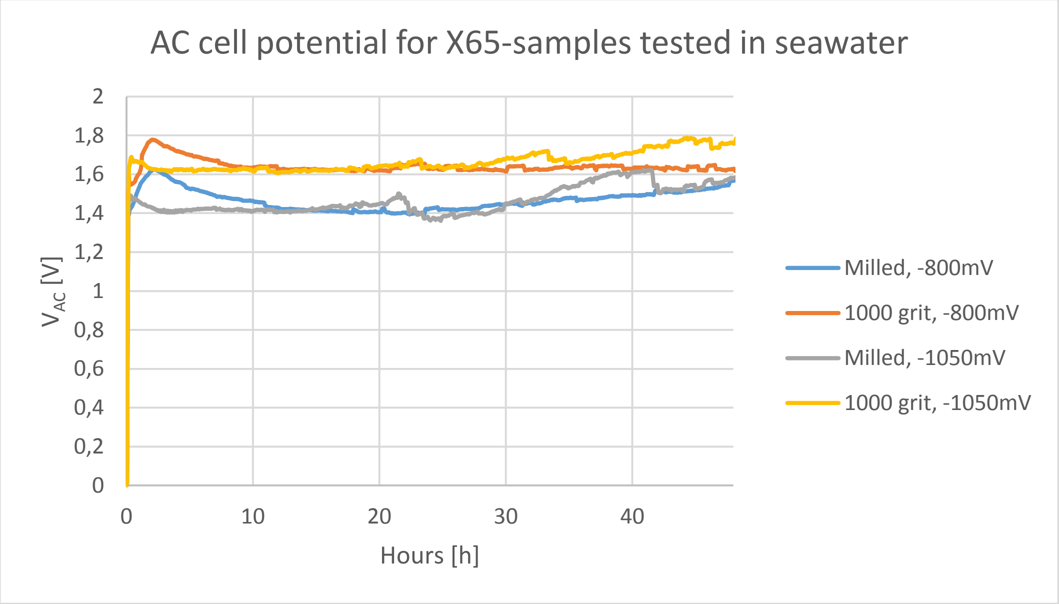

Figure 4-7: The recorded AC cell potential as a function of time, with 500 A/m² AC applied. Samples are either milled or grinded at 1000 grit, and polarized at -800 or -1050 mV DC in artificial seawater.

From both figures above, it is clear that the V_{AC} for both DC-potentials are higher for the samples grinded to 1000 grit compared to those that are milled. This is the case in both NaCl and seawater. Samples tested in NaCl as seen in Figure 4-6 are inconsistent when it comes to the effect of applied DC-potential, while for samples tested in seawater as in Figure 4-7, there seems to be little difference in V_{AC} with the different DC-potentials.

4.1.3 Polarization behavior of AISI 316 SS

The DC current response for potentiostatic polarization of 316-samples in seawater can be seen in Figure 4-8. Samples have been polarized at -800 and -1050 mV DC, and been under 500 and 1000 A/m^2 applied AC.

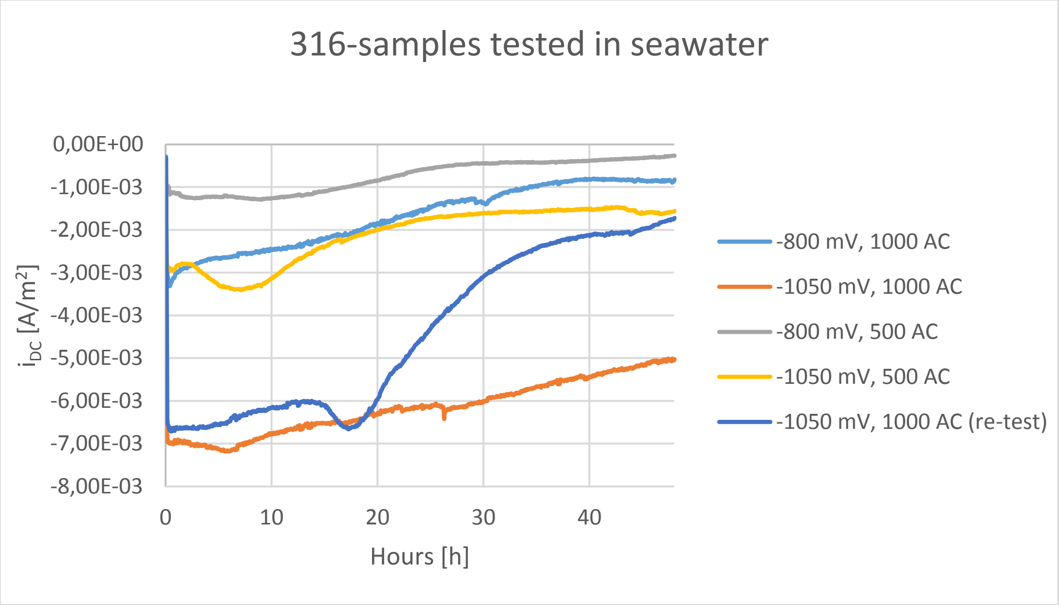

Figure 4-8: The recorded DC current density response as a function of time, with different AC applied at 316-samples. The samples are milled and polarized at different potentials in artificial seawater.

It can be seen from the figure that cathodic currents occur for all samples, and that the cathodic current decrease with time. Further, the graphs are similar for three of 5 experiments, where the last one tested at -1050 mV DC and 1000 A/m^2 AC is significantly more cathodic. Further, the sample re-tested at the same parameters suffers a major decrease in cathodic direction after approximately 20 hours. However, the general trend is that increasingly negative DC-potentials and increasing applied AC, increases the current response in cathodic direction. Compared to similar experiments on X65 in Figure 4-4 and 4-5, the current response is higher in cathodic direction for 316.

Figure 4-9 displays the AC cell potential that corresponds to the experiments viewed in Figure 4-8.

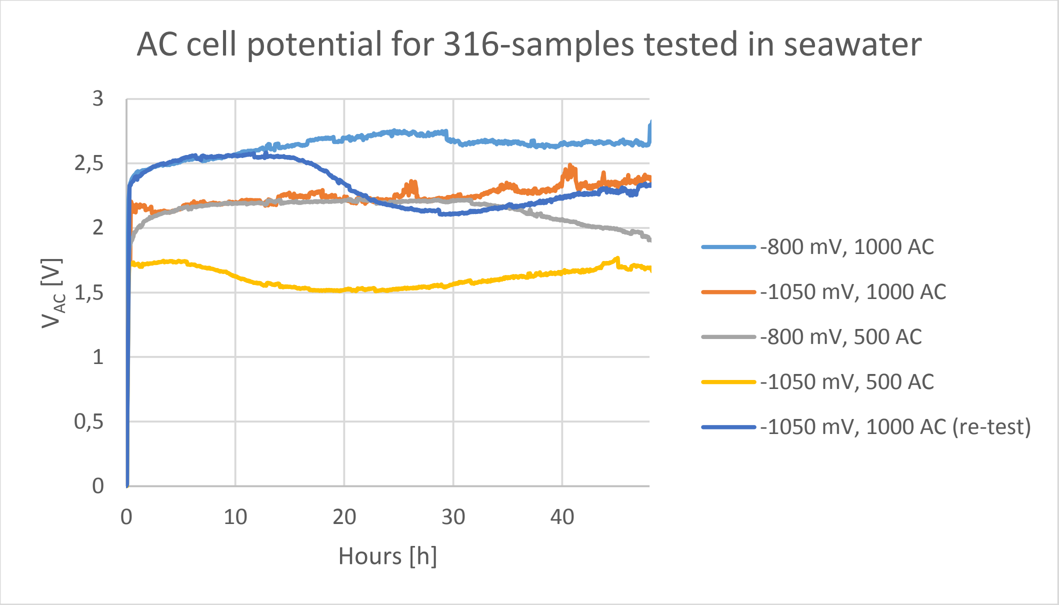

Figure 4-9: The recorded AC cell potential as a function of time, with various AC applied at 316-samples. The samples are milled and polarized at different potentials in artificial seawater.

From the figure, it can be seen that high applied AC and less negative applied DC causes V_{AC} to increase. Thus, the highest value of V_{AC} is at -800 mV DC and 1000 A/m^2 AC, and the lowest is at -1050 mV and 500 A/m^2. These values are inconsistent with the corresponding current response. However, the form of the curves is similar for all cases except for the re-tested sample. The V_{AC} for the re-tested sample is high in the first part of the experiment, but suffers from a significant decrease after about 20 hours, similar to what can be seen for the DC current response of the re-tested sample in Figure 4-8.

If the V_{AC}-results from Figure 4-9 are compared to similar results for X65 in Figure 4-7, the latter values are a bit lower.

4.1.4 Polarization behavior of 25Cr SDSS

The DC current response for potentiostatic polarization of 25Cr-samples in seawater can be seen in Figure 4-10. Samples have been polarized at -800 and -1050 mV DC, and have been under 100, 500 and 1000 A/m^2 applied AC. The line in light blue tested at -800 mV DC and 1000 A/m^2 AC were tested twice. As the current response curves were similar, they are presented together in Appendix D.

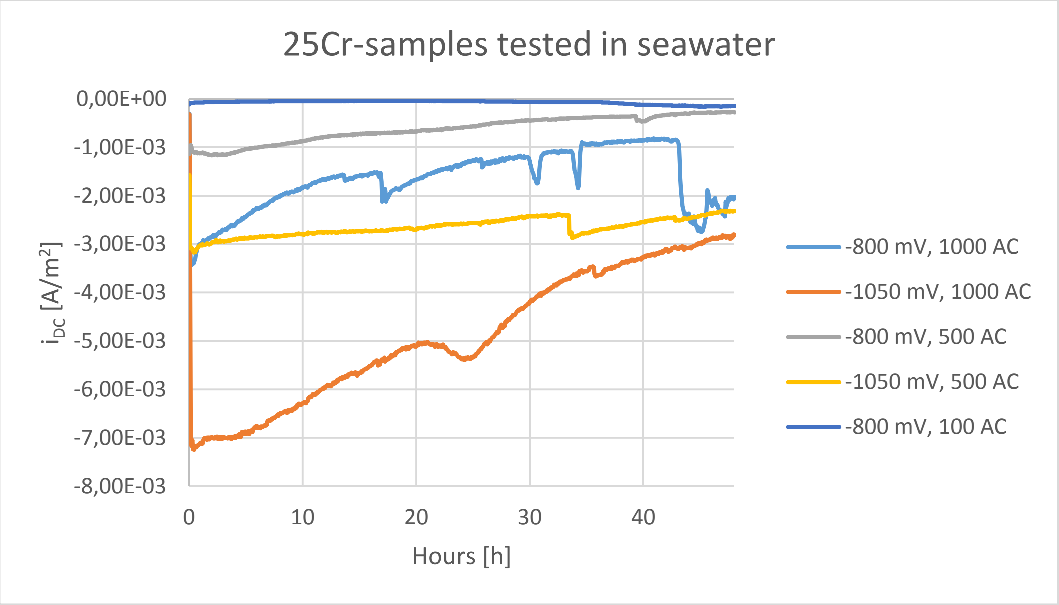

Figure 4-10: The recorded DC current density response as a function of time, with different AC applied at 25Cr-samples. The samples are milled and polarized at different potentials in artificial seawater.

It can be seen from all samples that the current response is cathodic and that the cathodic current decreases with time. Further, both increasingly negative DC and an increase in AC cause the current response to increase in cathodic direction. In addition, the cathodic currents are higher for all experiments on -1050 mV DC, compared to -800 mV DC. At 1000 A/m^2 AC, the current response is very unstable with several “drops” with increase in cathodic current that re-stabilizes quickly. This is especially present for -800 mV DC. If the results on 25Cr in Figure 4-10 are to be compared with the results on 316 as seen in Figure 4-8, the magnitude of the values are similar.

Figure 4-11 displays the AC cell potential that corresponds to the experiments viewed in Figure 4-10. The experiment that was tested twice (at -800 mV DC and 1000 A/m^2 AC) will be presented in Appendix D with the current response.

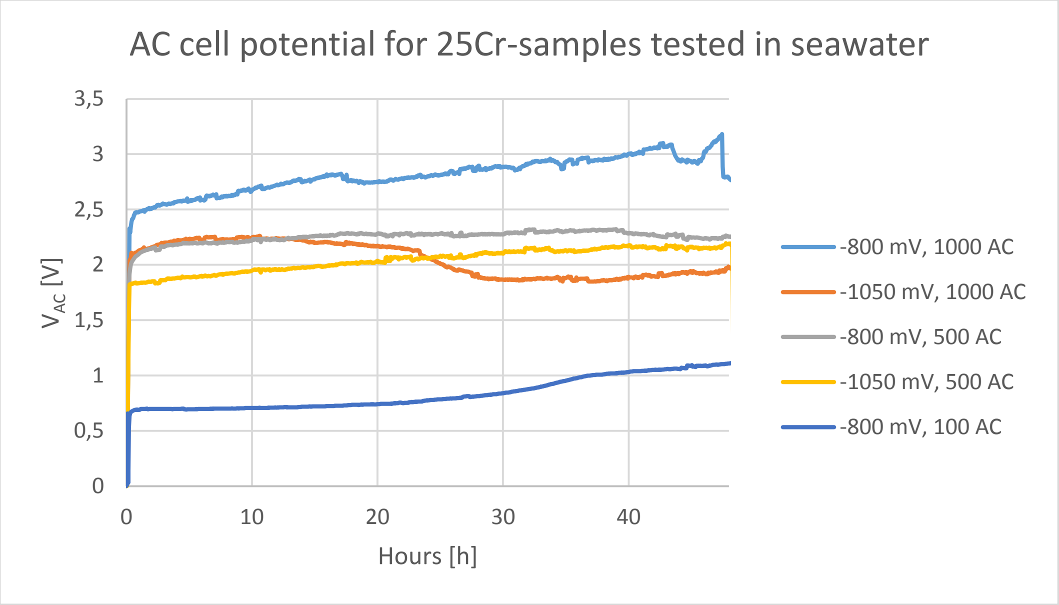

Figure 4-11: The recorded AC cell potential as a function of time, with various AC applied at 25Cr-samples. The samples are milled and polarized at different potentials in artificial seawater.

From Figure 4-11, it can be seen that the V_{AC} is high when applied AC is high and DC is less negative, which is in correlation with measurements on 316 as seen in Figure 4-9. Particularly low values are seen when 100 A/m^2 AC is applied. It does not seem like there is a correlation between the DC current response and the V_{AC} for 25Cr. If the magnitude of the 25Cr-values is compared with those at 316 in Figure 4-9, some values are equal and some are a bit higher for 25Cr.

4.2 Weight loss measurements

Corrected weight loss for each sample was measured after the experiment, and this together with the duration of immersion and the exposed area was used to calculate the CR. The equation used for this calculation can be found in Appendix A. Weight loss in mg is presented with decimals for X65 but not for 316 and 25Cr. This is due to the grade of detail of the weight used, and because the weight loss for X65 is based on plotted graphs as can be seen in Appendix B.

4.2.1 Weight loss measurements in absence of AC

For three out of four X65-samples tested in absence of AC, no significant corrosion was found through weigh loss measurements. There was however found a CR of 0.041 mm/year for the sample tested in seawater at -800 mV DC, which corresponds to the grey graph in Figure 4-1.

4.2.2 Weight loss measurements of various surface roughness

Corrosion rates based on calculations from the measured weight loss for X65-samples, either milled or grinded to 1000 grit and tested in different solutions can be seen in Table 4-1.

Table 4-1: Calculated corrosion rate for X65-samples tested at 500 A/m^{2}AC under -800 and -1050 mV DC, in 3.5 % NaCl-solution and artificial seawater. The samples have been either milled or grinded to 1000 grit.

	NaCl		**Seawater**	
Surface roughness	**-800 mV DC**	**-1050 mV DC**	**-800 mV DC**	**-1050 mV DC**
Milled [mm/year]	0,288	0,226	0,208	0,191
1000 grit [mm/year]	0,297	0,227	0,239	0,209

It can be seen here that the CRs are similar for the two topographies, where the difference is highest at 0.021 mm/year for the samples tested at -800 mV DC in seawater. Further, an increase in negative direction for applied DC seems to decrease CR in NaCl. It is not clear if this is a trend in seawater as well, as these calculated values seem to vary more. A clear trend however, is that CRs are higher for samples tested in NaCl compared to seawater, especially at an applied DC of -800 mV.

4.2.3 Weight loss measurements of AISI 316 SS

Corrosion rates based on calculations from the measured weight loss for 316-samples that were tested in seawater can be seen in Table 4-2.

Table 4-2: Calculated corrosion rate for 316-samples tested at different ACs under -800 and -1050 mV DC, in artificial seawater. One sample was re-tested.

DC [mV]	**AC [A/m^2]**	**Weight loss [mg]**	**Area [cm^2]**	**CR [mm/year]**
-800	1000	1	2.88	0.081
-1050	1000	3	2,68	0.260
-1050	1000	0	2,55	0 (re-test)
-800	500	1	5,55	0.042
-1050	500	0	5,55	0

From Table 4-2, one can see that 316 seem to be protected at -1050 mV DC at medium applied AC. For a high AC of 1000 A/m^2 however, the results differ greatly in the two experiments. At -800 mV DC, some corrosion occurs, where the CR seem to double when the applied AC is doubled.

4.2.4 Weight loss measurements of 25Cr SDSS

Corrosion rates based on calculations from the measured weight loss for 25Cr-samples that was tested in seawater can be seen in Table 4-3. The experiment that was performed twice (at -800 mV DC and 1000 A/m^2 AC), showed similar CRs for both tests and are thus presented in Appendix D.

Table 4-3 Calculated corrosion rate for 25Cr-samples tested at different ACs under -800 and -1050 mV DC in artificial seawater.

DC [mV]	AC [A/m^2]	Weight loss [mg]	Area [cm^2]	CR [mm/year]
-800	1000	6	2.67	0.522
-1050	1000	3	2.54	0.274
-800	500	3	5.51	0.126
-1050	500	5	5.19	0.224
-800	100	1	5.33	0.044
-1050	100	0	5.33	0

From the table it can be seen that no or little corrosion occurs at low AC current density. For medium and high applied AC there is no clear trend: at -1050 mV DC the CR is similar for both 500 and 1000 A/m^2 AC, while for -800 mV DC the CR are both lower (500 A/m^2 AC) and a lot higher (1000 A/m^2) than at -1050 mV DC.

4.2.5 Weight loss measurements of the stored sample

Corrosion rate based on calculation from the measured weight loss for a X65-sample tested and then stored for three months before cleaning, are visible in Table 4-4. One can see that the CR is at 0.215 mm/year, which is reasonably low.

Table 4-4: Calculated corrosion rate for a milled X65-sample tested at 500 A/m^{2}AC and -800 mV DC Testing was done in 3.5 % NaCl-solution and the sample was stored three months in a desiccator between testing and cleaning.

DC [mV]	AC [A/m^2]	Weight loss [mg]	Area [cm^2]	CR [mm/year]
-800	500	5.25	5.67	0.215

4.3 Macroscopic surface characterization

Each sample was inspected visually both after experiments was finished and after samples were cleaned. The samples were photographed during inspection.

4.3.1 Surface characterization in absence of AC

Photographs taken of samples tested in absence of AC can be seen in Figure 4-12. Only one of the post cleaned samples are presented due to high degree of similarity between the experiments.

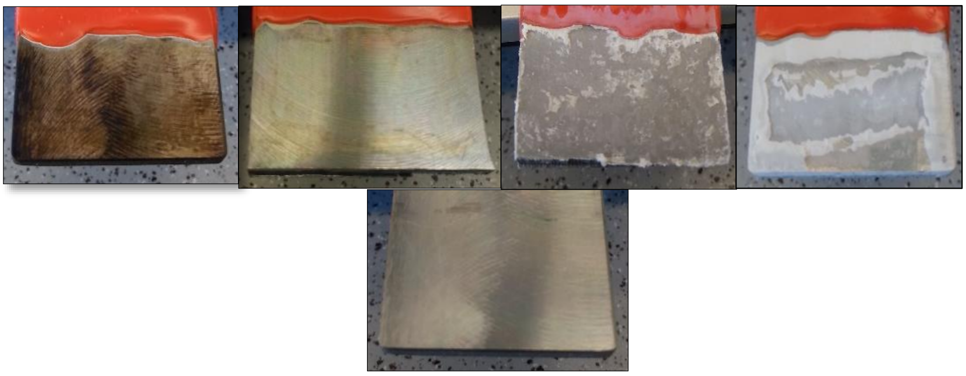

Figure 4-12: Pictures of the samples tested with applied DC and absence of AC. The top pictures are prior to cleaning and the bottom one is post cleaning. Of the top pictures: the two to the left are tested in 3.5 % NaCl-solution and the right ones in artificial seawater. From left to right they have been tested at -800, -1050, -800 and -1050 mV DC. The bottom picture corresponds to the first at the top.

From the figure, it appears that some black corrosion products formed on the sample under -800 mV DC in NaCl, while the one at -1050 mV DC was fully protected. In seawater, a thin layer of calcareous deposits was formed, with an increased amount corresponding to an increase in negative direction of applied DC.

4.3.2 Surface characterization of various surface roughness

Photographs taken of samples with different surface roughness tested in NaCl and seawater can be seen in Figure 4-13 and 4-14 respectively.

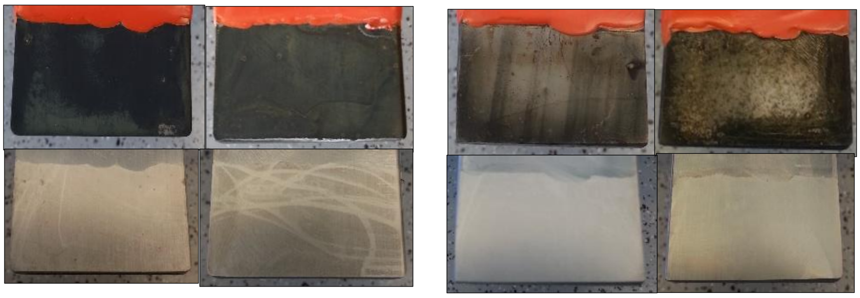

Figure 4-13: Pictures of samples with different surface roughness tested in 3.5 % NaCl-solution at 500 A/m² AC. The top pictures are prior to cleaning and the bottom one is post cleaning. The left cluster was tested at -800 mV DC, and the other at -1050 mV DC. Within each cluster, the 1000 grit samples are to the left.

One can see that there is little, if any, difference between milled and 1000 grit samples. Further, the corrosion product is black with a decrease in amount for -1050 mV DC.

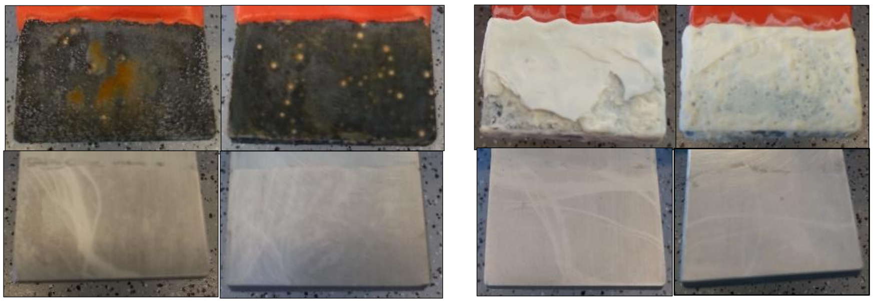

Figure 4-14: Pictures of samples with different surface roughness tested in artificial seawater at 500 A/m² AC. The top pictures are prior to cleaning and the bottom one is post cleaning. The left cluster was tested at -800 mV DC, and the other at -1050 mV DC. Within each cluster, the 1000 grit samples are to the left.

It can be seen that there seem to be a mix between orange and black corrosion products for the samples tested at -800 mV DC, while for -1050 mV a medium thick layer of calcareous deposits were formed. There is little difference between milled and 1000 grit, but some difference can be seen at -800 mV DC.

4.3.3 Surface characterization of AISI 316 SS

Photographs taken of 316-samples tested in seawater can be seen in Figure 4-15 and 4-16, which have been tested at 500 and 1000 A/m^2 AC respectively.

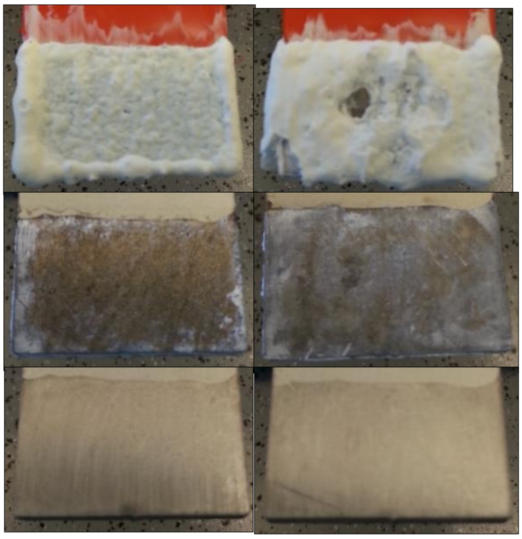

Figure 4-15: Pictures of 316-samples tested in artificial seawater at 500 A/m^2 AC. The top pictures are right after testing, the middle ones are after deposits have been stripped off prior to cleaning and the bottom one is post cleaning. The left row was tested at -800 mV DC, and the right at -1050 mV DC.

From Figure 4-15, it can be seen that calcareous deposits are formed at both potentials, but with increased amount at -1050 mV DC. At -800 mV, thicker deposits seem to form on the edges. It can also be seen that corrosion has occurred beneath the deposits.

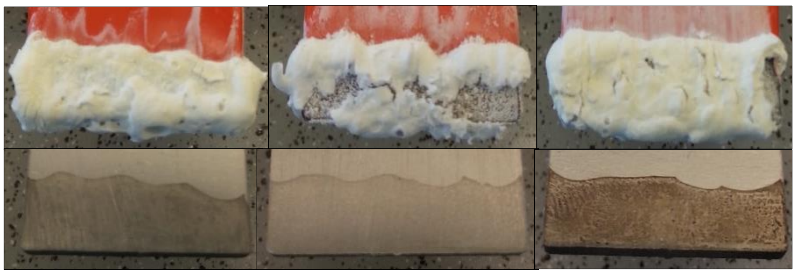

Figure 4-16: Pictures of 316-samples tested in artificial seawater at 1000 A/m^2 AC. The top pictures are prior to cleaning and the bottom ones are post cleaning. The left row was tested at -800 mV DC, the middle at -1050 mV DC and the right is the re-test of the middle one.

In Figure 4-16, it can be seen that all the samples suffered from thick calcareous deposits. It is also possible to see that the tested area has dark insoluble layer after cleaning. This is especially visible for the re-tested experiment at -1050 mV DC and 1000 A/m^2 AC.

4.3.4 Surface characterization of 25Cr SDSS

Photographs taken of 25Cr-samples tested in seawater can be seen in Figure 4-17 where the samples were tested at 100 and 500 A/m^2 AC, and in Figure 4-18 where the samples were tested at 1000 A/m^2 AC.

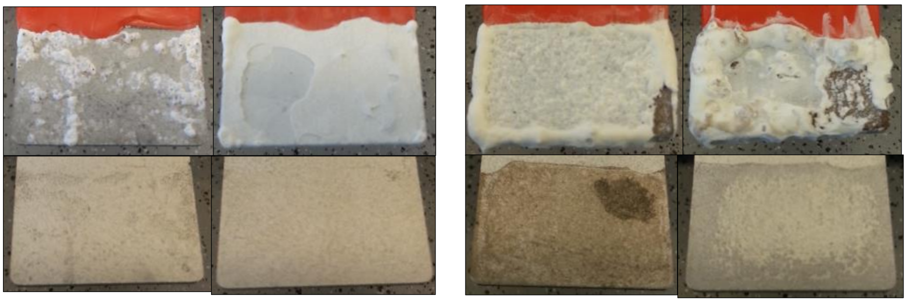

Figure 4-17: Pictures of 25Cr-samples tested in artificial seawater. The top pictures are prior to cleaning and the bottom one is post cleaning. The left cluster was tested at 100 A/m^2 AC, and the right cluster at 500 A/m^2 AC. Within each cluster, the left samples are at -800 mV DC and the right at -1050 mV DC.

From Figure 4-17, the following trend can be seen: more calcareous deposits form with higher AC current densities and increase in negative direction for applied DC. The sample tested at -800 mV DC and 100 A/m^2 AC only have deposits at certain places, and it looks like the deposits at 500 A/m^2 AC have a darker color, with some black spots. From the cleaned samples, it is clearly visible that corrosion has occurred. Further, the cleaned sample tested at -800 mV DC and 500 A/m^2 AC have a very dark area at its top right corner.

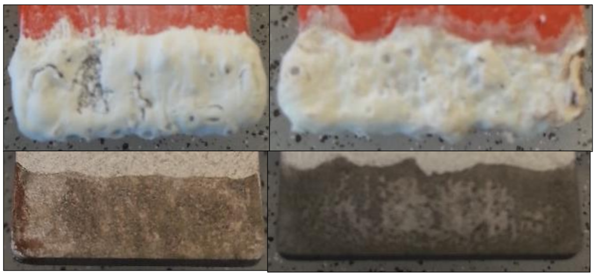

Figure 4-18: Pictures of 25Cr-samples tested in artificial seawater at 1000 A/m^2 AC. The top pictures are prior to cleaning and the bottom one is post cleaning. The pictures to the left are samples tested at -800 mV DC and the right at -1050 mV DC.

It can be seen that the trend from Figure 4-17 continues. Furthermore, both samples have dark areas after cleaning, but the tested area from the experiment at -1050 mV DC are significantly darker.

4.3.5 Surface characterization of samples for GIXRD analysis

Photographs of the samples that were re-tested in order to be examined in GIXRD can be seen in Figure 4-19 to 4-21. The samples in Figure 4-19 and 4-20 are of X65, which were tested in NaCl and seawater respectively. The sample in Figure 4-21 is of 25Cr.

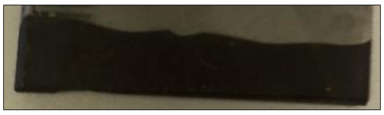

Figure 4-19: Picture of an X65-sample before GIXRD analysis. It was tested in 3.5 % NaCl-solution at -800 mV DC and 700 A/m^2 AC. The sample was cut without any cooling medium.

In Figure 4-19, one can see that the sample has corroded and that the corrosion product is black.

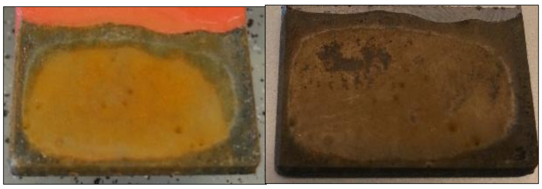

Figure 4-20: Picture of an X65-sample before GIXRD analysis. It was tested in artificial seawater at -800 mV DC and 500 A/m^2 AC. The left picture is before the sample was cut, while the right is after it was cut with water as cooling medium. This sample corresponds to the left cluster in Figure 4-14.

In Figure 4-20, it can be seen that most of the sample is covered with orange corrosion products. Upon cutting, the colors have faded, but it still seems like the corrosion products are present. The samples presented in Figure 4-20 corresponds to the left cluster of samples presented in Figure 4-14.

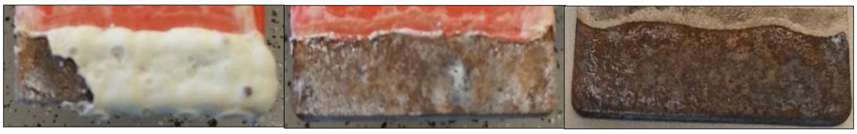

Figure 4-21: Picture of a 25Cr-sample before GIXRD analysis. It was tested in artificial seawater at -800 mV DC and 1000 A/m^2 AC. The left picture is just after the sample was removed from solution, the middle picture is before cutting and the right picture is after it was cut with water as cooling medium. This sample corresponds to the left pictures in Figure 4-18.

In Figure 4-21, it can be seen that the sample have corroded beneath the calcareous deposits. Further, there is little difference between the cut and the uncut sample. It seems like the remains of the deposits were washed away by the cooling medium. The samples presented in Figure 4-21 corresponds to the left pictures of samples in Figure 4-18.

4.4 Microscopic surface characterization

The samples were examined in XRD, GIXRD, SEM and EDS. XRD analysis was performed on powder from formed deposits and cell sediments, while GIXRD was performed on films on the sample surface prior to cleaning. All the samples that were observed in SEM and EDS were observed post cleaning.

The XRD tests were set for 30 minutes each, with the following set up parameters: fixed divergence slit of 0.2° and a 2θ-range of 10-75°. The GIXRD tests were set for 2 hours each with fixed divergence slit, 2.5° incidence slit and a 2θ-range of 15-70°. SEM and EDS analysis were performed with an accelerating voltage of 15 kV and a working distance of approximately 10 mm. In addition, SEM was operated in low current-mode with aperture size of 30 µm, while EDS was operated in high current-mode and an aperture size of 120 µm.

4.4.1 XRD analysis

XRD analysis of calcareous deposit formed on 25Cr in seawater at -800 mV DC and 1000 A/m^2 AC can be seen in Figure 4-22. The red column in the figure shows that the deposit consisted of $Mg(OH)_2$, the blue displays $CaCO_3$ and the green shows NaCl.

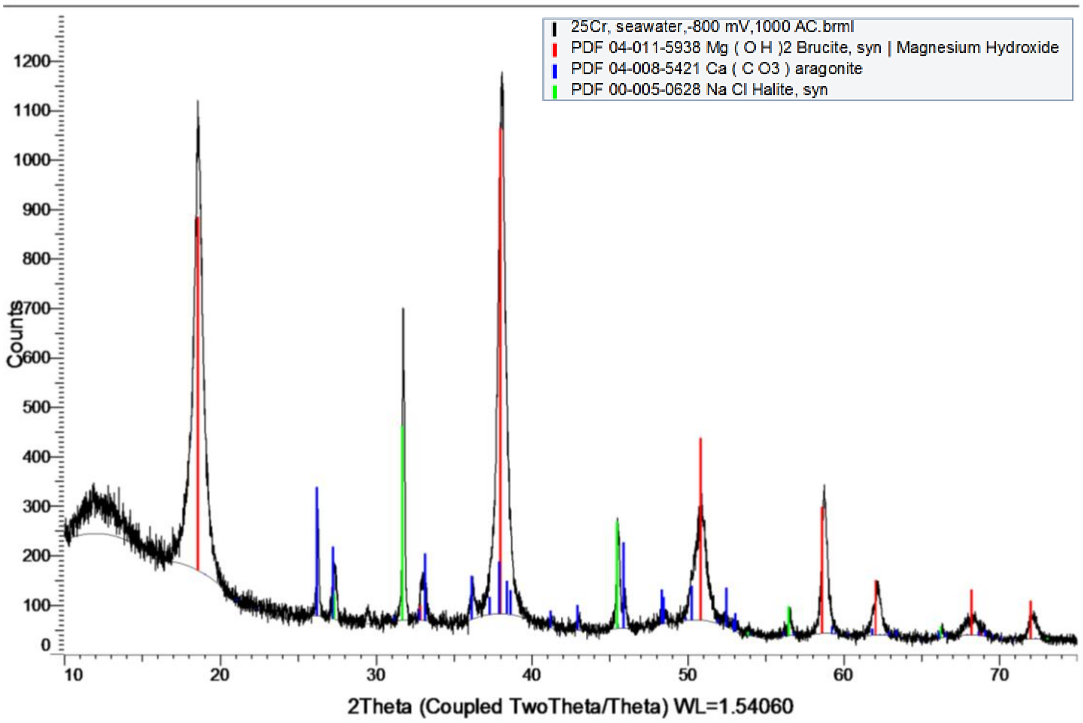

Figure 4-22: X-ray diffractogram of crushed calcareous deposit formed on 25Cr tested in artificial seawater at -800 mV DC and 1000 A/m^2 AC. This corresponds to the pictures on the left row in Figure 4-18 and the sample in Figure 4-21.

The results from the XRD analysis performed on 316 in seawater at -800 mV DC and 1000 A/m^2 AC were identical to the one displayed in Figure 4-22. Thus, the diffractogram is presented in Appendix E. Further, the analysis of the cell sediments that were formed during the experiment on X65 in seawater, tested at -800 mV DC and 500 A/m^2 AC, showed only NaCl. These results are also presented in Appendix E.

4.4.2 GIXRD analysis

GIXRD analysis of surface films on X65 and 25Cr tested in NaCl and seawater can be found in Figure 4-23 to 4-25. The analysis of an X65-sample tested in NaCl at -800 mV DC and 700 A/m^2 AC are presented in Figure 4-23.

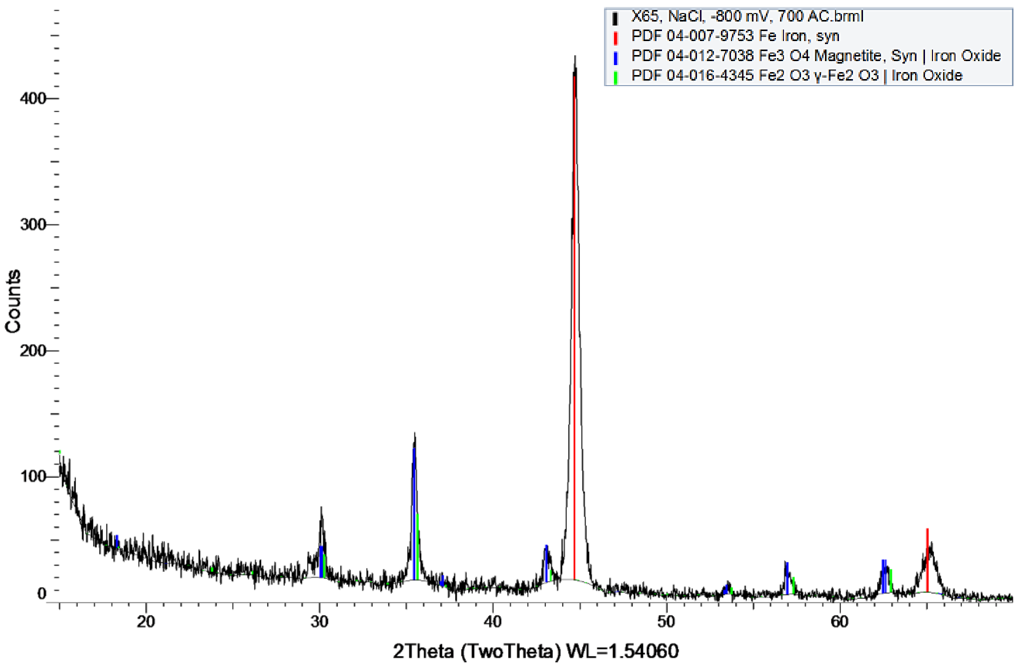

Figure 4-23: X-ray diffractogram of a surface film on a X65-sample tested in 3.5 % NaCl-solution at -800 mV DC and 700 A/m^2 AC. This corresponds to the picture in Figure 4-19.

In Figure 4-23, the red column shows the base material, Fe. The blue and green column shows Fe_3O_4 and Fe_2O_3, respectively. The two latter columns are very similar and almost overlapping due to similar crystal structure. This could mean that only one of them is present, or both at the same time.

The analysis of an X65-sample tested in seawater at -800 mV DC and 500 A/m^2 AC are presented in Figure 4-24. The pink column represents the base metal, Fe. The red line determines that $CaCO_3$ is present, while the green one shows γ-FeOOH (lepidocrocite), which may not be present as most of its peaks are also characterized by other species. Fe_2O_3 is represented by the blue column, which have one column that is not placed within a large peak. However, one peak is characterized by Fe_2O_3 only, and Fe_2O_3 is thus likely to be present.

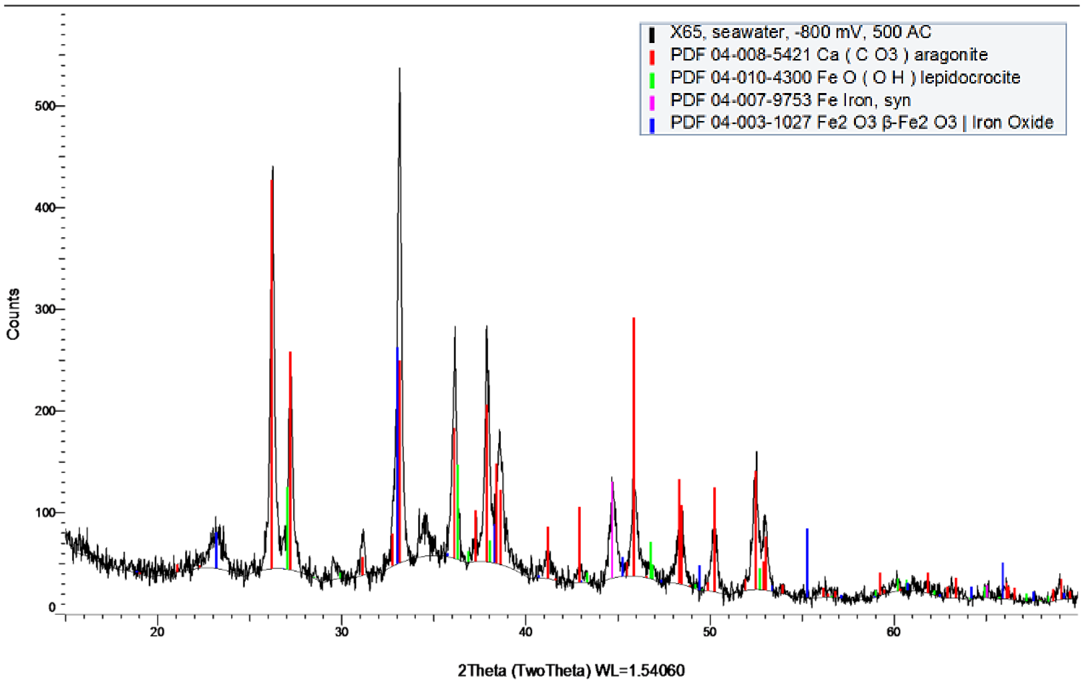

Figure 4-24: X-ray diffractogram of a surface film on an X65-sample tested in artificial seawater at -800 mV DC and 500 A/m² AC. This corresponds to the picture in Figure 4-20 (which is tested at same parameters as the left cluster in Figure 4-14).

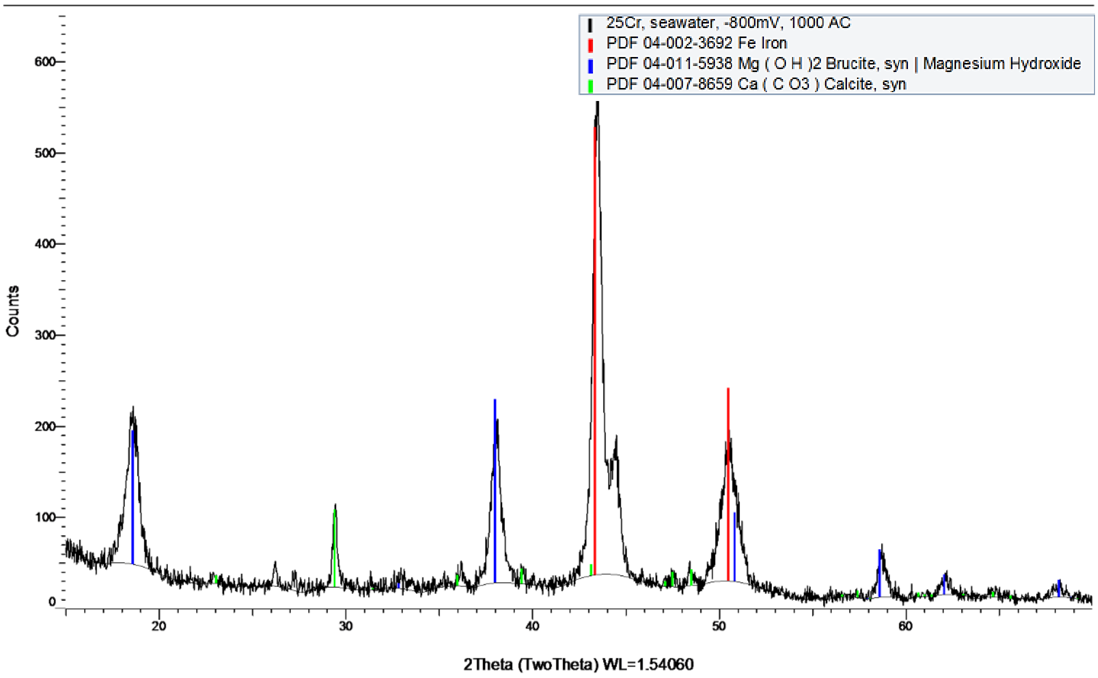

Figure 4-25: X-ray diffractogram of a surface film on a 25Cr-sample tested in artificial seawater at -800 mV DC and 1000 A/m² AC. This analysis corresponds to the picture in Figure 4-21 (and tested at the same parameters as the left part of Figure 4-18).

The analysis of a 25Cr-sample tested in seawater at -800 mV DC and 1000 A/m^2 AC are presented in Figure 4-25. The red column represents the base metal, Fe. The blue line determines that $Mg(OH)_2$ is present and the green line represents $CaCO_3$.

4.4.3 SEM analysis

This chapter presents the SEM images of importance that was acquired during the SEM analysis.

4.4.3.1 SEM analysis of various surface roughness

SEM images of X65-samples with different surface roughness and tested in different solutions at 500 A/m^2 AC and -800mV or -1050 mV DC, can be seen in Figure 4-26 to 4-28.

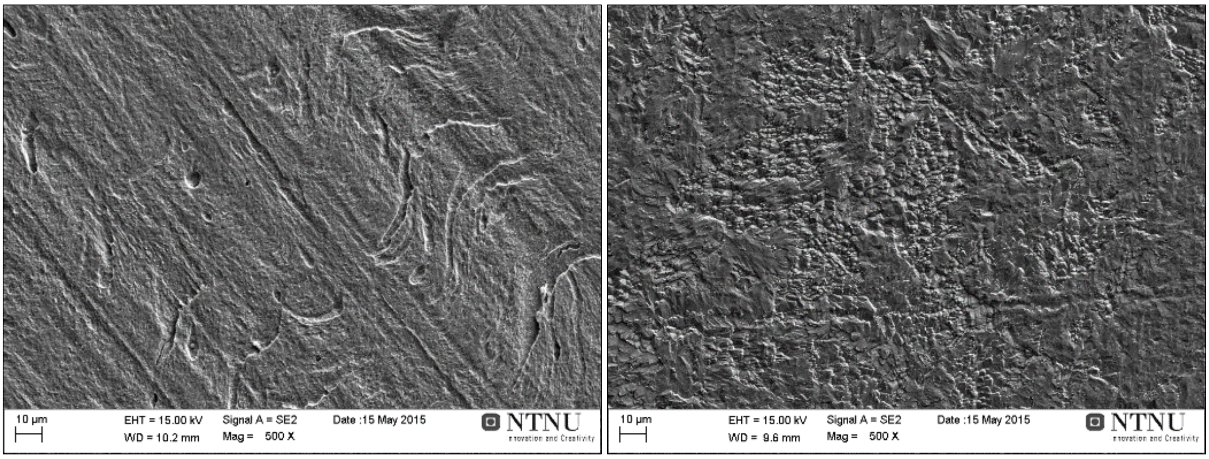
10 µm
EHT = 15.00 kV
WD = 10.2 mm
Signal A = SE2
Mag = 500 X
Date :15 May 2015
NTNU
Innovation and Creativity
10 µm
EHT = 15.00 kV
WD = 9.6 mm
Signal A = SE2
Mag = 500 X
Date :15 May 2015
NTNU
Innovation and Creativity

Figure 4-26: SEM images taken of X65-samples with different surface roughness, tested in 3.5 % NaCl-solution at -800 mV DC and 500 A/m^2 AC. The left sample is milled and the right is grinded to 1000 grit. Images are taken with a magnification of 500 X.

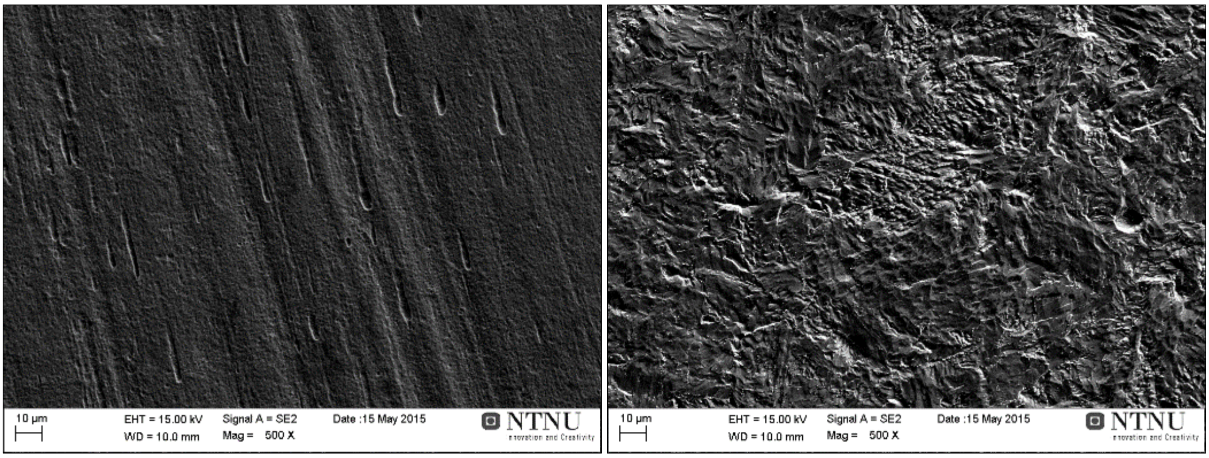
10 µm
EHT = 15.00 kV
WD = 10.0 mm
Signal A = SE2
Mag = 500 X
Date :15 May 2015
NTNU
Innovation and Creativity
10 µm
EHT = 15.00 kV
WD = 10.0 mm
Signal A = SE2
Mag = 500 X
Date :15 May 2015
NTNU
Innovation and Creativity

Figure 4-27: SEM images taken of X65-samples with different surface roughness, tested in artificial seawater at -800 mV DC and 500 A/m^2 AC. The left sample is milled and the right is grinded to 1000 grit. Images are taken with a magnification of 500 X.

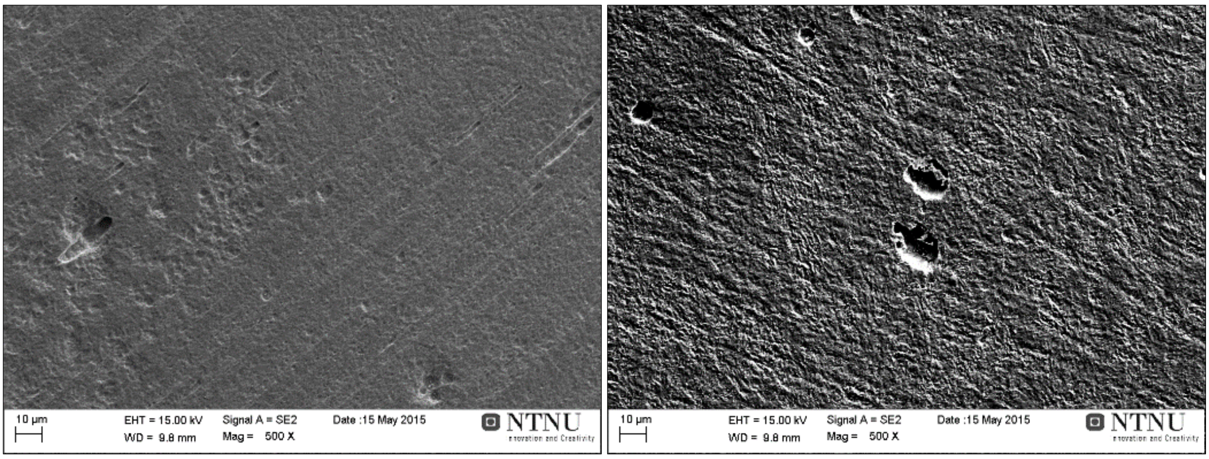
10 µm
EHT = 15.00 kV
WD = 9.8 mm
Signal A = SE2
Mag = 500 X
Date :15 May 2015
NTNU
Innovation and Creativity
10 µm
EHT = 15.00 kV
WD = 9.8 mm
Signal A = SE2
Mag = 500 X
Date :15 May 2015
NTNU
Innovation and Creativity

Figure 4-28: SEM images taken of X65-samples with different surface roughness, tested in artificial seawater at -1050 mV DC and 500 A/m^2 AC. The left sample is milled and the right is grinded to 1000 grit. Images are taken with a magnification of 500 X.

For all pictures displayed in Figure 4-26 to 4-28, the biggest holes that can be seen are not from pitting but rather because of surface treatment. From the images, it can be seen that there is some difference between the various surface topographies. For the pictures on the left hand side that are milled, corrosion has occurred uniformly. The pictures on the right hand side that have been grinded seem to have corroded uniformly as well. However, spots where the initial stages of pitting have occurred can also be seen for the latter.

4.4.3.2 SEM analysis of AISI 316 SS

SEM images of 316-samples tested in seawater at 500 A/m^2 AC and -800mV or -1050 mV DC, can be seen in Figure 4-29.

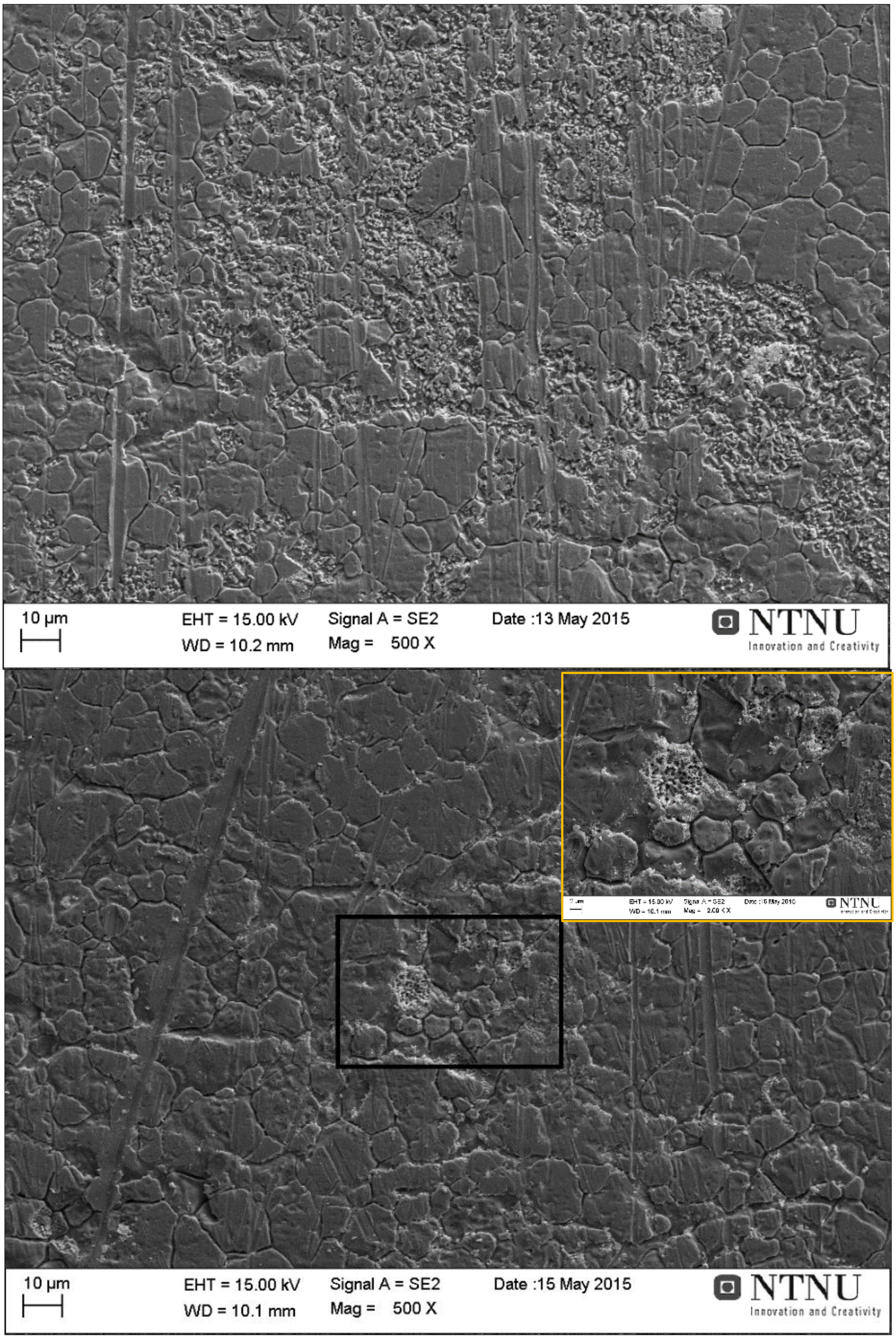
10 µm
EHT = 15.00 kV
WD = 10.2 mm
Signal A = SE2
Mag = 500 X
Date :13 May 2015
NTNU
Innovation and Creativity
10 µm
EHT = 15.00 kV
WD = 10.1 mm
Signal A = SE2
Mag = 500 X
Date :15 May 2015
NTNU
Innovation and Creativity

Figure 4-29: SEM images taken of 316-samples tested in artificial seawater at 500 A/m^2 AC. The top sample was polarized at -800 mV DC, the bottom at -1050 mV DC. Images are taken with a magnification of 500 X. The magnified square at the bottom image is at 2000 X.

From Figure 4-29, it can be seen that both samples suffer from the early stages of pitting. For the sample tested at -800 mV DC, the pitting is extensive and covers must of the surface. For -1050 mV DC on the other hand, only a few small spots have occurred.

4.4.3.3 SEM analysis of 25Cr SDSS

SEM images of 25Cr-samples tested in seawater and at -800 mV or -1050 mV DC can be seen in Figure 4-30 to 4-32. The samples in each figure have been tested at the following applied AC from top to bottom: 100, 500 and 1000 A/m^2.

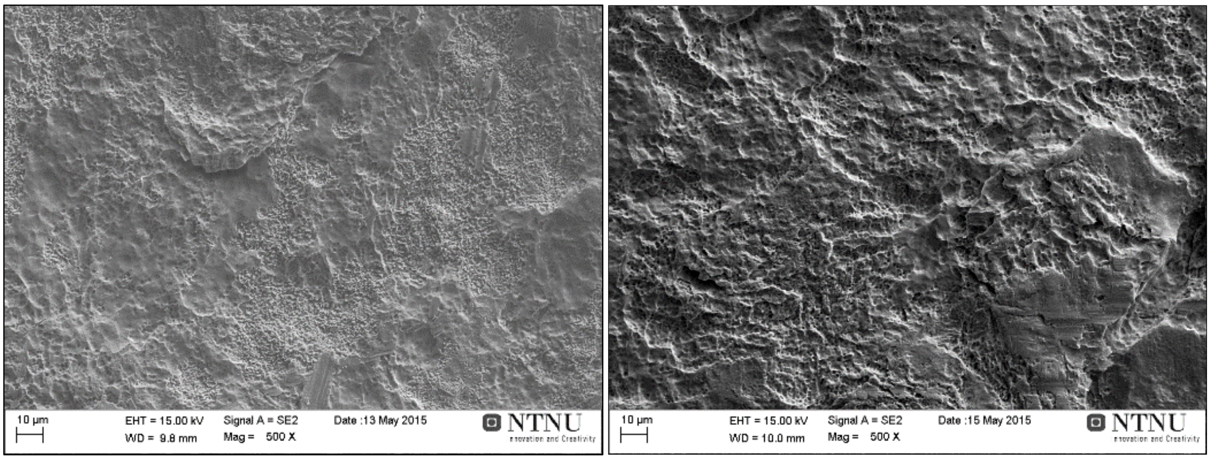
10 µm
EHT = 15.00 kV
WD = 9.8 mm
Signal A = SE2
Mag = 500 X
Date :13 May 2015
NTNU
Innovation and Creativity
10 µm
EHT = 15.00 kV
WD = 10.0 mm
Signal A = SE2
Mag = 500 X
Date :15 May 2015
NTNU
Innovation and Creativity

Figure 4-30: SEM images taken of 25Cr-samples tested in artificial seawater at 100 A/m^2 AC. The left sample tested at -800 mV DC and the right at -1050 mV DC. Images are taken with a magnification of 500 X.

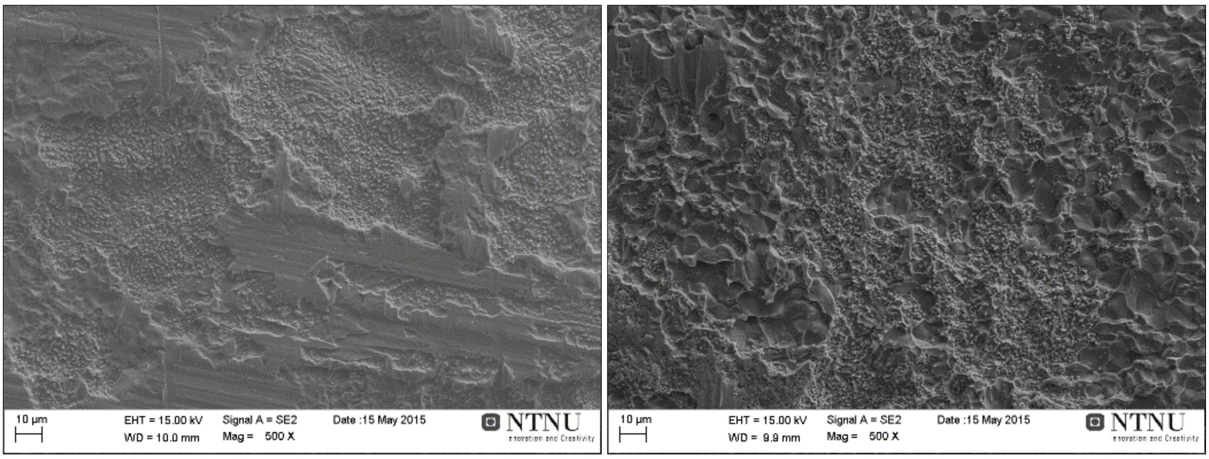
10 µm
EHT = 15.00 kV
WD = 10.0 mm
Signal A = SE2
Mag = 500 X
Date :15 May 2015
NTNU
Innovation and Creativity
10 µm
EHT = 15.00 kV
WD = 9.9 mm
Signal A = SE2
Mag = 500 X
Date :15 May 2015
NTNU
Innovation and Creativity

Figure 4-31: SEM images taken of 25Cr-samples tested in artificial seawater at 500 A/m^2 AC. The left sample tested at -800 mV DC and the right at -1050 mV DC. Images are taken with a magnification of 500 X.

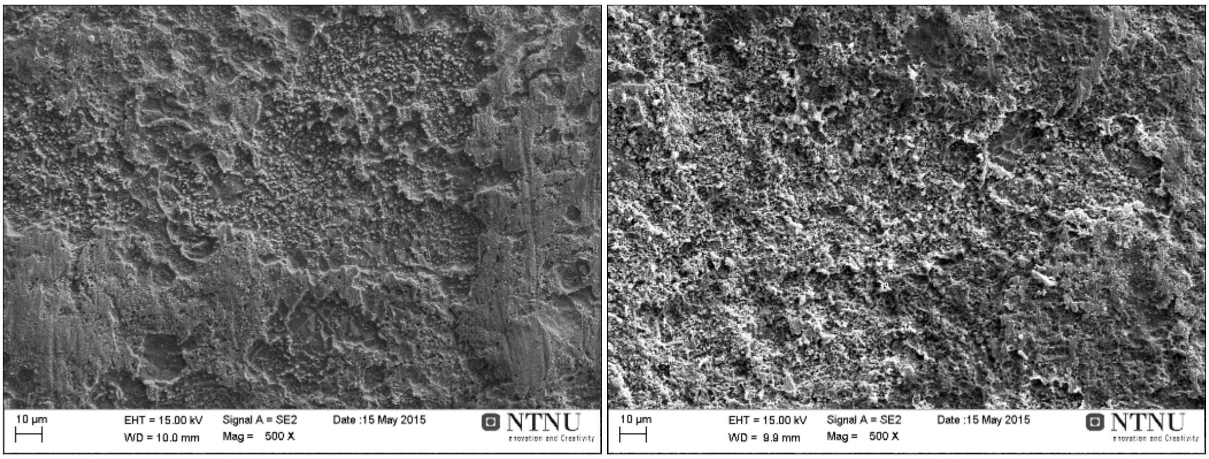
10 µm
EHT = 15.00 kV
WD = 10.0 mm
Signal A = SE2
Mag = 500 X
Date :15 May 2015
NTNU
Innovation and Creativity
10 µm
EHT = 15.00 kV
WD = 9.9 mm
Signal A = SE2
Mag = 500 X
Date :15 May 2015
NTNU
Innovation and Creativity

Figure 4-32: SEM images taken of 25Cr-samples tested in artificial seawater at 1000 A/m^2 AC. The left sample tested at -800 mV DC and the right at -1050 mV DC. Images are taken with a magnification of 500 X.

From the images, it can be seen that all samples suffer from initial stages of pitting. Some samples, like the one at -1050 mv DC and 500 A/m^2 AC in Figure 4-31, seems to be exposed to more uniform corrosion as well. Further, the sample tested at -1050 mV DC and 1000 A/m^2 AC in Figure 4-32 seem to be covered with some bright deposits, a tendency that barely can be seen in the on at -800 mV DC also. However, it is difficult to deduce any general trend.

4.4.4 EDS analysis

A SEM image from the darkest area of a cleaned 25Cr-sample that was tested in seawater at -800 mV DC and 500 A/m^2, which corresponds to the left sample in the right cluster of Figure 4-17, was examined in EDS. The measured chemical composition displayed only Pt and its results are presented in Appendix F.

4.5 Observations during experimental testing

4.5.1 Initial color on sample surface

Some samples of X65 were observed during the start-up phase of the experiments, and it was seen that the whole sample surface turned black after a short amount of time. Not as dark as towards the end of experiments, but still with a distinct black color.

4.5.2 Chlorine evolution

During experiments, it was possible to observe that gas evolved at the samples. This could be seen immediately when AC was tuned on, often formed as a chain of big bubbles on the steel-coating interface initially. Upon removal of the sample and especially the solution, a distinct smell of chlorine could be sensed.

4.5.3 AC counter electrode

The AC counter electrode in one of the cells was seen to dissolve. This was discovered after one of the last tests (only two more were performed in that cell), which was performed on 25Cr in seawater at -800 mV DC and 1000 A/m^2 AC. The electrode was thin to begin with, but after this test, it got thinner and even lost some bits. A picture of the electrode after this test can be seen in Figure 4-33.

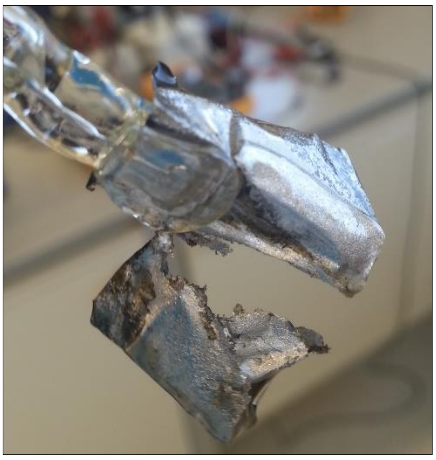

Figure 4-33: A photograph of the AC counter electrode that has started to dissolve.

4.5.4 pH measurements

Measurements with a standard pH meter in a 3.5 % NaCl-solution after the sample had been removed showed an increase in pH, with higher values for an increase in negative direction of DC. pH-values before testing were approximately 6, and ended up at about 7.5 for -800 mV DC and 8 for -1050 mV DC.

The same measuring method on artificial seawater after testing with X65-samples showed a decrease in pH with the same trend for DC-potential. There the start pH was 8.2 and the end value were around 7.9 for -800 mV DC and 6 for -1050 mV DC. At 316 and 25Cr, there were no difference between the DC-potentials and all experiments ended up on about 7 after a start pH of 8.2

The experiments on 316 and 25Cr were also tested with pH-strips. This testing was done in the solution right before testing ended and directly on the steel sample upon its removal from the solution, and showed values of about 5 and 10 respectively. Although not a very accurate method, it gives a pointer.

4.6 Summary of results

DC current response and AC cell potential

Although some experiments started out with an anodic DC current response, all quickly shifted to cathodic. Further, the samples tested in NaCl showed increasing or stable cathodic values, while in seawater decreasing cathodic values was the case. There was found no difference for variation in surface topography. For 316 and 25Cr, increasingly negative DC and increase in AC caused the DC current response to increase in cathodic direction. In Table 4-5, it can be seen that 316 and 25Cr display higher cathodic currents than X65, which again are higher than X65 (DC). Further, there is little difference between 316 and 25Cr, but the latter is slightly more cathodic.

The majority of recorded AC cell potentials showed little difference with time. The AC cell potential at X65 was seen to be higher for samples grinded to 1000 grit compared to milled samples. While X65 showed no difference in V_{AC} with DC-potentials, 316 and 25Cr saw a tendency to decrease V_{AC} with increasingly negative DC. This can also be seen in Table 4-5, which also shows higher V_{AC}-values for 25Cr and 316 compared to X65, where 25Cr is slightly higher than 316.

Table 4-5: Key results from the DC current response and AC cell potential during polarization, for all DC-potentials and and types of metal. All samples were under applied AC of 500 A/m^2, except for X65(DC), which was tested in absence of AC. V_{AC_avg} is averaged over the whole experiment, i_{net_start} is collected 2.5 hours into the experiment and i_{net_end} is collected at the end. The collected values for X65 are also averaged over the two surface topographies.

Metal sample	**-800 mV DC**			**-1050 mV DC**		
	V_{AC_avg} [V]	i_{net_start} [A/cm^2]	i_{net_end} [A/cm^2]	V_{AC_avg} [V]	i_{net_start} [A/cm^2]	i_{net_end} [A/cm^2]
X65 (DC)	0	-3.17E-5	-1.47E-5	0	-1.41E-4	-3.46E-5
X65	1.55	-4.54E-5	-3.54E-5	1.56	-6.87E-4	-8.55E-4
316	2.14	-1.23E-3	-2.63E-4	1.62	-2.79E-3	-1.55E-3
25Cr	2.25	-1.17E-3	-2.82E-4	2.05	-2.98E-3	-2.33E-3

Weight loss measurements

It was found that the CR was unaffected by the surface topography, and that the CR is slightly higher for NaCl than seawater (although there is very little difference at -1050 mV DC). It was also discovered that corrosion does not necessarily continue on an X65-sample, even if it is stored for months prior to cleaning.

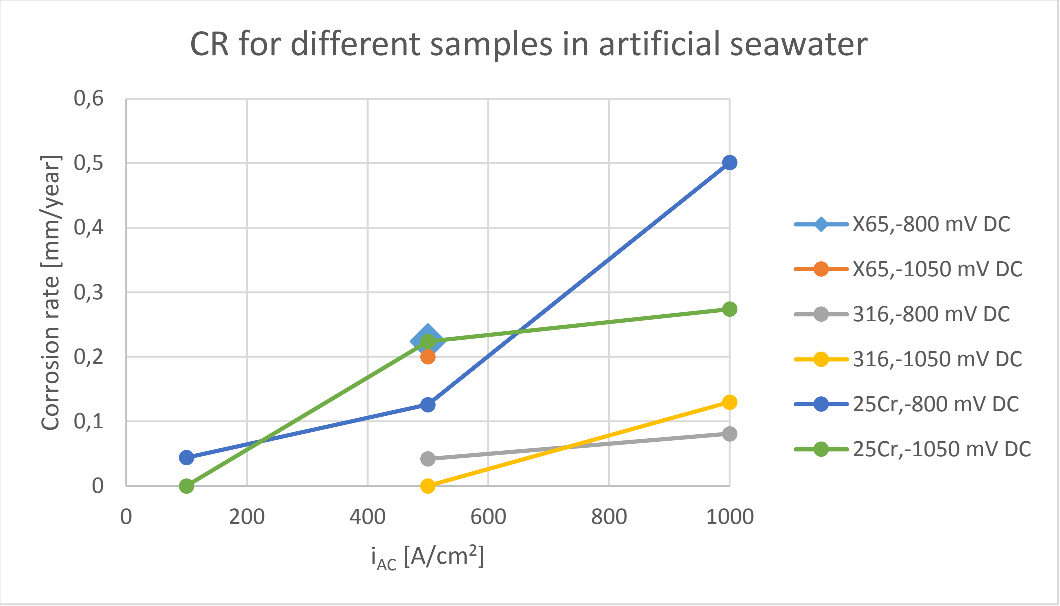

Figure 4-34: Calculated corrosion rate for all different-samples tested (at different ACs under -800 and -1050 mV DC) in artificial seawater. The CR-values are averaged for the experiments tested twice, but deviations are not included.

As Figure 4-34 shows, an increase in AC increases the CR. There does not seem to be any trend on how DC-potential influences CR. At low AC current densities, CR is highest for X65. At medium AC, 316 have the lowest CR and 25Cr is similar to X65. At high current densities, the CR of 316 is significantly lower than for 25 Cr.

Surface characterization

Macroscopic characterization showed that the corrosion products that were formed at X65 were mainly black in color, although some areas were orange. When X65 was tested in seawater at -1050 mV DC, and for all tests on 316 and 25 Cr, calcareous deposits formed. More was formed at higher AC current densities and increasingly negative DC. It was showed that corrosion occurred beneath these deposits. Lastly, a black insoluble layer with varying intensity formed on 316 and 25Cr after cleaning.

XRD analysis determined that calcareous deposits consisted of $Mg(OH)_2$ and $CaCO_3$. Both species and especially the latter were also found on an X65 surface and a 25Cr surface, which did not show a mentionable amount of calcareous deposits during the macroscopic observation. The corrosion products that were found were Fe_3O_4, Fe_2O_3 and possibly γ-FeOOH (lepidocrocite). SEM micrographs showed that most samples suffered from initial stages of pitting, and a few from uniform corrosion. EDS-analysis of black insoluble layer after cleaning proved it consisted of platinum (Pt).

5 Discussion

This section contains a discussion of the results and the experimental work. The different aspects are discussed in the same order as they were presented in the results. Towards the end of this section, suggestions for further work will also be presented.

5.1 Polarization behavior

5.1.1 Current behavior

All the samples of X65 that were tested showed cathodic currents in the DC current response for most parts of the testing period, as seen in Figure 4-1 to 4-5. A cathodic current means that the cathodic reaction is enhanced, and thus will a high cathodic current mean that the cathodic reaction occurs at a high rate. At a cathodic current, the cathodic reaction will be the rate-controlling part of the total reaction.

In both 3.5 % NaCl-solution and artificial seawater, the following tendency was seen initially at 500 A/m^2 AC: at a DC of -1050 mV, the DC current response began with cathodic currents and stayed within that region. At -800 mV DC however, the DC current response showed anodic currents initially. It took approximately 1 hour in 3.5 % NaCl-solution and 3 hours in artificial seawater, before the anodic currents shifted to cathodic. As can be seen in Figure 4-1, this is not the case in absence of AC, meaning it is promoted by the superimposition of AC. However, due to the short time interval where the anodic currents occur, and since it has been reported [26] that it is not necessarily directly affecting the corrosion rates, it is not an important aspect.

The same tendency to the cathodic currents that are observed for X65 is observed at samples of 316 and 25Cr, seen in Figure 4-8 and 4-10 respectively. This means that cathodic currents were seen for all tested samples of all types of steel. This coincide well with some studies [26, 27, 35] performed on both CS and SSs, and partly with another study [30] by L. Y. Xu et al performed on CS. The latter reported anodic DC current density when AC was applied at -850 mV DC. The authors gave no explanation to why this occurred. Their experiments were performed on 16Mn steel in simulated soil solution, but it is unknown to what degree this would affect the results compared to the results from this thesis.

For the samples of X65 that were prepared with different surface roughness, there were found little difference in the recorded DC current density. Although the curves were dissimilar between the solutions and different DC-potential applied, the samples tested at same parameters were very similar in terms of both form and values. This indicates that the different reactions and processes that occur on the steel surface are not affected by an uneven topography. For instance, the reduction of oxygen will happen with equal speed and scale regardless if it occurs on a flat or uneven surface. It is worth mentioning however, that even the milled samples were quite flat on a macroscopic level, but one can clearly see the lines across the samples.

An aspect that was seen for the different solutions is that for 3.5 % NaCl-solution the cathodic current increased or remained constant, whereas for artificial seawater it decreased. A likely explanation for this is the formation of calcareous deposits that was seen to develop at the samples tested in artificial seawater. The deposits act as a barrier that partly covers the surface, which is likely to reduce the extent of the cathodic reaction and thus the necessary current input. This reduction in cathodic current, which means that the cathodic reaction is less dominant and thus is reduced, could indicate that the main cathodic reaction is reduction of oxygen as seen in equation (2.9). The reason for this is that calcareous deposits have been reported to reduce diffusion of oxygen from bulk to surface [22]. Thus, if oxygen is the determining cathodic reaction, less oxygen will be present at the surface and the extent of the cathodic reaction will be reduced, which will reduce the cathodic currents. This is however, contradictory to other studies [26, 41-44] that have reported hydrogen evolution, according to equation (2.11), as the controlling cathodic reaction at high AC current densities (set to i_{AC} > 100 A/m^2 on 316 and 25Cr by C. H. M. Hagen).

The samples of 316 (Figure 4-8) and 25Cr (Figure 4-10) have very similar DC current responses in terms of both value and form, while X65 is quite different. X65 shows little variation with time and display low cathodic currents, while 316 and 25Cr display a clear decrease with time and at higher values. This is the case for both applied DC-potentials. Further, the DC current response for X65 with and without applied AC is quite similar. The cathodic currents are, as expected, in the following ranking from high to low: 25Cr>316>X65>X65(DC). Despite the high degree of similarity between samples of 316 and 25Cr, there is a difference in the form of some curves. This is the case for experiments conducted at high total currents, like 500 and 1000 A/m^2 AC at -1050 mV DC and 1000 A/m^2 AC at -800 mV DC. While these experiments at 316 are stable with a steady decrease in cathodic current, the same experiments on 25Cr have a few unstable drops. This is especially visible for the 25Cr-sample tested at -800 mV DC and 1000 A/m^2 AC, which was tested twice and is presented in Appendix D. The drops that are seen are instant increases in cathodic current that usually relocates very quickly. The highest drop is from approximately -1.0E-3 to about -2.8E-3, and there are several smaller ones. This unstable tendency has not been reported earlier, and it is unknown why this occurs. Since an increased cathodic current means that the electron consumption is increased, a possible explanation could be that an increased electron consumption is a consequence of a higher amount of free electrons due to anodic dissolution. If 25Cr is only able to maintain passivity to a certain degree, the spots may be short intervals where the steel loses its passivity. Then, for a short amount of time, the anodic dissolution increases and more free electrons are formed. Another possible solution to this unstable tendency is that high applied AC and less negative DC, causes the formed calcareous deposits to be unstable. This will be reviewed more in section 5.3.

Another similarity worth noting is the form of two of the curves recorded on 316 and 25Cr. The curves on both steel samples were recorded from the experiments performed at -1050 mV DC and 1000 A/m^2 AC, where the one performed at 316 is the re-tested sample. Both display high initial cathodic currents, significantly higher than experiments with other parameters within the same steel. When experiments are initiated they suffer an immediate decrease in cathodic current, followed by a round drop in current, and then with a steep decrease again. The sample at 316 suffers a change from an initial value at about -6.7E-3 to an end value of about -1.8E-3. For the 25Cr sample, the change is approximately from -7.2E-3 to -2.9E-3. This will be discussed further in section 5.2 and 5.3, and briefly mentioned in 5.1.2.

5.1.2 AC cell potential

For all the samples tested, the measured V_{AC} was seen to maintain its value more or less through the experiment. For the X65-samples at Figure 4-6 and 4-7, there were seen no or inconsistent correlation between the recorded DC current response and the V_{AC}. What was seen however, was a difference between milled and grinded samples. In both artificial seawater and 3.5 % NaCl-solution, the measured V_{AC} was higher for samples grinded to 1000 grit compared to the milled ones. This can be explained by different resistances in the circuit. As the AC cell potential is measured in parallel with the working electrode and the counter electrode, it measures the potential difference over the two electrodes. In a cell, this can be described by ohmic resistances on the electrodes as seen in equation (5.1). Worth noting is that the area of the working electrodes and thus the currents were similar for all the tested samples during the examination of surface roughness.

$$\Delta V_{AC} = \Delta V_{AC-Pt} - \Delta V_{AC-Steel} = (V_{AC-Pt} - I * R_{Pt}) - (V_{AC-Steel} - I * R_{Steel}) \tag{5.1}$$

On a steel surface with a rougher and more uneven surface topography, it is more likely that the ohmic resistance (R_{Steel}) is increased due to gas bubbles and corrosion products being caught on the surface. This could explain why the measured V_{AC} is higher for the finer surface topography of 1000 grit, when it is expected to be lower. However, another factor that is assumed to play a role is the external resistance, for instance in wires and other equipment. All milled samples were tested with one set up and all grinded samples were tested with another set up. Therefore, there could be a difference in external resistance, which could have affected the results.

The measured V_{AC} for 316 (Figure 4-9) and 25Cr (Figure 4-11) are similar, and both showed that the V_{AC} increases with an increase in applied AC and less negative DC. Similar to X65, there were found little correlation between the DC current response and V_{AC}. One similarity that can be found for the V_{AC} at 316 and 25Cr, is that for the same experiments as mentioned in the last paragraph of section 5.1.1, tested at -1050 mV DC and 1000 A/m^2 AC (re-tested sample at 316). A big drop in the V_{AC} can be seen at approximately the same hours as the smaller drop was seen at the recorded current response.

For all types of steel, there were a similarity in terms of relative values between V_{AC} and the DC current response. The found V_{AC} was as expected and in correlation with the DC current response, in the following order from high to low: 25Cr>316>X65, with a small difference between 25Cr and 316.

5.2 Weight loss and corrosion rates

The cathodic protection system applied by the potentiostat was believed to protect the samples from corrosion, despite a calculated CR of 0.041 mm/year for the sample tested at -800 mV DC in artificial seawater. The reason for this is that this value is seen as faulty. This sample corresponds to the grey line in the DC current response displayed in Figure 4-1. It is believed that when the salt bridge lost contact, the potentiostat applied extreme current values to try to hold the potential constant, without succeeding. Thus, some corrosion occurred before contact was reestablished.

The weight loss and calculated CR of the X65-samples that was either milled or grinded to 1000 grit, was similar independent on the surface topography. In 3.5 % NaCl-solution, the CRs were very similar with a difference in the area 0.001-0.011 mm/year. The difference was a bit higher in artificial seawater where the highest one was 0.021 mm/year, but still within acceptable variance. Thus, an increase in V_{AC} does not necessarily mean an increased CR, as stated in a previous study [31], since V_{AC} was seen to be higher for the grinded samples in this thesis. Further, it was seen that the CRs were lower in artificial seawater than in 3.5 % NaCl-solution. This was mainly visible at -800 mV DC where the difference, when averaged over surface topography, was 0.069 mm/year, which means an approximately 30 % decrease in CR for artificial seawater. At a DC of -1050 mV DC however, the difference in CR was as small as 0.027 mm/year, which is a decrease of 13 %. Thus, it can be concluded that the CR to some degree is reduced in artificial seawater, which is similar to another study [29] and falls in between several earlier studies [24, 27, 35] (whereas one is in absence of AC). An obvious reason for this is the formation of calcareous deposits, which have been shown to decrease corrosion. Another cause may be the buffer capacity that seawater possesses, as described in section 2.3.4. During measurements of pH before and after experiments, it was showed that pH changes with 1.5-2 in 3.5 % NaCl-solution, while in artificial seawater the change was 0.3-2.2

Compared to other studies performed on X65 under applied AC, the results presented here (0.191-0.297 mm/year) matches several of them within reasonable values: 0.205-0.236 mm/year[26], 0.15-0.17 mm/year [29], 0.1-0.3 mm/year[30] and 0.15-0.3 mm/year[42]. Some studies have also found higher CRs [27, 29, 35]. In addition, the CR of the X65-sample that was stored in a desiccator before cleaning was calculated to 0.215 mm/year. Thus, storage of the samples prior to cleaning could not have been the cause for the unreasonably high CRs during the author's specialization project.

The calculated CRs for 316-samples varied a lot as seen in Table 4-2, from not corroding at all to a CR of 0.260 mm/year. The CR with the highest deviation is the latter one, as the others are in the area of 0-0.081 mm/year. In addition, the experiment (performed at -1050 mV DC and 1000 A/m^2 AC) that gave a CR of 0.260 mm/year was re-tested, and then CR was found to be zero. The corresponding DC current response and AC cell potential for these experiments have been discussed in section 5.1.1 and 5.1.2, respectively. The corresponding DC current responses in Figure 4-8 was seen to suffer a major decrease in cathodic current for the re-tested sample that has a CR of 0, while a regular decrease was seen for the sample with a CR of 0.260 mm/year. It is thus believed that the DC current response correlates with the CR to some degree. This will be discussed further in section 5.3.

The CRs that were calculated for 25Cr-samples were seen to be quite high, a lot higher than expected. The only experiment where the sample suffered no corrosion was at -1050 mV DC and 100 A/m^2 AC. For the other experiments, the CR was in the area of 0.044-0.522 mm/year. The highest of 0.522 mm/year was seen at -800 mV DC and 1000 A/m^2 AC, while the rest of the samples that were tested at 500 and 1000 A/m^2 AC were in the area of 0.126-0.274 mm/year. Because of the significant difference between these experiments, the highest was performed twice with similar results. As 25Cr in general is seen to be immune to corrosion in seawater, it is unknown why such high CRs occur. Possible explanations could be that the metals passivation properties have little effect due to the oscillating nature of the AC, or that the composition of the samples was changed in some way during their manufacturing. The latter can easily be tested, and should be so prior to any further experiments.

Another likely explanation to these high CRs could be the formation of chlorine gas and presence of chlorine in the solution, which was observed during the experiments. It has been reported that SSs suffer from corrosion in chlorine gas: where the CRs are high for wet gas at low temperatures (about 10-100 °C) and dry gas at high temperatures (about 450-650 °C)

[48]. Similar as for SS, it has been reported that Pt corrodes in dry chlorine gas at high temperatures (about 500-1000 °C) [48, 49]. Thus, it is possible that Pt will corrode at low temperatures in wet chloride gas as well. This correlates to the observed dissolution of Pt during experiments. However, this explanation does not account for the difference in CR between 316 and 25Cr.

Another possible explanation for the high CRs seen in 25Cr is that high-applied ACs causes the steel to enter the transpassive area, as can be described in the pourbaix diagram in Figure 5-1. This could also be the case for the observed corrosion of the platinum counter electrode, as can be seen in the pourbaix diagram in Figure 5-2. From the diagrams, it can be seen that both SSs and platinum enter an area where they dissolve into ions at high potentials and high pH. However, neither this explanation describes why 25Cr corrodes at a faster rate than 316.

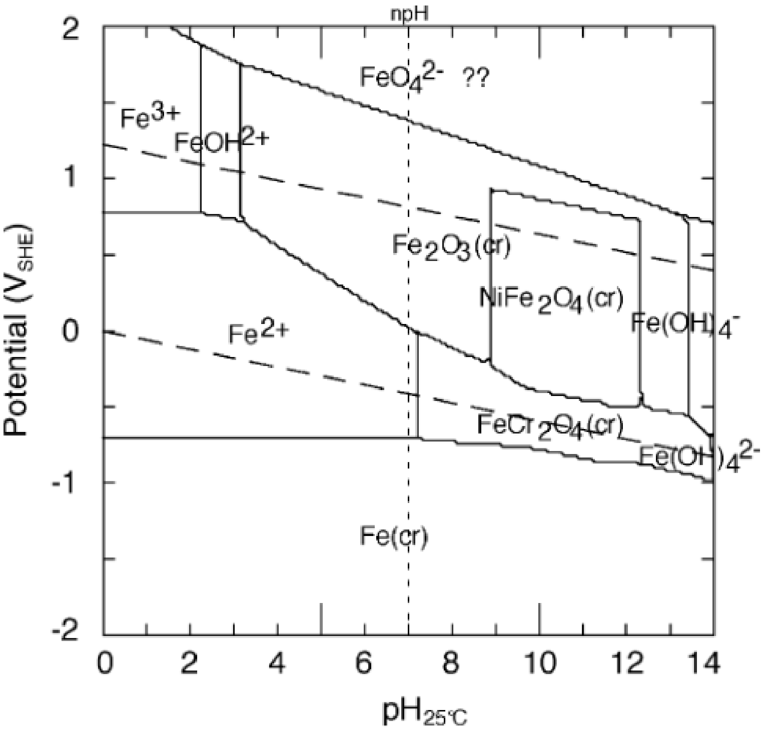

Figure 5-1: Pourbaix diagram for iron species in the ternary system of Fe-Cr-Ni at 25 °C. The question mark at FeO_4^{2-} indicates uncertainty on its stoichiometry and stability [50].

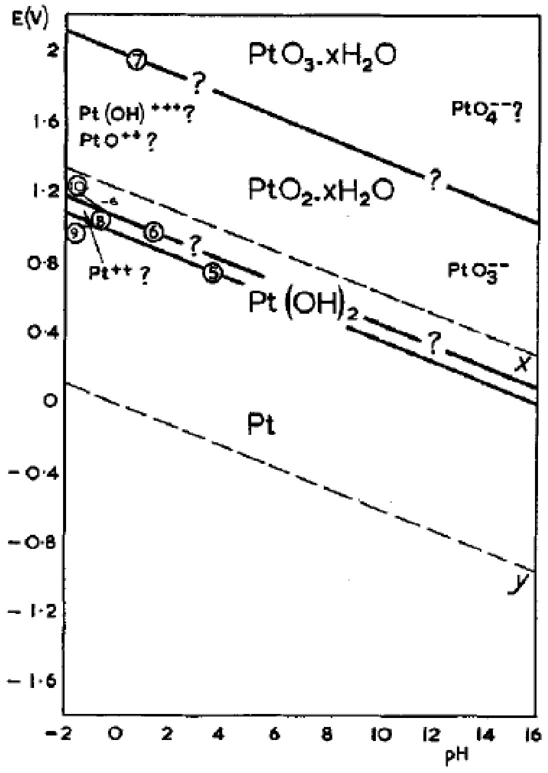

Figure 5-2: Pourbaix diagram for the platinum-water system at 25 °C. The question marks behind the ions on the left and right hand side indicate uncertainty due to lack of thermodynamic data [51].

Upon comparison with previous studies, the results on 316 and 25Cr are found to be similar. Former studies on 316 have presented CRs in in range of 0.007-0.113 mm/year in 3.5 % NaCl-solution [26] and 0.002-0.034 mm/year in artificial seawater [27], for applied ACs in the area of 100-1000 A/m^2. These are a bit lower than the CRs found in this thesis. For 25Cr, only anodic polarization and low applied AC has been performed, and at 100 A/m^2 AC the CR were found in the area 0.010-0.022 mm/year [26]. These are very similar to CR found in this thesis at 100 A/m^2 AC.

For all tested steels, it is clear that an increase in AC current density increases the rate of corrosion, which is clear in earlier reports as well. The effect of DC-potential varied between the different steels and with the different applied AC, making it difficult to deduce any trend. 316 was seen to have very low CR, which was expected, and even had the lowest CR compared to the other steels at both medium and high AC current density. Surprisingly, 25Cr had similar CR as X65 at medium applied AC. Compared to some studies, 25Cr even have higher CR than X65 at high AC current densities.

5.3 Surface characterization

In general, for the samples that were tested in artificial seawater, calcareous deposits were very common. This was the case for all steels. Of all the tested samples, the only ones that were not fully covered in calcareous deposits were the ones tested in 3.5 % NaCl-solution and the following in artificial seawater: X65 at -800 mV DC and 500 A/m^2 AC, and 25Cr at -800 mV DC and 100 A/m^2 AC. The latter of these had local spots were calcareous deposits had formed, while the other ones were black (3.5 % NaCl-solution) or black and/or orange (artificial seawater). Even though many of the samples were covered in calcareous deposits, it was visible upon removal that corrosion had occurred beneath, either before formation of deposits or during the whole duration of the experiments.

Five tests were analyzed through XRD to determine the composition of corrosion products and calcareous deposits. For the latter, it was hoped that corrosion products could be found within the deposits, which did not happen. The deposits consisted of $CaCO_3$ and $Mg(OH)_2$ (and NaCl), as described in theory [3, 23]. This indicates an increase in local pH, which is confirmed by the in situ pH measurements. More surprisingly, surface analysis of 25Cr showed that the sample surface consisted of the same species despite no visible calcareous deposits. This indicates that the formation of deposits is extensive and likely to be present and reduce risk of corrosion at all samples tested in artificial seawater. This is accompanied by the surface analysis of an X65-sample, as seen in Figure 4-24, which displays $CaCO_3$ (and other species) despite no visible calcareous deposits at the sample surface. In the theory [23], it is reported that $CaCO_3$ form with slower kinetics than $Mg(OH)_2$, and thus is the major component in calcareous deposits in the late stages of testing. Since $CaCO_3$ is the only component after a 48 hours test, it could indicate that the formation kinetics is increased upon applied AC. The absence of $Mg(OH)_2$ could also indicate that the reduction reaction is the formation of H_2, as seen in equation (2.11), since it does not produce OH^- that $Mg(OH)_2$ is dependent on.

In section 5.1.1, it was reported that instability of the recorded DC current density was seen from some of the experiments performed on 25Cr, especially at -800 mV DC and 1000 A/m^2 AC but also -1050 mV DC and 500 A/m^2 AC. One proposed possible solution was unstable calcareous deposits, and this can in fact be seen for those experiments in Figure 4-18 and 4-17, respectively. The calcareous deposits formed on the actual samples have some holes and areas of non-continuous deposits. However, this can also be seen for other experiments on 316.

The XRD analysis that were successful in characterizing corrosion products after testing, were performed on the sample surface of X65-samples. Fe_2O_3 was found on both samples. In addition, Fe_3O_4 was found on the one tested in 3.5 % NaCl-solution and γ-FeOOH (lepidocrocite) was found on the one tested in artificial seawater. However, the crystal structure of Fe_2O_3 and Fe_3O_4 are very similar, and when the black color seen at Figure 4-19 is taken into consideration, it is most probable that the surface tested in 3.5 % NaCl-solution only consisted of Fe_3O_4. These different corrosion products formed in different solutions coincide to a large degree with another study [24]. The reason to why no γ-FeOOH was found at the tests in 3.5 % NaCl-solution could be that the reaction towards Fe_3O_4, as in equation (2.17), is complete. While in artificial seawater the reaction in incomplete due to lower reaction kinetics (lower corrosion rates in artificial seawater). This is however, dependent on that the solid-state reaction (2.20) is complete.

For the X65-samples, there was actually seen a difference in the SEM micrographs for milled and grinded samples. The milled ones did not seem to suffer from pitting corrosion, but rather uniform. Why this occurs is unknown and unexpected, especially due to similar current behavior and CRs. The opposite could have been expected because an uneven topography might already have valleys or similar that act as pits. Of the other experiments, pitting was seen on all samples and uniform corrosion was seen on a few. However, the pitting that was observed was often very wide spread and in the initial stages. Thus, no big pitting-holes were observed, and there is little difference between this wide spread pitting and uniform corrosion. Experiments lasting longer would be necessary to determine how the corrosion would propagate, and to confirm if it really is pitting or not.

Except for the experiments on 316 at 500 A/m^2 AC, which displayed less extensive pitting at -1050 mV DC compared to -800 mV, there were seen no direct correlation between the extent of pitting and applied AC or DC as reported by C. H. M. Hagen [26].

The black insoluble product that remained on the samples after cleaning, was confirmed to be Pt as presented by C. H. M. Hagen [26]. An interesting aspect with the Pt-layer is that the color and thus the thickness of the layer vary between different samples. This variation can also be seen between samples that have been tested at the same parameters. As already mentioned, the DC current response of a 316 and a 25Cr-sample was discussed in section 5.1.1, and its corresponding AC cell potential discussed in section 5.1.2. In addition, the samples’ CR was discussed in section 5.2. Both samples were tested at -1050 mV DC and 1000 A/m^2 AC, and their DC current responses both showed irregular steep decrease in cathodic current. In the 316 case, the re-tested sample with these parameters had a CR of 0 while the original had a CR of 0.260 mm/year. The surface characterization in Figure 4-16 shows that the re-tested sample is significantly darker in color after cleaning than the original. It is thus possible, that the very low CR is due to high amount of Pt deposited. Similar for 25Cr. In Table 4-3, it can be seen that the CR of 0.522 mm/year tested at -800 mV DC and 1000 A/m^2 AC, is a lot higher than the one tested at -1050 mV DC and 1000 A/m^2, which has a CR of 0.274 mm/year. From Figure 4-18, it can be seen that the thickness of the Pt-layer at -800 mV DC and 1000 A/m^2 AC is lesser than the Pt-layer at -1050 mV DC and 1000 A/m^2 AC. This indicates that the CR from the latter test probably is reduced due to increased amount of Pt deposited. This is a potential big source of error, which puts the whole testing procedure to questioning.

5.4 The mechanism for AC corrosion

The mechanism behind AC corrosion is not clearly understood, and it is difficult to set any conclusion based on the results from this thesis. The pH measurements and the good growth conditions for calcareous deposits proves that a local increase in pH occur on the steel surface. Even though the procedure for measuring pH is inaccurate, it dismisses D.-K. Kim et al.'s [29] proposal that the pH is so high that the steel enters the active corrosion area of $HFeO_2^-$, as seen in Figure 2-6.

Based on pH measurements, it is likely that the pH is around 10-12 at the steel surface. Further, the mechanism is likely to be similar to what is described in Figure 2-7 in section 2.4.1, and explained in its corresponding text. This is supported by the observations described in section 4.5.1. As presented, the V_{AC} was in the region of approximately 1-3 V, which means that the anodic cycle reaches almost to the top of the pourbaix diagram in Figure 2-6, even at the lowest applied AC. This is far into the region where Fe_2O_3 is the stable species, and thus Fe_2O_3 should be formed. This is the case for the samples tested in artificial seawater, which had a measured V_{AC} at about 1.55 V. For the sample tested in 3.5 % NaCl-solution, the V_{AC} was not measured, but based on Figure 4-6 and 4-7 it is expected to be lower but still around 1 V. It is thus possible that the faradaic current caused equation (2.20) to be shifted to left during the cathodic cycle of the AC, forming Fe_3O_4 from Fe_2O_3. In artificial seawater, it is possible that the reaction continued according to equation (2.17), leading to formation of γ-FeOOH.

On the other hand, the pourbaix diagram Figure 5-1 indicates that the high V_{AC} brings the steel into the transpassive region of FeO_4^{2-}. This transpassive region has also been reported in a regular pourbaix diagram for iron-water-system [52]. This does not necessarily disprove the formation of the species mentioned in the last paragraph, but rather that the mechanism for AC corrosion is not as simple as described in Figure 2-7 in section 2.4.1.

It is clear that some of the faradic current during the anodic cycle leads to the formation of $Cl_{2\,(g)}$ according to equation (2.8). Further, it is likely that there is not only one reduction reaction occurring. It is possible that any of the reactions (2.9-2.11) occur at different times during an experiment and vary between the different experiments.

Several propositions to describe the mechanism of AC corrosion have been made, but none is able to explain the seen difference between 316 and 25Cr regarding the CR. Thus, it is difficult to draw adequate conclusions.

5.5 Evaluation of experimental work

Before experimental work was initiated, all wires and electrical equipment was checked for conductivity. Equipment with low conductivity was discarded to make sure that measured current was as accurate as possible. The majority of the used apparatus were satisfactory. However, the used VariAC was controlled manually. Thus, the applied AC was unsteady and changed over time, such that higher or lower values than intended was applied for a limited amount of time. Furthermore, it would have been favorable with better accuracy of the weights used for measuring weight loss. The used weights accuracy was about ± 1 mg, which is the same order of magnitude as most of the weight losses and may thus have had a significant effect on the results.

Another potential source of error, is that two different set ups were used during testing. This means two potentiostats, two cells etc. A minor error source is the different resistances in wires and equipment, as they to a certain degree can be accounted for. A bigger difference between the two cells were the counter electrode of Pt, where the area (and volume) of both electrodes were bigger in one cell compared to the other. This would cause a higher current density on the counter electrodes in the cell where the area of the electrodes were smallest. This would not usually be a problem, but as it is seen that the AC counter electrodes of Pt dissolve and deposit on the steel samples, it clearly is in this case. A solution may be to increase the area of the counter electrodes in order to reduce their current density so that the dissolution will reduce as well. Additionally, it would be favorable if the electrode-area were similar in the different cells. Another solution may be to use a different material as counter electrode.

The weakest part of this thesis is the lack of parallel testing. As was seen for the experiment performed twice on 316, there can be huge differences in the result. The results will thus rather serve as a pointer. Furthermore, in order to increase the reproducibility of the results, the coating method should be revised. Applying by hand as in this thesis gives a small variance in exposed area, which is undesirable. An easy way to coat the samples with equal exposed area would be to dip them in the coating solution upside down. The coating at the top were the clamps are connected can easily be removed when dry. This would however, be more time consuming than applying coating by hand.

One of the computers with a potentiostat crashed a couple of times. The potentiostat was able to apply the right amount of DC-potential despite crashing such that weight loss measurements was performable, but data like DC current response and AC cell potential was lost. This can be a frustrating element and should be avoided if possible.

The cleaning procedure related to removal of corrosion products on X65, also caused metal loss as described in Appendix B. This can be accounted for to a certain degree. However, it would still be preferable to perform a cleaning procedure were no metal loss will occur. ASTM G-1 has several suggestions of solutions that may work.

5.6 Suggestions for further work

Based on the experimental work and methodology performed in this thesis and in former work, a range of suggestions to better understand the mechanism of AC corrosion are presented in the following paragraphs:

- Perform similar experimental work as described in this thesis, but with a different set up regarding the AC counter electrode. It should be possible to separate the AC electrode and the working electrode in two different cells, connected with a salt bridge. In that way, the issue with Pt depositing on the tested sample will be removed.
- It would be interesting to perform galvanostatic polarization, which is to apply a constant current (DC) while measuring any change in the potential. Current shifts have been seen under constant potential and potential has been seen to decrease in open circuit, but it is unknown how potential react upon constant current.
- Perform accurate in situ pH measurements. This would be of interest both directly on the sample surface and in the solution. It could also be interesting to see pH as a function of time. An accurate pH measurement could with certainty limit or confirm some corrosion reactions.
- Perform accurate in situ temperature measurements on the sample surface. The purpose of the applied AC is to heat the steel samples, but its effect in these laboratory experiments is unknown. The temperature can be interesting regarding critical pitting temperature and critical temperature related to changes in microstructure. The latter is however unlikely.
- Measure the amount of hydrogen diffused into the samples, to assess the possible risk of hydrogen embrittlement in SSs. Regular cathodic protection has been seen to cause such problems and gas evolution is very high during AC experiments. It would be interesting to see if applied AC on CP increases the diffusion of H-atoms.
- Further characterization of corrosion products, preferably GIXRD analysis due to thickness of layer on the sample surfaces. Experiments should also be performed in 3.5 % NaCl-solution or similar, to avoid formation of calcareous deposits that disrupts the readings. Low applied AC current densities could also be a solution to reduce the amount of calcareous deposits that forms.

- Perform characterization of ions in the solution, both pre- and post-testing. This would be helpful in understanding which reactions that occurs.
- Increase experimental duration. This would serve as a more accurate method in determining the mechanism and severity of AC corrosion. Both XRD and SEM analysis would be simplified and give more accurate results. Further, the source of error related to weighing the mass loss would be reduced, as mass loss would increase. In addition, by testing at different time intervals one could see if the mechanism and severity of AC corrosion varies as a function of time.
- In situ and close up video recording of the sample surface. This would be especially interesting in the early stages, to evaluate the observations described in section 4.5.1. It could also act as support to either confirm or decline the proposed mechanisms. Another interesting aspect would be to inspect the gas evolution and any local corrosion.
- Perform experiments at even lower DC-potential. According to theory there should be a limit-potential where applied AC no longer will cause corrosion. If it is the case, it could be interesting to find it and determine a CP-system that ensures no corrosion.

6 Conclusions

The cathodic polarization behavior under applied AC have been studied for X65 CS, AISI 316 SS and 25Cr SDSS, in 3.5 % NaCl-solution and artificial seawater. Weight loss measurements and surface characterization by SEM and XRD were included in the study. Due to limited parallel testing the following conclusions will serve more as indications:

- Corrosion of tested samples did not continue upon storage in a desiccator.
- Surface topography had no effect on AC corrosion
- Cathodic currents were seen for all tested samples. Higher AC and more negative DC-potential increased the cathodic currents on 316 and 25Cr. Cathodic currents were in the following order from high to low, with small variation between the first two: 25Cr>316>X65 (with AC)>X65 (absence of AC).
- The AC cell potential (V_{AC}) showed little correlation to the DC current response. High applied AC caused high V_{AC}. Applied DC did not affect V_{AC} for X65, while for 316 and 25Cr the V_{AC} decreased with more negative DC-potential. V_{AC} was in the same order as the DC current response, with the highest value for 25Cr and similar small variation between 316 and 25Cr.
- Some correlation between CR and the DC current response were found. The correlation between DC-potential and CR were inconsistent, while an increase in applied AC was seen to increase the CR and cathodic currents. The following CRs were calculated for the various types of steel: 0-0.260 mm/year (316), 0-0.522 mm/year (25Cr) and 0.191-0.297 mm/year (X65).
- For equal experimental parameters, 500 A/m^2 applied AC and -800 mV or -1050 mV DC, the following CRs were calculated for the various types of steel: 0-0.042 mm/year (316), 0.126-0.224 mm/year (25Cr) and 0.191-0.297 mm/year (X65).
- Calcareous deposits were formed on all samples tested in seawater and usually consisted of both $CaCO_3$ and $Mg(OH)_2$. Higher applied AC and negative increase in DC-potential caused increased formation of deposits, and it is likely that applied AC increases the kinetics of formation.
- There was a small difference between 3.5 % NaCl-solution and artificial seawater regarding AC corrosion, more significant at -800 mV DC. CRs were a little lower for artificial seawater and DC current response displayed decreasing cathodic currents (compared to stable or increasing in 3.5 % NaCl-solution). Both are likely due to formation of calcareous deposits.
- Fe_3O_4 was seen to form in 3.5 % NaCl-solution, while Fe_2O_3 and γ-FeOOH formed in artificial seawater. However, this seemed to vary between experiments.

7 References

1. Nexans. *Direct Electrical heating (DEH)*. 2015 [cited 2015 23/2]; Available from: http://www.nexans.com/eservice/Corporate-en/navigate_276641/Direct_electrical_heating_DEH_.html.
2. Hosokawa, Y., F. Kajiyama, and Y. Nakamura, *Overcoming the New Threat to Pipeline Integrity - AC Corrosion Assessment and its Mitigation*, in *23rd World Gas Conference*. 2006, Tokyo Gas Co.: Amsterdam.
3. Forthun, K., *Alternating Current Corrosion of Aluminium Sacrificial Anodes*, in *Department of Materials Science and Engineering*. 2013, Norwegian University of Science and Technology: Trondheim.
4. Nisancioglu, K., *Personal communication*. 12/12-2014, Norwegian University of Science and Technology: Trondheim.
5. Kuang, D. and Y.F. Cheng, *AC Corrosion at Coating Defect on Pipelines*, in *Corrosion* 2014, NACE International.
6. Kulbotten, H. *Direct Electric Heating (DEH) - Basic technology*. 2008 [cited 2015 23/2]; Available from: https://www.tekna.no/ikbViewer/Content/745664/DEH-Basic%20Technology.pdf.
7. Nysveen, A., et al., *Direct electrical heating of subsea pipelines - Technology development and operating experience.* Ieee Transactions on Industry Applications, 2007.
8. Lervik, J.K., et al., *Direct electrical heating of pipelines as a method of preventing hydrate and wax plugs*, in *Proceedings of the Eighth International Offshore and Polar Engineering, Vol 2*. 1998, International Society Offshore& Polar Engineers.
9. Nisancioglu, K., *Personal communication*. 17/3-2015, Norwegian University of Science and Technology: Trondheim.
10. Rubinstein, I., ed. *Physical Electrochemistry: Science and Technology: Principles, Methods and Applications*. 1995, CRC Press.
11. Orazem, M.E., *Electrochemical Impedance Spectroscopy*. 2008, Department of Chemical Engineering, University of Florida.
12. Orazem, M.E. and B. Tribollet, *Electrochemical Impedance Spectroscopy*. 2008: John Wiley & Sons Inc.
13. Nisancioglu, K., *Corrosion Basics and Engineering*. 2013: Norwegian University of Science and Technology.
14. King, F. and M. Kolar, *Theory Manual for the Steel Corrosion Model Version 1.0.* 2009.
15. Lu, Z., et al., *Effects of a magnetic field on the anodic dissolution, passivation and transpassivation behaviour of iron in weakly alkaline solutions with or without halides.* Corrosion Science, 2006.
16. Meng, G.Z., C. Zhang, and Y.F. Cheng, *Effects of corrosion product deposit on the subsequent cathodic and anodic reactions of X-70 steel in near-neutral pH solution.* Corrosion Science, 2008.
17. Sato, N., *An overview on the passivity of metals.* Corrosion Science, 1990.
18. NORSOK, *Cathodic Protection M-503*, in *Common Requirements*. 1997.
19. DNV, *Cathodic Protection Design*, in *Recommended Practice DNV-RP-B401*. 2011.
20. Instruments, G. *Reference Electrodes*. 2014 [cited 2014 4/11]; Available from: http://www.gamry.com/products/accessories/reference-electrodes/.
21. Galsgaard, F., et al., *AC/DC interference corrosion in piplines*. 2006, MetriCorr.
22. Elbeik, S., A.C.C. Tseung, and A.L. Mackay, *The formation of calcareous deposits during the corrosion of mild steel in sea water.* Corrosion Science, 1986.
23. Sun, W., et al., *A mathematical model for modeling the formation of calcareous deposits on cathodically protected steel in seawater.* Electrochimica Acta, 2012.
24. Moller, H., E.T. Boshoff, and H. Froneman, *The corrosion behaviour of a low carbon steel in natural and synthetic seawaters.* Journal of the South African Institute of Mining and Metallurgy, 2006.

25. DNV, *Submarine Pipeline Systems*, in *Offshore Standard DNV-OS-F101*. 2012.
26. Hagen, C.H.M., *The Influence of Alternating Current on the Polarization Behavior of Stainless Steels*. 2013, Norwegian University of Science and Technology.
27. Esser, C.B., *The Influence of Alternating Current on the Polarization behavior of Stainless Steel in Artificial Seawater*. 2013, Norwegian University of Science and Technology.
28. Fu, A.Q. and Y.F. Cheng, *Effects of alternating current on corrosion of a coated pipeline steel in a chloride-containing carbonate/bicarbonate solution.* Corrosion Science, 2010.
29. Kim, D.-K., et al., *Electrochemical studies on the alternating current corrosion of mild steel under cathodic protection condition in marine environments.* Electrochimica Acta, 2006.
30. Xu, L.Y., X. Su, and Y.F. Cheng, *Effect of alternating current on cathodic protection on pipelines.* Corrosion Science, 2013.
31. Pagano, M.A. and S.B. Lalvani, *Corrosion of mild steel subjected to alternating voltages in seawater.* Corrosion Science, 1994.
32. Muralidharan, S., et al., *Influence of alternating, direct and superimposed alternating and direct current on the corrosion of mild steel in marine environments.* Desalination, 2007.
33. Büchler, M., *Alternating current corrosion of cathodically protected pipelines: Discussion of the involved processes and their consequences on the critical interference values.* Materials and Corrosion-Werkstoffe Und Korrosion, 2012.
34. Büchler, M., C.-H. Voûte, and D. Joos, *Effect of variation of cathodic protection level over time on the a.c. corrosion process*. 2012, Ceocor: Lucerne.
35. Bergin, A., *The Influence of Alternating Current on the Corrosion of Carbon Steel under Cathodic Protection*. 2014, Norwegian University of Science and Technology: Trondheim.
36. Nisancioglu, K., *Personal Communication*. 27/4-2015, Norwegian University of Science and Technology: Trondheim.
37. Benke, G. and W. Gnot, *The electrochemical dissolution of platinum.* Hydrometallurgy, 2002.
38. Bosch, R.W. and W.F. Bogaerts, *A theoretical study of AC-induced corrosion considering diffusion phenomena.* Corrosion Science, 1998.
39. Goidanich, S., L. Lazzari, and M. Ormellese, *AC corrosion – Part 1: Effects on overpotentials of anodic and cathodic processes.* Corrosion Science, 2010.
40. Lazzari, L., et al., *Laboratory Test Results of AC Interference on Polarized Steel*, in *Corrosion*. 2003, NACE International: San Diego, California, USA.
41. Xu, L.Y., et al., *Development of a real-time AC/DC data acquisition technique for studies of AC corrosion of pipelines.* Corrosion Science, 2012.
42. Stamnes, I., *AC corrosion of pipe line steel*, in *Department of Materials Science and Engineering*. 2010, Norwegian University of Science and Technology: Trondheim.
43. Lilleby, L.S., S.M. Hesjevik, and S. Olsen, *Effects From Alternating Current On Cathodic Protection Of Submarine Pipelines*, in *Corrosion*. 2011, NACE International: Houston, Texas, USA.
44. Hagen, C.H.M., *A comparative study of AC-induced corrosion of X65 Carbon Steel and 316L Stainless Steel in 3.5 wt% NaCl electrolyte*. 2012, Norwegian University of Science and Technology: Trondheim.
45. ASTM, *Standard Practice for Preparing, Cleaning, and Evaluating Corrosion Test Specimens*, in *G1*. 1999.
46. ASTM, *Standard Practice for the Preparation of Substitute Ocean Water*, in *D1141*. 2013.
47. Nisancioglu, K., *Personal communication, E-mail*. 23/2-2015, Norwegian University of Science and Technology: Trondheim.
48. Brown, M.H., W.B. Delong, and J.R. Auld, *Corrosion by Chlorine and by Hydrogen Chloride at High Temperatures.* Industrial and Engineering Chemistry, 1947.
49. Hauffe, K. and H. Puschmann, *A34 Platinum and platinum alloys.* Corrosion Handbook, 2011.
50. Beverskog, B. and I. Puigdomenech, *Pourbaix Diagrams for the Ternary System of Iron-Chromium-Nickel.* 1999.
51. Pourbaix, M.J.N., J.V. Muylder, and N.d. Zoubov, *Electrochemical Properties of the Platinum Metals.* Platinum Metals Review, 1959.
52. Pourbaix, M., *Bestimmung und anwendung von gleichgewichtspotentialen.* Materials and Corrosion, 1969.

APPENDICES

Appendix A: Equations

A.1 Required AC voltage

The VariAC applied AC in the form of voltage that was controlled through a multimeter connected in parallel with VariAC and working electrode. In order to apply the right AC current density, calculations were done to find the voltage that corresponded to that current density. Exposed area of sample, resistance of the AC-circuit, desired AC current density and Ohm's law was used to determine the required AC voltage, as seen in equation (A.1):

$$V_{AC} = A * R * i_{AC} \tag{A.1}$$

Where:

V_{AC} = required AC voltage [V]

A = exposed area [cm^2]

R = resistance [Ω]

i_{AC} = desired AC current density [A/cm^2]

A.2 Corrosion rate (CR)

The corrosion rate (CR) in mm/year was calculated by the following equation:

$$CR = \frac{k * \Delta m}{t * \rho * A} \tag{A.2}$$

Where:

Δm = mass loss [g]

k = constant equal to $8.76 * 10^4$ [mm*hours/cm*years]

t = duration of experiment [h]

ρ = density of steel, set to 7.86 [g/cm^2] for all steels

A = exposed area [cm^2]

Appendix B: Weight loss-graph for X65

The cleaning solution that was used to clean the X65-samples after testing, also caused metal loss of the sample itself. Thus, preventive measures were performed as described according to ASTM G-1 [45], to find the actual mass loss due to corrosion. The approach was to repeat the cleaning cycle several times and plot the mass loss between each cycle in a graph, which an example of can be seen in Figure B-1. Further, the measured mass loss at each cycle was corrected for any metal loss, where this correction was based on cleaning of an untested sample. Usually six cleaning cycles were performed and plotted in the graph, which could be divided into two trend lines. The mass loss due to corrosion will then correspond to the intersection of these trend lines.

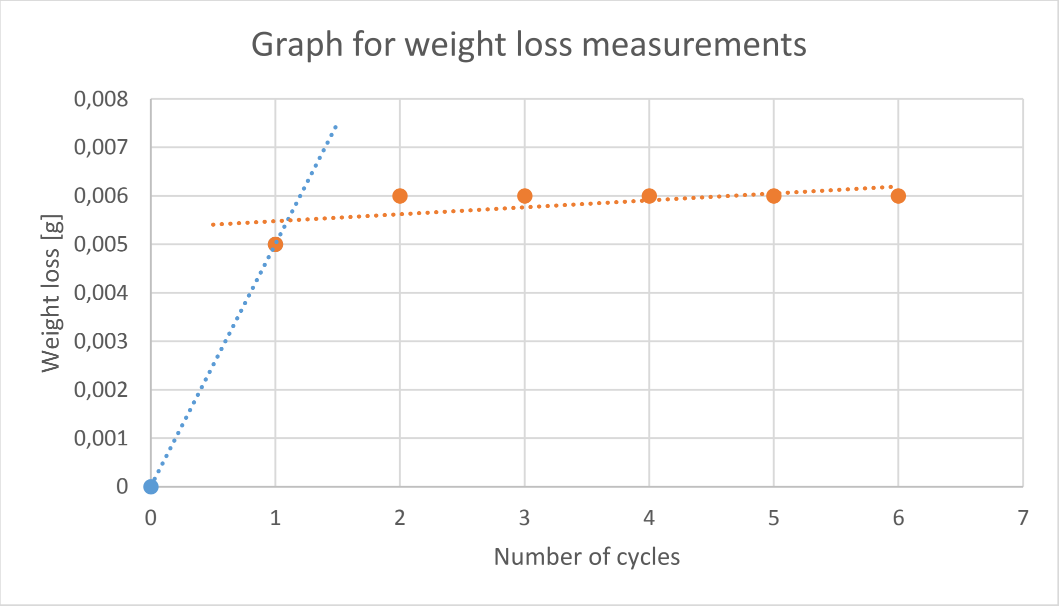

Figure B-1: Example of measured weight loss as a function of number of cycles, according to ASTM G-1. The corresponding experiment was performed at a grinded X65-sample tested in 3.5 % NaCl-solution at -1050 mV DC and 500 A/m^2 AC. The weight loss was determined to be 0.0055 g.

Appendix C: Reproducibility

The results from experiments performed on X65 in 3.5 % NaCl-solution at 500 A/m^2 AC was, in addition to be compared with artificial seawater and to investigate surface roughness, used to test reproducibility of data compared to C. H. M. Hagen's thesis [26]. The CRs compared was calculated from experiments performed under an applied DC of -800 mV and -1050 mV DC, and can be seen in **Figure C-1**.

From the figure, it can be seen that results were quite similar and thus the experimental procedure was sufficient to collect new data.

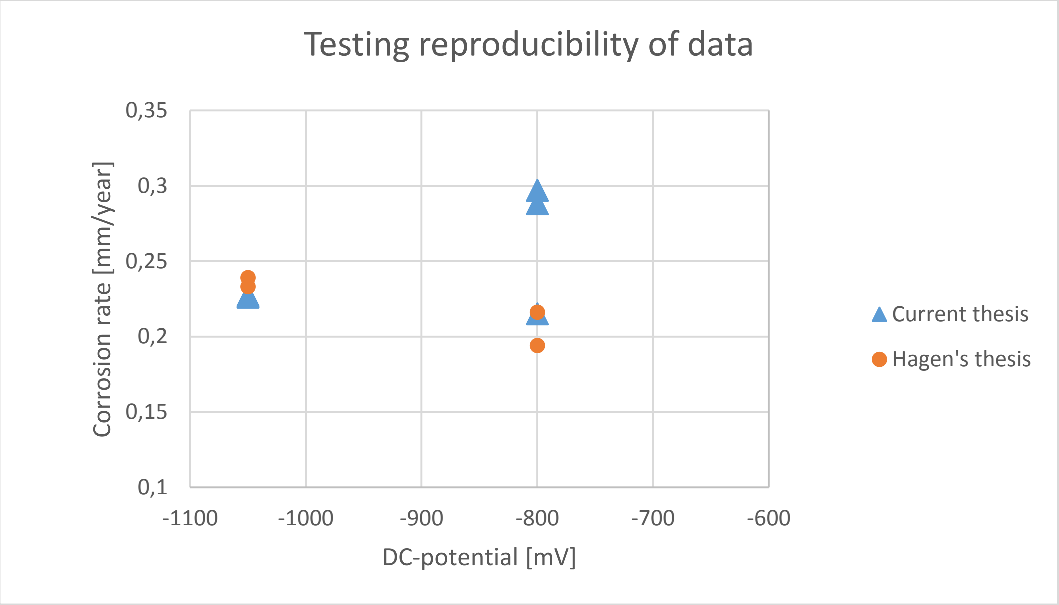

Figure C-1: Corrosion rate as a function of applied DC-potential. The plot compares results from this thesis with results from C. H. M. Hagen's thesis. The results were acquired from experiments performed at -800 mV and -1050 mV DC, in 3.5 % NaCl-solution at 500 A/m^2 AC.

Appendix D: Parallel testing of 25Cr

The 25Cr-sample that were tested in artificial seawater at -800 mV DC and 1000 A/m^2 AC, displayed a DC current response and a CR that was significantly different compared to the other experiments. Thus, one parallel test was performed. The DC current response for the two tests can be seen in Figure D-1, the V_{AC} can be seen in Figure D-2 and the calculated CR can be seen in Table D-1. Of the two experiments displayed, the first was presented in chapter 4 while the 2nd is only displayed here.

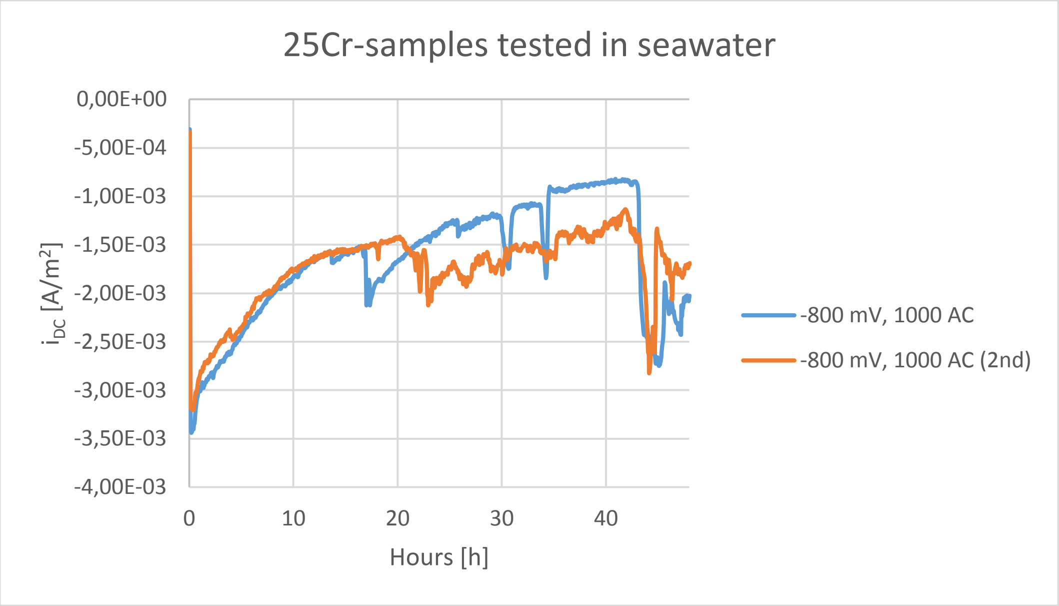

Figure D-1: The recorded DC current density response as a function of time. Both experiments have been tested at 25Cr under a DC of -800 mV at 1000 A/m^2 AC in artificial seawater.

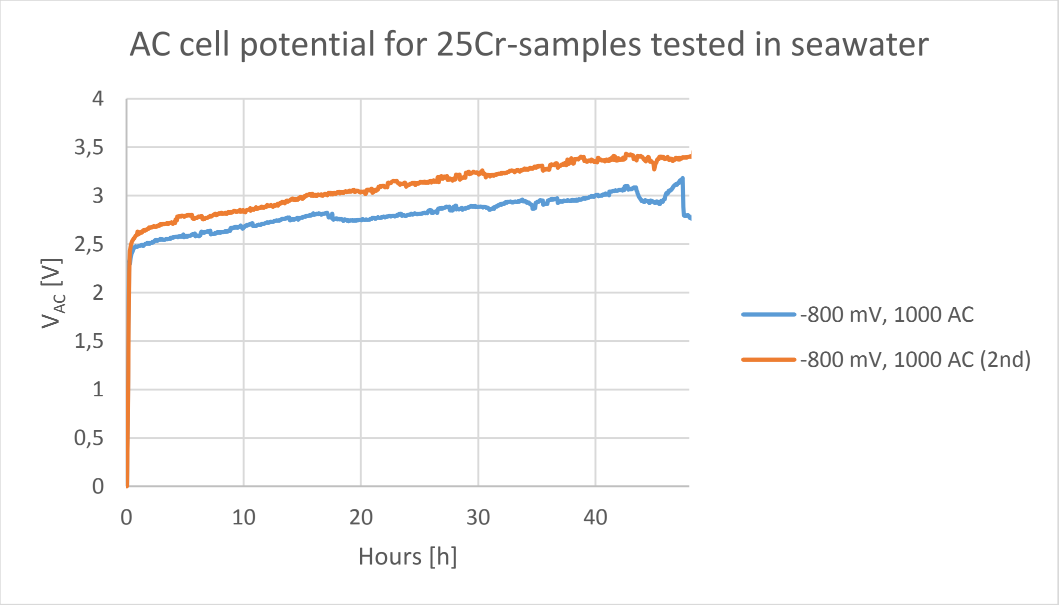

Figure D-2: The recorded AC cell potential as a function of time. Both experiments have been tested at 25Cr under a DC of -800 mV at 1000 A/m^2 AC in artificial seawater.

Table D-1: Calculated corrosion rate for 25Cr-samples. Both samples have been tested under a DC of -800 mV at 1000 A/m^2 AC in artificial seawater.

DC [mV]	AC [A/m^2]	Weight loss [mg]	Area [cm^2]	CR [mm/year]
-800	1000	6	2.67	0.522
-800	1000	5	2.42	0.480 (2nd)

Appendix E: Additional XRD data

Additional XRD analysis that was seen as redundant in chapter 4 is presented here. Figure E-1 displays the formed calcareous deposits that were formed on 316 at -800 mV DC and 1000 A/m^2 AC, and shows same composition as in Figure 4-22. Figure E-2 on the other hand, displays that the cell sediments analyzed only consisted of NaCl.

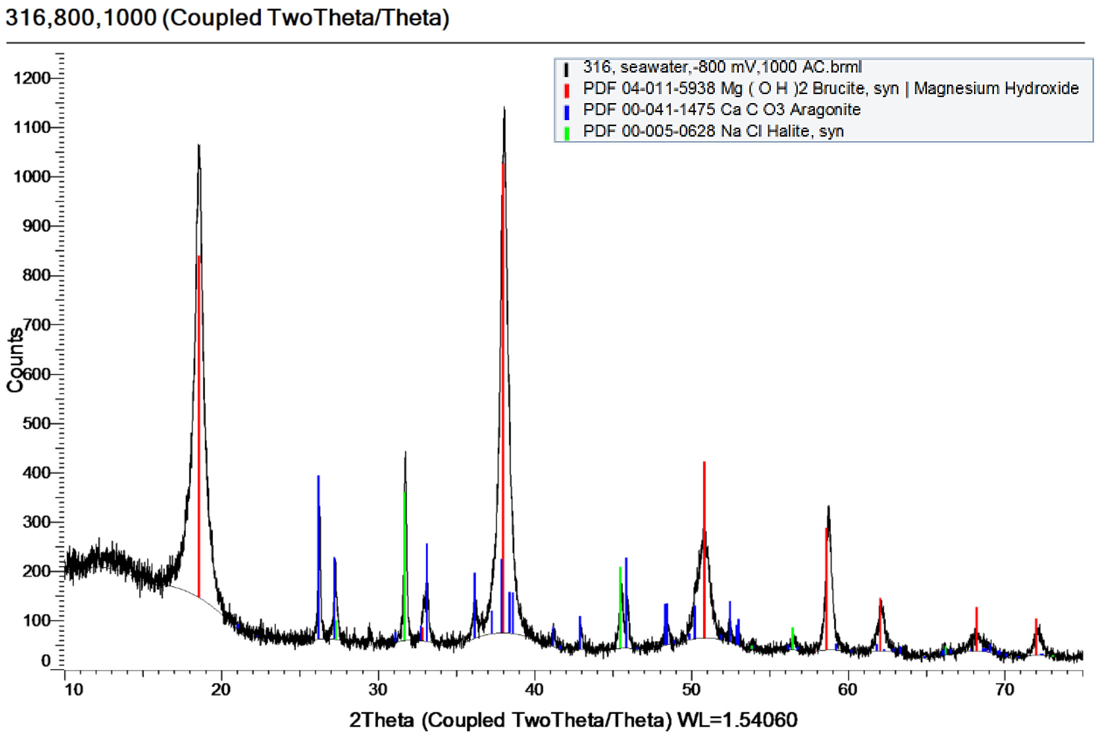

Figure E-1: X-ray diffractogram of crushed calcareous deposits formed on 316 tested in artificial seawater at -800 mV DC and 1000 A/m^2 AC.

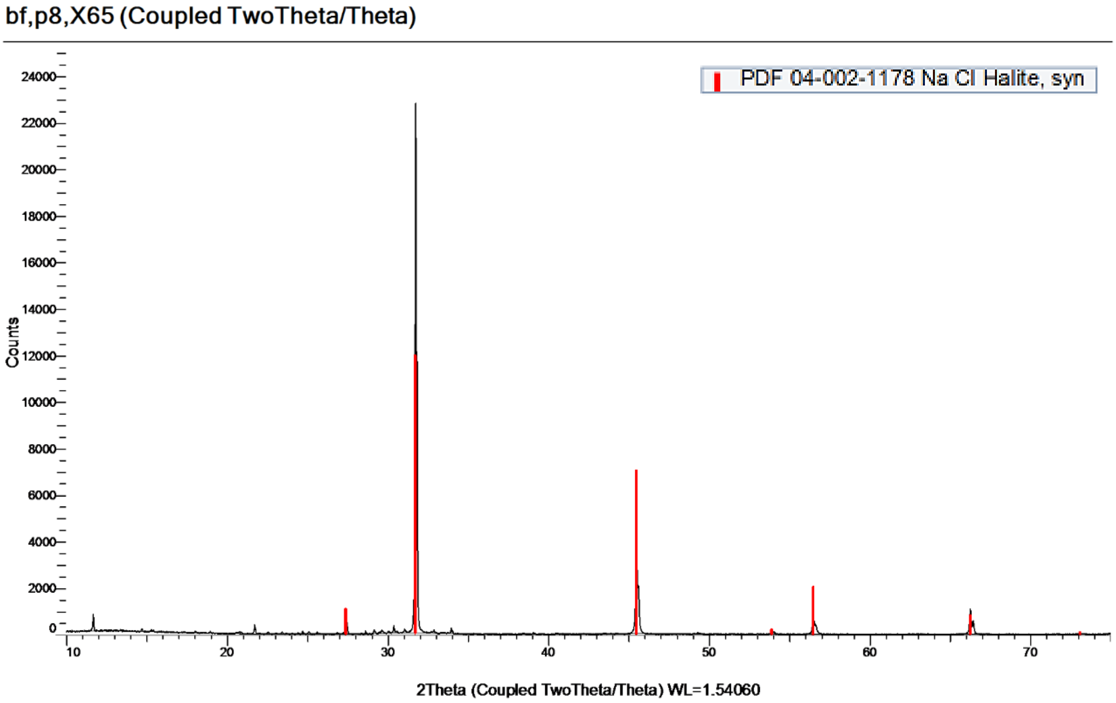

Figure E-2: X-ray diffractogram of crushed cell sediments formed during an experiment on X65 in artificial seawater at -800 mV DC and 500 A/m^2 AC.

Appendix F: Additional EDS data

The EDS analysis from the darkest area of a cleaned 25Cr-sample tested in artificial seawater at -800 mV DC and 500 A/m^2 AC, can be seen in Figure F-1 with its corresponding composition in Table F-1 to F-3. It can be seen that the sample is covered by a Pt-layer.

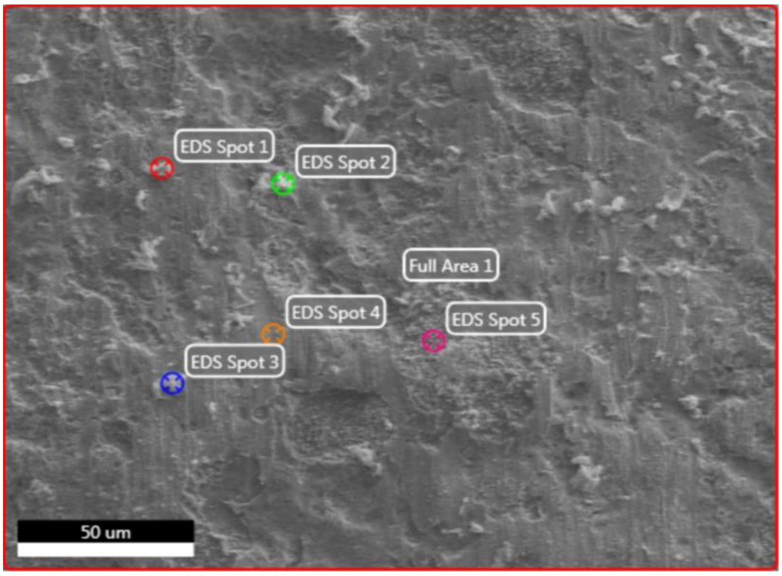

Figure F-1: SEM image from the darkest area seen on the 25Cr-sample tested in artificial seawater at -800 mV DC and 500 A/m^2 AC.

Table F-1: The measured composition of EDS Spot 1 visible in Figure F-1.

Element	Weight %	Atomic %	Net Int.	Error %	K-ratio
Pt-Mβ	100.00	100.00	675.95	2.63	1.00

Table F-2: The measured composition of EDS Spot 4 visible in Figure F-1.

Element	Weight %	Atomic %	Net Int.	Error %	K-ratio
Pt-Mβ	100.00	100.00	167.13	5.85	1.00

Table F-3: The measured composition of Full Area 1 (which is the whole image) visible in Figure F-1.

Element	Weight %	Atomic %	Net Int.	Error %	K-ratio
Pt-Mβ	100.00	100.00	149.01	5.31	1.00